

UCSF

UC San Francisco Electronic Theses and Dissertations

Title

Investigating cDC1 priming requirements and T cell differentiation outcomes in cancer and infection

Permalink

<https://escholarship.org/uc/item/2675z4g1>

Author

DeBarge, Rachel

Publication Date

2023

Peer reviewed|Thesis/dissertation

Investigating cDC1 priming requirements and T cell differentiation outcomes in cancer and infection

by
Rachel DeBarge

DISSERTATION
Submitted in partial satisfaction of the requirements for degree of
DOCTOR OF PHILOSOPHY

in

Biomedical Sciences

in the

GRADUATE DIVISION
of the
UNIVERSITY OF CALIFORNIA, SAN FRANCISCO

Approved:

DocuSigned by:

Lewis Lanier

Lewis Lanier

C111345FC07E42F...

Chair

DocuSigned by:

Matthew Spitzer

Matthew Spitzer

DocuSigned by:

Lawrence Fong

Lawrence Fong

91A2D66309BE4D7...

Committee Members

Acknowledgements

The process of earning a PhD is an incredibly difficult and isolating experience. As this degree is so individualized, successful completion is ultimately up to the pursuant. However, I wouldn't have reached this finish line without the support system I've garnered throughout the years.

I joined Matt Spitzer's lab for my PhD research for a variety of reasons, but a big part was due to how Matt ran his lab. Here, I felt like an equal member of a research group, worthy of trust and freedom to pursue questions that interested me most. Paradoxically, I also appreciated Matt's ability to synthesize my oftentimes scattered ideas and help me focus in on the best path forward. As is often the case, my thesis work had a lot of ups and downs, and I'm thankful to have had Matt as a source of support and guidance throughout. Similarly, I'd like to thank the other members of my thesis committee, Lewis Lanier and Lawrence Fong, who always provided invaluable insight and guidance during my committee meetings. I'm also grateful for the members of my qualifying exam committee who helped guide me through one of the most difficult processes of this PhD: Ari Molofsky, Tiffany Scharschmidt, and Mark Ansel. I feel lucky to have been mentored by those who have contributed so much to the scientific field.

I also greatly appreciated the collaborative style of Matt's lab and had the opportunity to work with and be guided by many amazing scientists. I appreciated the guidance from Lauren Levine, Nam Woo Cho, Joel Babdor, Elizabeth McCarthy, and the opportunity to work closely with so many others. I'm especially thankful to have gotten to work closely with Kamir Hiam-Galvez for several years early in my PhD journey, and consider him to be the most impactful mentor I've had in the lab. Kamir taught me so

much – how to do countless lab techniques, how to think like a scientist, how to code and analyze big data, and more. Most importantly, he showed me how to lead with compassion, and that I needn't compromise my values or who I am to do rigorous science. I'm incredibly grateful to have worked with him, and don't think my PhD would have been the same if I had not. Outside of the Spitzer lab, I was able to collaborate with an amazing Berkeley grad student, Jesse Garcia Castillo. Jesse is a fantastic scientist and I feel lucky that we worked together so seamlessly. I'm happy to have had my first co-first author manuscript be in collaboration with him and Michel DuPage.

I'm also thankful for the invaluable support, friendship, and love afforded to me from afar throughout this process. It was hard to leave my family and friends on the East Coast, but staying connected with them virtually and having visits whenever possible were needed reprieves from the stresses of grad school. I must especially thank my mom, Michelle DeBarge, who has always been my biggest supporter –I wouldn't be where I am today without her.

Graduate school was tough, and I wouldn't have gotten through it without my San Francisco support system: my best friend Nick Mroz, my pup Sadie, and my partner Frank Buquicchio. They help me escape, relax, and put everything into perspective. I'm so happy to have met Nick in grad school and he's not only an incredible friend, but also often a source of scientific support. This is also true for my partner, Frank, who I was so lucky to do an Immunology PhD alongside. I can't adequately express here how much he means to me and how invaluable his support was throughout this process. He took care of me and believed in me when I didn't have the strength to myself.

Investigating cDC1 priming requirements and T cell differentiation outcomes in cancer and infection

Rachel DeBarge

Abstract

Adaptive immune responses are essential for long-term immunity and the success of many disease treatments such as vaccines and antibody-based immunotherapy. Conventional type I dendritic cells (cDC1s) initiate this response by presenting antigen, providing co-stimulation, and producing cytokines to prime *de novo* T cell responses. After priming, T cells clonally expand, create long-term memory, and execute effector functions to clear tumors and pathogens. Understanding signals that can affect T cell priming and expansion in disease is vital for improving treatment approaches. This study explores how tumors can disrupt cDC1-T cell priming distal to the tumor site by using an intravenous *Listeria monocytogenes* infection as a model of a peripheral Type-I immune response. *In vivo* studies revealed a tumor-initiated IL-1 autocrine loop drives cDC1 dysfunction in the spleen, and blockade of IL-1R signaling was sufficient to rescue deficits in CD8⁺ T cell priming abilities of cDC1s. Further, we developed a CyTOF approach to investigate T cell dynamics after key priming timepoints. We performed a comparative analysis of T cell receptor (TCR) V α - and V β -chain use among different diseases and treatment modalities. This strategy identified expansions of specific V β and V α chain-expressing CD8⁺ and CD4⁺ T cells with varying differentiation states in response to *Listeria monocytogenes*, tumors, and respiratory influenza infection. Taken together, these studies advance our understanding of T cell priming and differentiation dynamics by investigating signals upstream of cDC1 activation as well as T cell TCR use and differentiation across disease.

TABLE OF CONTENTS

CHAPTER 1: INTRODUCTION	1
1.1 OVERVIEW.....	1
1.2 INITIATION OF ADAPTIVE IMMUNITY	2
1.3 REGULATION AND STUDY OF T CELL PRIMING AND POLARIZATION	3
 CHAPTER 2: A MASS CYTOMETRY APPROACH TO TRACK THE EVOLUTION OF T CELL RESPONSES DURING INFECTION AND IMMUNOTHERAPY BY PAIRED T CELL RECEPTOR REPERTOIRE AND T CELL DIFFERENTIATION STATE ANALYSIS	 5
2.1 AUTHOR CONTRIBUTIONS.....	6
2.2 ACKNOWLEDGEMENTS	6
2.3 ABSTRACT	7
2.4 INTRODUCTION.....	8
2.5 RESULTS.....	10
<i>2.5.1 Tracking the phenotypes of clonal T cell responses against Listeria monocytogenes with CyTOF.....</i>	<i>10</i>
<i>2.5.2 Expanded CD8⁺ and CD4⁺ T cells expressing specific TCR Vβ chains are enriched for recognition of antigens from LADD</i>	<i>12</i>
<i>2.5.3 Activated Vβ14⁺ CD8⁺ T cells expand in response to OVA-expressing tumors and recognize the OVA antigen.....</i>	<i>16</i>
<i>2.5.4 Respiratory infection with influenza induces expansions of CD8⁺ and CD4⁺ T cells using specific Vβ chains linked to the recognition of influenza antigens</i>	<i>17</i>
<i>2.5.5 Expanded T cells using different Vβ chains adopt distinct differentiation states in response to immunization versus primary infection with influenza</i>	<i>20</i>
<i>2.5.6 Transfer of convalescent serum shortly after respiratory influenza infection mimics aspects of prophylactic vaccination by reshaping the TCR repertoire of responding T cells.....</i>	<i>22</i>
2.6 DISCUSSION	25

2.7 MATERIALS AND METHODS	59
CHAPTER 3: TUMOR IL-1 AUTOCRINE LOOP DRIVES SYSTEMIC CHRONIC INFLAMMATION	
THAT CONSTRAINS THE ABILITY OF PERIPHERAL CONVENTIONAL TYPE 1 DENDRITIC	
CELLS TO PRIME T CELL RESPONSES	
3.1 AUTHOR CONTRIBUTIONS	68
3.2 ACKNOWLEDGEMENTS	68
3.3 ABSTRACT	69
3.4 INTRODUCTION	70
3.5 RESULTS	72
<i>3.5.1 Reduced cDC1 activation in AT3 tumor-bearing mice results in constrained T cell</i>	
<i>response to Listeria</i>	72
<i>3.5.2 Initiation of immune response and cytokine cascade is impaired in AT3</i>	
<i>tumor-bearing mice responding to Listeria infection</i>	74
<i>3.5.3 Blockade of IL-1R1 signaling rescues altered immune response to Listeria in AT3</i>	
<i>tumor-bearing mice</i>	75
<i>3.5.4 Tumor-initiated IL-1 autocrine loop is a primary driver of peripheral cDC1</i>	
<i>dysfunction</i>	78
3.6 DISCUSSION	82
3.7 MATERIALS AND METHODS	98
CHAPTER 4: CLOSING AND FUTURE DIRECTIONS	106
REFERENCES	108

LIST OF FIGURES

Figure 2.1: Tracking the phenotypes of clonal T cell responses against attenuated Listeria (LADD) with CyTOF.....	31
Figure 2.2: Tracking a Listeria-specific CD8+ T cell response against LADD by TCR use and phenotyping with CyTOF.....	32
Figure 2.3: Tracking Listeria-specific CD4+ T cells against LADD by TCR use And phenotyping with CyTOF.....	33
Figure 2.4: The OVA- and Lm-expanded CD8+ and CD4+ T cells recognize LADD encoded antigens.....	34
Figure 2.5: CD8 response to Lm- and OVA-derived epitopes.....	36
Figure 2.6: CD4 response to Lm-derived epitopes.....	38
Figure 2.7: Comparative analysis of V β 14+V α 2+ CD8 expansion with scRNAseq During Lm infection.....	40
Figure 2.8: Activated V β 14+ CD8+ T cells expand in OVA-expressing tumor model.....	42
Figure 2.9: Tracking the expansion and recognition of CD8+ T cells specific for influenza antigens across multiple tissues.....	43
Figure 2.10: Expansion and activation of T cell subsets during flu infection across multiple tissues.....	45
Figure 2.11: Identification of flu NP-specific V β 14+ CD4+ T cells.....	46
Figure 2.12: Identification and phenotyping of V β 9+ Treg expansion after flu infection.....	47
Figure 2.13: V β 8.3+ CD8s have different phenotypes and frequencies in the	

context of influenza immunization model.....	48
Figure 2.14: Flu-specific conventional CD4+ T cell differentiation, but not repertoire, is altered by vaccination.....	49
Figure 2.15: Vβ9+ Treg clonal population is only present in the setting of a primary infection.....	50
Figure 2.16: Early convalescent therapy restricts the CD8+ T cell repertoire during influenza infection.....	51
Figure 2.17: Convalescent therapy has a limited effect on the CD4+ Teff repertoire during influenza infection.....	53
Figure 2.18: Vβ9+ Treg clonal population does not expand after early convalescent serum therapy.....	54
Figure 2.19: Semi-supervised clonotyping assignment script efficiently streamlines high dimensional single-cell proteomic analysis.....	55
Figure 3.1: Reduced cDC1 activation in AT3 tumor-bearing mice results in constrained T cell response to listeria.....	86
Figure 3.2: Reduced splenic cDC1 function driven by in vivo tumor presence.....	87
Figure 3.3: Initiation of immune response and cytokine cascade is impaired in AT3 tumor bearing mice responding to Listeria infection.....	88
Figure 3.4: Blockade of IL-1R1 signaling rescues altered immune response to listeria in AT3 tumor-bearing mice.....	90
Figure 3.5: Immune cell uptake of Lm-RFP affected by tumor burden.....	92
Figure 3.6: Tumor-initiated IL-1 autocrine loop is a primary driver of peripheral cDC1 dysfunction.....	93

Figure 3.7: Direct effects of IL-1R signaling constrained to tumor cells.....94

LIST OF TABLES

Table 2.1: Antibodies used for mass cytometry of T cell dynamics.....	56
Table 2.2: Markers used for cluster annotations.....	57
Table 3.1: CRISPR-Cas9 cell line editing information.....	93
Table 3.2: CyTOF antibodies used for time course studies.....	94
Table 3.3: Antibodies used for flow cytometry and cell sorting.....	95

Chapter 1: Introduction

1.1 Overview

Initiation and maintenance of an adaptive immune response is key for effective and long-lasting immunity. In particular, robust T cell responses are key for clearance of intracellular infections and anti-tumor immunity. Therefore, understanding the complete context that governs the initiation, functional capacity, and maintenance of T cell responses is vital for understanding and treating disease. Utilizing established mouse models of disease, *in vivo* perturbations, and high-dimensional proteomic and transcriptomic techniques, the aims of this thesis were as follows:

1. Determine the clonal and phenotypic evolution of T cell responses in response to infection and immunotherapy, as described in Chapter 2.
2. Investigate how tumor burden can affect the ability of peripheral antigen presenting cells to prime T cell responses, as described in Chapter 3.

1.2 Initiation of adaptive immunity

Dendritic cells are professional antigen-presenting cells that bridge innate and adaptive immunity and can be found in both lymphoid and non-lymphoid tissues. The canonical role of conventional dendritic cells, or cDCs, is to survey tissues for antigen, and then process and present this antigen to T cells for either a pro-immunogenic or pro-tolerogenic response. cDCs can be divided into two main subsets, cDC1s and cDC2s. cDC2s are efficient primers of many CD4 T cell responses, whereas cDC1s are the main drivers of *de novo* CD8 T cell priming and type I CD4 responses. cDC1s are efficient at both direct presentation of antigen (presenting peptides of intracellular pathogens) and cross-presentation of antigen (uptake of exogenous antigen for processing and presentation on major histocompatibility complex-I (MHC-I complexes)). Similar to other innate myeloid cells, cDC1s become activated after engagement of their pattern recognition receptors (PRRs)¹. In the context of a Type I immune response, cDC1s will also be exposed to pro-inflammatory cytokines like Type I interferons². These additional signals help drive upregulation of molecules such as CD80 and CD86, which bind to CD28 on T cells for co-stimulation³. Additionally, these signals will drive production of IL-12 from cDC1s, which is important for effector polarization of T cells. During this activation process, cDC1s will also upregulate antigen processing machinery and present MHC-I-peptide complexes for CD8 T cells⁴. These phenotypic changes are the three signals necessary for a proper *de novo* CD8 T cell response: MHC-I-peptide complexes on the surface, costimulatory molecule expression, and cytokine production.

Each T cell has a unique receptor (TCR) capable of recognizing specific antigens to rapidly resolve immune insults as well as create long-term cellular immunity. The ability

of T cells to create immunological memory to resolve perturbations more quickly upon rechallenge make them a highly relevant cell type in many disease indications. This includes autoimmunity, infectious disease, and cancer. So, many therapeutic approaches including vaccination, checkpoint blockade, and cell-based immunotherapy target or utilize T cells. Thus far, many studies have focused on how certain perturbations and immunotherapies affect T cells. Further, many of these studies have focused on T cell intrinsic drivers of fate and function such as transcription factor dynamics and metabolic regulation^{5,6}. However, given the early imprinting of T cell fate after priming^{7,8}, studying the transient signals and cell states leading up to and affecting priming is essential.

1.3 Regulation and study of T cell priming and polarization

Tumors are known to inhibit immune cell function to escape clearance. This can happen both by inhibiting pro-immunogenic subsets of immune cells, such as cytotoxic T cells and cDCs, and by promoting function of suppressive or pro-tolerogenic subsets of immune cells^{9,10}. Mechanisms of suppression by tumors have generally focused locally on the tumor microenvironment or proximally in draining lymph nodes. These locations are where suppression of immunogenic cDCs have been previously described. Tumors can interfere with proper cDC differentiation, disrupt activation signals, create metabolic stress, inhibit antigen processing and presentation, affect cellular viability, and more⁹⁻¹¹. Recent advances have shown the extent to which tumors systemically disrupt the homeostasis of the immune system, altering immune cell composition and phenotype in the tumor microenvironment (TME), lymph nodes, spleen, blood, and bone marrow. Additionally, mechanistic studies into cancer immunotherapy efficacy have shown that

initiation of *de novo* T cell responses, particularly ones originating in the periphery, are vital for the effectiveness of cancer immunotherapy¹²⁻¹⁴.

As the immune response is highly coordinated and regulated, even minor disruption of certain signals can skew the canonical T cell response to pathogens. This necessitates the utilization of high-throughput and high-dimensional methods that can monitor the clonal dynamics of T cell responses. We understand many aspects of T cell development and function, but technological advances in recent years have expanded the depth and nuance we're able to apply to basic questions regarding T cell immunology. Although methods to track clonal T cell responses exist, current strategies are either slow and labor intensive or lack broad applicability. T cell receptor sequencing can identify patterns in TCR use within discrete populations but collapses the phenotypic heterogeneity that happens after clonal expansion¹⁵⁻¹⁷. Paired single cell sequencing of TCR and gene expression can be a powerful tool, but can be limited by transcript recovery and cell input^{13,18,19}. Antigen-specific readouts like tetramer staining can identify T cells responding to an epitope of interest, but requires knowledge of said epitope and creation of unique peptide:MHC complexes for each target epitope^{20,21}.

Thus, there has been a limited capacity in the field to study broad changes in the clonality and T cell responses together with measurements of T cell function. Fully understanding the nuances of adaptive immunity in different tissues and diseases can further our understanding of systemic immune cell coordination. This deeper understanding will help us create generalizable principles as well as tissue and disease specific characterizations that should be considered for therapeutic development and future study design.

Chapter 2: A mass cytometry approach to track the evolution of T cell responses during infection and immunotherapy by paired T cell receptor repertoire and T cell differentiation state analysis

Jesse Garcia Castillo^{1,9}, Rachel DeBarge^{2,3,9}, Abigail Mende¹, Iliana Tenvooren^{2,3}, Diana M. Marquez^{2,3}, Adrian Straub⁷, Dirk H. Busch⁸, Matthew H. Spitzer^{2-6,10}, Michel DuPage^{1,10}

¹ Division of Immunology and Molecular Medicine, Department of Molecular and Cell Biology, University of California, Berkeley, Berkeley, CA 94720, USA

² Department of Otolaryngology-Head and Neck Surgery, University of California, San Francisco, San Francisco, CA 94143, USA

³ Department of Microbiology and Immunology, University of California, San Francisco, San Francisco, CA 94143, USA

⁴ Helen Diller Family Comprehensive Cancer Center, University of California, San Francisco, San Francisco, CA 94143, USA

⁵ Parker Institute for Cancer Immunotherapy, San Francisco, CA 94129, USA

⁶ Chan Zuckerberg Biohub San Francisco, San Francisco, CA 94158, USA

⁷ Institute for Medical Microbiology, Immunology and Hygiene, Technische Universität München (TUM), Munich, Germany.

⁸ Institute for Medical Microbiology, Immunology and Hygiene, Technische Universität München (TUM), Munich, Germany; Partner site Munich, German Center for Infection Research (DZIF), Munich, Germany.

⁹ These authors contributed equally.

¹⁰ These authors contributed equally.

Chapter 2 is reprinted as manuscript under review at Nature Immunology

2.1 Author Contributions

Conceptualization, J.G.C., R.D., M.D., M.H.S.; Experimental Methodology, J.G.C., R.D., A.M., I.T., D.M.M., M.D., M.H.S.; Computational Methodology, R.D., A.S., M.H.S.; Investigation, all authors; Writing – Original Draft, J.G.C., R.D., M.D., M.H.S.; Writing – Review & Editing, all authors; Funding Acquisition, M.D., M.H.S.; Supervision, M.D., M.H.S.

2.2 Acknowledgements

We acknowledge the UCSF Parnassus Flow Cytometry CoLab (RRID:SCR_018206) for assisting in generating mass cytometry data and the UC Berkeley Cancer Research Laboratory Flow Cytometry Facility. We also thank D. Portnoy (University of California, Berkley) for providing attenuated *Listeria* strains for this study. Research reported here was supported in part by Grants from the NIH 1DP2CA247830-01, P30 DK063720, and the NIH S10 Instrumentation Grant S10 1S10OD018040-01. J.G.C. is a HHMI Gilliam Fellow. M.D. is a Pew-Stewart Scholar and a St. Baldrick's Scholar with generous support from Hope with Hazel.

2.3 Abstract

T cell receptor (TCR) recognition followed by clonal expansion is a fundamental feature of adaptive immune responses. Here, we developed a mass cytometric (CyTOF) approach combining antibodies specific for different TCR V α - and V β -chains with antibodies against T cell activation and differentiation proteins to identify antigen-specific expansions of T cell subsets and assess aspects of cellular function. This strategy allowed for the identification of expansions of specific V β and V α chain-expressing CD8⁺ and CD4⁺ T cells with varying differentiation states in response to *Listeria monocytogenes*, tumors, and respiratory influenza infection. Expanded V β chain expressing T cells could be directly linked to the recognition of specific antigens from *Listeria*, tumor cells, or influenza. In the setting of influenza infection, we showed that the common therapeutic approaches of intramuscular vaccination or convalescent serum transfer altered the clonal diversity and differentiation state of responding T cells. Thus, we present a new method to monitor broad changes in TCR specificity paired with T cell differentiation during adaptive immune responses.

2.4 Introduction

The basis of adaptive immunity is the clonal expansion of rare T or B cells that are specifically reactive to unique antigens. In response to an infection, CD4⁺ or CD8⁺ T cells possessing a T cell receptor (TCR) that recognizes an antigen from the pathogen can activate, proliferate, differentiate, and then migrate to the site of infection to control it²²⁻²⁴. Clonal expansions include 3-10 cycles of division, creating 10 to 1,000+ cells from a single reactive T cell²⁵⁻²⁸. During the proliferative phase, and depending on the type of insult, clonally-expanded T cells will differentiate, gaining distinct functions with some acquiring the capacity to form long-lived memory cells²⁹⁻³². Although immune-based therapies can change the function of T cells to better fight disease, it has also been shown that they can change the clonal diversity (or repertoire) of the responding T cells^{15,33-37}.

Although methods to track clonal T cell responses exist, current strategies are either slow and labor intensive or lack broad applicability. Bulk TCR sequencing can identify patterns in the use of T cell receptor genes, but cannot directly link phenotypic or functional information about the cells that comprise clonal expansions of T cells¹⁵⁻¹⁷. Single-cell sequencing can pair unique TCR sequences with gene expression analysis to infer phenotype and function; however, it is limited in the number of cells that can be analyzed^{13,18,19}. Furthermore, transcription may infer some phenotypic attributes of T cells, but it is often imperfect, as many key cellular processes are regulated post-transcriptionally³⁸. Functional assays, such as ELISPOT, can enumerate cytokine production from antigen-specific cells but are limited to measuring one function at a time³⁹. Tetramer staining can identify T cells recognizing a particular peptide:MHC combination but require custom reagents for each specificity, which prevents investigation

of the total reactive T cell pool^{20,21}. Most challenging for these functional assays is the requirement that the antigens recognized by T cells already be known; thus, studying broad changes in the clonality and T cell responses together with measurements of T cell function has not been possible. Thus, we developed an approach to balance the trade-offs in T cell characterization techniques. We hypothesized that we could use simultaneous staining of unique V α and V β chains on T cells to learn about the TCR repertoire during a response. While not tracking single T cell clones, this approach would be fast, iterative, and scalable for use in many disease settings in mice and humans.

In this study, we used a novel mass cytometry by time of flight (CyTOF) approach to resolve these challenges. CyTOF is a technology that enables the quantification of >45 proteins in millions of single cells⁴⁰. The increase in the number of proteins that can be analyzed at once allowed us to develop antibody panels to detect both the V α and V β chains of different TCRs to monitor changes in the TCR repertoire while simultaneously measuring proteins to delineate T cell differentiation and function⁴¹. Flow cytometry-based staining of V α and V β TCR chains has been done previously to track clonal populations, but limitations of fluorescence-based readouts required the use of multiple panels or sacrificed the amount of phenotypic information gathered simultaneously⁴²⁻⁴⁴. As a demonstration of the utility of our approach, we linked expansions in TCR V α and V β chains to clonal expansions of T cells responding to well-defined antigens from *Listeria monocytogenes* (*Lm*) and influenza. Although our approach does not require that the antigens targeted by T cells be known to track changes in the TCR repertoire, these studies allowed us to benchmark its performance in contexts of defined immunodominant antigens while also examining additional unknown T cell responses. Using our strategy

to study different treatment modalities for respiratory infection by influenza, we show that prophylactic vaccination by intramuscular injection versus passive transfer of convalescent serum both led to changes in the repertoire of responding T cells as well as in the differentiation state of T cells utilizing specific TCR V α and V β chains. By testing our approach in the setting of influenza infection, *Lm* infection, and cancer, we validate a new strategy that is readily applicable to study the T cell response in multiple settings without the need for custom reagents or tailored biological systems. We also developed automated data analysis approaches to identify populations of T cells with particular TCR V α and V β chains. Our findings advance the understanding of T cell priming and fate determination, elucidate ways immunotherapies could be improved, and enable future studies through technological development and validation.

2.5 Results

2.5.1 Tracking the phenotypes of clonal T cell responses against *Listeria*

***monocytogenes* with CyTOF**

In this study, we aimed to test whether mass cytometry (CyTOF) could be used to track clonal expansions of T cells during an immune response by using antibodies against TCR V β and V α chains combined with highly-multiplexed measurements of the protein expression of phenotypic markers of T cell activation and differentiation. First, we injected mice with attenuated strains of *Listeria monocytogenes*, referred to as attenuated double-deleted (*LADD*, $\Delta ActA \Delta InlB$), that either expressed the common model antigen ovalbumin (*LADD-OVA*) or did not (*LADD*) compared to PBS-injected controls (**Figure 2.1a**)⁴⁵. We chose *LADD* because it has been widely used to safely generate robust T

cell responses, especially CD8⁺ T cell responses, against overexpressed antigens in *LADD* as a cancer vaccine strategy^{45,46}. Indeed, five days after administration, we observed increased activation of CD8⁺ and CD4⁺ T cells in the spleens of *LADD*-infected mice compared to controls (**Figures 2.2a, b and 2.3a**). Clustering analysis of CD8⁺ T cells based on activation and differentiation proteins visualized by Uniform Manifold Approximation and Projection (UMAP) revealed effector T cell (T_{eff}) and some effector memory T cell (T_{em}) populations unique to *LADD*-infected mice (**Figure 2.1b, Table 2.2**). Due to the lack of CD62L in our initial panels, we were not able to distinguish central memory (T_{cm}) and naïve (T_{nv}) T cell populations during *Listeria* infection. The T effector (T_{eff}) populations were defined by the expression of LFA-1/CD11a and T-bet (**Figure 2.1c**). However, the Teff_1 population stood out as particularly different due to high expression of Ki-67 and PD-1. This cluster also expressed proteins CD49b, ICOS, and CD25 (**Figures 2.1c and 2.1d**), suggesting it consisted of early activated, antigen-specific CD8⁺ T cells (T_{ea}) that we recently described to have a unique metabolic state and to peak in abundance at this time after *Listeria* infection⁴⁷. Similar observations were made in CD4⁺ T cells, where Ki-67 expression differentiated two T_{eff} populations (**Figure 2.3a-c**).

Given that the CD8⁺ Teff_1 population had the greatest enrichment of markers indicative of antigen experience, we utilized Ki-67 and PD-1 expression to detect enrichment of TCR V β and V α chains in *LADD*- and *LADD-OVA*-infected mice within this proliferating subpopulation (**Figure 2.1e**). We identified V β 5.1/2⁺ and V β 12⁺ T cell populations expanded in mice infected with *LADD* or *LADD-OVA*, whereas V β 14⁺ T cells were only expanded in mice infected with *LADD-OVA* (**Figure 2.1e-1h**). Furthermore,

only *LADD-OVA*-infected mice had an expansion of $V\alpha 2^+$ $CD8^+$ T cells that were also $V\beta 14^+$ (**Figure 2.1e, 2.1i**). The expansion of $V\beta 14^+V\alpha 2^+$ T cells in *LADD-OVA*-infected mice may indicate that T cells with these TCR chains have clonally expanded due to their specificity for the OVA antigen. UMAP visualization and quantification of $V\beta 14$ expression in $CD8^+$ T cells, and more specifically $V\beta 14^+V\alpha 2^+$ $CD8^+$ T cells, revealed a clear enrichment in T cells expressing these TCR chains in the *Teff_1* cluster only after *LADD-OVA* infection (**Figure 2.1j, 2-1k, Figure 2.2c**), whereas $V\beta 12^+$ $CD8^+$ T cells could be found expanded in both *LADD*- and *LADD-OVA*-infected mice (**Figure 2.2d**). In $CD4^+$ T cells, we also observed increased usage of specific TCR $V\beta$ and $V\alpha$ chains in mice infected with *LADD* or *LADD-OVA*; however, no expansions were unique to *LADD-OVA* (**Figure 2.3e-h**). In particular, we found that $V\beta 13^+V\alpha 2^+$ $CD4^+$ T cells were dramatically increased in both *LADD*-infected mice (**Figure 2.3i**). Again, UMAP visualization of TCR $V\beta$ and $V\alpha$ chains revealed a clear enrichment in $CD4^+$ T cells expressing either $V\beta 13$ and $V\alpha 2$, or $V\beta 14$ in the *Teff_1* cluster of $CD4^+$ T cells with *LADD*-infection (**Figure 2.3j-m**). These results show that changes in the frequency of TCR $V\beta$ and $V\alpha$ chains used by T cells can be detected and quantified by our CyTOF approach during an immune response to *LADD*. We thus hypothesized that these changes in TCR chain usage were driven by clonal T cell expansions of $CD8^+$ and $CD4^+$ T cells directed against specific antigens expressed by *LADD*.

2.5.2 Expanded $CD8^+$ and $CD4^+$ T cells expressing specific TCR $V\beta$ chains are enriched for recognition of antigens from *LADD*

To validate that the increased $CD8^+$ and $CD4^+$ T cells with specific TCR $V\beta$ and $V\alpha$ chains was the result of their recognition of antigens expressed by *LADD* (OVA or

Listeria-derived antigens), we tested known antigens in peptide restimulation assays and loaded MHC tetramers with defined peptides to stain antigen-specific T cells (**Figure 2.4a** and **Figure 2.5a-c** and **2.6a,2.6b**). We calculated a fold-enrichment for either interferon-gamma (IFN- γ)-producing (**Figure 2.4b, 2.4d, 2.4f, and 2.4h**) or tetramer-positive (**Figure 2.4c** and **2.4g**) T cells for each specific TCR V β chain as compared to all CD8⁺ or CD4⁺ T cells. The major epitope from OVA recognized by H-2K^b-restricted CD8⁺ T cells is the peptide SIINFEKL⁴⁸. From our analysis in **Figure 2.1**, we hypothesized that the expanded V β 14⁺ CD8⁺ T cells were specific for OVA and most likely the SIINFEKL epitope. In support of our hypothesis, SIINFEKL peptide stimulation of splenocytes from *LADD-OVA*-infected mice led to IFN- γ production in CD8⁺ T cells, and IFN- γ ⁺ cells were significantly enriched for the expression of the V β 14 TCR (~10-fold) compared to all CD8⁺ T cells or CD8⁺ T cells expressing other TCR V β chains (**Figure 2.4b** and **Figure 2.5d, 2.5e**). CD8⁺ T cells using V β 5.1/2 were also enriched in this experiment, although very weakly. Notably, V β 5 is the TCR chain used in the OT-1 TCR transgenic mouse that recognizes the SIINFEKL epitope presented on H-2K^b MHC complexes⁴⁹. Using SIINFEKL-loaded H-2K^b tetramers, we also found that SIINFEKL-tetramer-positive cells were significantly enriched for V β 14 usage, and even further enriched in V β 14⁺V α 2⁺ cells (**Figure 2.4c**). These results indicate that V β 14⁺ and V β 14⁺V α 2⁺ CD8⁺ T cells in *LADD-OVA*-infected mice are significantly enriched in cells that recognize and respond to the SIINFEKL antigen, consistent with our hypothesis that we can use V β 14-expression together with activation and proliferation markers as a surrogate for CD8⁺ T cells specific to OVA in *LADD-OVA* infected mice.

Next, we tested whether the CD8⁺ and CD4⁺ T cells that expanded with specific TCR V β chains with both *LADD* and *LADD-OVA* infection recognized *Listeria*-derived antigens. Several *Listeria* antigens recognized by CD8⁺ and CD4⁺ T cells are derived from the Listeriolysin O (LLO) protein⁵⁰. We tested one peptide from LLO that is presented on H-2K^b to CD8⁺ T cells (VAYGRQVYL, denoted LLO1) and two additional peptides presented on MHC-II (I-A^b) to CD4⁺ T cells, designated LLO2 (NEKYAQAYPNVS) and LLO3 (AFDAAVSGKSVS)⁵¹. Splenocytes from *LADD* or *LADD-OVA*-injected mice were stimulated with VAYGRQVYL, enabling us to identify a population of CD8⁺ T cells that produced IFN- γ . Within the IFN- γ ⁺ population, CD8⁺ T cells expressing V β 12 were enriched ~3-fold compared to all CD8⁺ T cells (**Figure 2.4d** and **Figure 2.3f, 2.3g**). Therefore, we identified V β 14⁺V α 2⁺ CD8⁺ T cells recognizing SIINFEKL and V β 12⁺ CD8⁺ T cells recognizing VAYGRQVYL (**Figure 2.4e**).

To investigate the CD4⁺ T cell response to *LADD*, splenocytes from *LADD*-infected mice were stimulated with LLO2. In these mice, CD4⁺V β 13⁺ T cells were enriched ~20-fold within the IFN- γ ⁺ population compared to all CD4⁺ T cells or compared to other V β -expressing CD4⁺ T cells (**Figure 2.4f** and **Figures 2.6c, 2.6d**). Using MHC-II tetramers loaded with LLO2, we also observed a ~5-fold enrichment in V β 13⁺V α 2⁺ CD4⁺ T cells recognizing LLO2 compared to all CD4⁺ T cells from *LADD*-infected mice (**Figure 2.4g**). Using the LLO3 peptide to stimulate splenocytes from infected mice, we observed a ~3-fold enrichment in V β 14⁺ CD4⁺ T cells in the IFN- γ ⁺ population compared to all CD4⁺ T cells or compared to other V β -expressing CD4⁺ T cells (**Figure 2.4h** and **Figures 2.6e, 2.6f**). Interestingly, we also noted a significant but more modest enrichment in V β 8.1/2⁺ CD4⁺ T cells in the IFN- γ ⁺ population, which was also weakly observed with LLO2

stimulation. Thus, in several cases, enrichment in proliferating T cells expressing a specific V β chain was sufficient to capture expansions in CD8⁺ and CD4⁺ T cells with TCRs specific for antigens expressed by *LADD* (**Figures 2.4e** and **2.4i**). Therefore, measuring changes in TCR V β and V α chain use within the population of proliferating cells can identify clonally expanded T cells during an immune response. Our approach expands the use of CyTOF to identify antigen-responsive T cells at a single-cell level not possible by bulk T cell analysis, at a magnitude and throughput not attainable by single-cell TCR sequencing, and without requiring prior knowledge of the antigen(s) of interest.

To compare our CyTOF method to detect and phenotype antigen-responsive clonal populations to single-cell RNA sequencing methods, we re-analyzed a recently acquired single-cell RNA-seq dataset from CD8⁺ T cells sorted from spleens of mice infected with OVA-expressing *Listeria*⁵². Cells in this study were sorted that exhibited an activated (CD44⁺) phenotype or were SIINFEKL-reactive by tetramer staining⁵². Phenotypic analysis of the CD8⁺ T cells identified six distinct clusters of cells, which expressed similar markers as compared to our results using our CyTOF method (**Figure 2.7a-c**). Expression of *Mki67* and *Pdcd1* was also concentrated in clusters that were annotated as T_{eff} and T_{em} lineages (**Figure 2.7d**). Next, we determined whether V β 14⁺ and V β 14⁺V α 2⁺ CD8⁺ T cells were present among the SIINFEKL-reactive CD8⁺ T cells in this dataset. Indeed, CD8⁺ T cells expressing *Trbv31* (V β 14) and *Trav14d-2* (V α 2.1) were enriched in both the T_{eff} and T_{em} clusters, which were determined to be SIINFEKL-reactive (**Figure 2.7e, 2.7f**). When quantifying this enrichment, *Trbv31* (V β 14) cells were enriched only in the SIINFEKL-reactive cells (**Figure 2.7g, left**), but not in the cells that didn't react to SIINFEKL (**Figure 2.7g, right**). Most importantly, SIINFEKL-reactive CD8⁺ T cells that

expressed *Trav14d-2* (V α 2.1) were dramatically enriched in *Trbv31* (V β 14) expression (**Figure 2.7h**). Therefore, our CyTOF method and scRNA-seq methods both captured the same enrichment in TCR chain usage and CD8⁺ T cell phenotypes in response to *Listeria* overexpressing OVA.

We compared our results with this scRNA-seq dataset for their overall capacity to capture the distribution of TCR chain usage in this setting. First, we directly compared all V β chain assignments between both methods and observed comparable frequencies of V β chain assignment between the two methods (**Figure 2.7i-j**). When the two datasets were compared after removing unassigned TCRs in each dataset, the concordance was even higher for V β chain use in both datasets (**Figure 2.7i**). In fact, a direct comparison of V β chain abundances showed high correlation between both methods (**Figure 2.7k**). Taken together, the comparison of our CyTOF method to a paired scRNA-seq dataset generated in a separate lab, but with the same *Listeria* infection model, shows the feasibility and reproducibility of our CyTOF method for identifying and characterizing clonal T cell responses during infection.

2.5.3 Activated V β 14⁺ CD8⁺ T cells expand in response to OVA-expressing tumors and recognize the OVA antigen

We investigated whether OVA expression in cancer cells would also lead to an expansion of V β 14⁺ CD8⁺ T cells specific for OVA as observed with *LADD-OVA* infection (**Figure 2.1**). We inoculated mice with B16F10 melanoma tumor cells that either did or did not express OVA, and we monitored the frequency of V β 14⁺ cells in mice⁵³. In mice with B16F10-OVA tumors, we observed an increase in the frequency of V β 14⁺ CD8⁺ T cells within the proliferating (Ki-67⁺PD-1⁺) cells from tumors and tumor-draining lymph

nodes (tdLN) of mice, whereas this was not observed in B16F10 tumors lacking OVA expression (**Figure 2.8a**). Using tetramer staining, we validated that SIIN-H-2K^b + cells were enriched in V β 14⁺ CD8⁺ T cells (**Figures 2.8b** and **2.8c**). There was a ~2-fold enrichment in B16F10-OVA tumors and a ~3-fold enrichment in the tdLN. These results demonstrate that our approach can broadly identify OVA-specific CD8⁺ T cells based on their use of the TCR V β 14 chain across two different settings of immune responses. Although this is a robust proof of principle of our approach, it is not altogether surprising given the strong immunogenicity of the OVA antigen. Future studies should focus on whether our approach is sensitive enough to track clonal expansions of T cells responding to tumor neoantigens.

2.5.4 Respiratory infection with influenza induces expansions of CD8⁺ and CD4⁺ T cells using specific V β chains linked to the recognition of influenza antigens

During localized infections at non-lymphoid sites, such as the lung during influenza infection, antigens from a pathogen are trafficked from the site of infection to secondary lymphoid structures to activate and expand T cells that express a TCR that recognizes the antigen. These expanded T cells then migrate and infiltrate pathogen-infected tissues and mount an appropriate inflammatory response to remove the pathogen⁵⁴. To test whether our approach was capable of tracking T cell expansions in a natural model of respiratory infection, we used intranasal delivery of the PR8 strain of influenza (flu) and tracked expansions in TCR V β and V α chain use in T cells. We performed our CyTOF analysis ten days after flu infection across multiple tissues: the lungs, mediastinal lymph node (medLN) that drains the lung tissue, non-draining inguinal lymph nodes (ndLN), and the spleen (**Figure 2.9a**). We observed increased activation of both CD8⁺ and CD4⁺ T

cells by Ki-67 and PD-1 expression specifically in the lung, medLN, and spleen (**Figure 2.10a-c**). Clustering analysis of activation and differentiation proteins on CD8⁺ T cells visualized by UMAP showed the appearance of T_{eff}, T_{em}, and T_{cm} CD8⁺ T cell populations enriched in the flu-infected mice (**Figure 2.9b, Table 2.2**). The two T_{eff} populations shared expression of key phenotypic markers (e.g., KLRG1 and T-bet) that defined their effector lineage, but had differential expression of functional markers (e.g., granzyme B, IFN- γ). This differential expression of phenotypic and lineage markers has been previously shown for both the CD8 and CD4 compartment during influenza infection⁵⁵. In comparison, T_{em} and T_{cm} subsets were defined by differential expression of canonical markers (e.g., CD62L, CD44, Slamf6). Similar observations were made in CD4⁺ T cells with the identification of T_{eff}, T_{em}, and T_{cm} subsets (**Figure 2.11a and 2.11b**).

Using a similar approach to *LADD* infection, we utilized Ki-67 and PD-1 expression to identify TCR V β and V α chains associated with putative flu-specific CD8⁺ T cells (**Figure 2.9d**). We identified V β 8.3, V β 7, and V β 6 TCR chains expanded in CD8⁺ T cells in the lungs of influenza-infected mice (**Figures 2.9e-g**). However, the expansion of these V β chains in CD8⁺ T cells was variable in the medLN, ndLN, and spleen of flu-infected mice. When we overlaid V β chain expression on UMAPs of CD8⁺ T cells, where dimensionality reduction was based only on expression of activation and differentiation markers but not V β or V α chains, we found that V β 8.3, V β 7, and V β 6 expression was enriched in the T_{eff}_1 and T_{em}_1 compared to the T_{cm} and T_{nv} clusters (**Figures 2.9h-j**). We tested whether the expanded V β chain-expressing CD8⁺ T cells recognized any of the defined antigens from flu⁵⁶⁻⁵⁸. We prepared single-cell suspensions of cells from the lungs of PBS or flu-infected mice and stimulated with the following peptides:

ASNENMETM, derived from the PR8 nucleoprotein (NP) and SSLENFRAYV, derived from the viral polymerase subunit A (PA). There was ~4-fold enrichment in V β 8.3⁺ CD8⁺ T cells producing IFN- γ and TNF- α in response to ASNENMETM compared to all CD8⁺ T cells, even those expressing the other V β chains that expanded in flu-infected mice (**Figure 2.9k**). Single cells from lung tissue stimulated with SSLENFRAYV peptide exhibited ~6-fold enrichment of V β 7⁺ CD8⁺ T cells producing IFN- γ and TNF- α compared to all CD8⁺ T cells (**Figure 2.9l**).

For CD4⁺ T cells, there were two T_{eff} clusters that appeared in the lungs of infected mice (**Figure 2.11a**). These clusters were distinguished by differential expression of Ly6C, granzyme B, CD39, Slamf6, and CD69 (**Figure 2.11b**). Using Ki-67 as a marker of proliferating cells, we observed the expansion of V β 14⁺ CD4⁺ cells in the lungs, spleen, and in the medLN (**Figure 2.11c, 2.11d**). The V β 14⁺ CD4⁺ T cells that expanded were enriched in the T_{eff}_1 cluster that had the highest expression of inflammatory and activation markers (**Figure 2.11e**). We stimulated cells from PR8- or PBS- infected lungs with the LILRGSVAHKSCLPACV peptide, a NP- derived epitope presented on I-A^b and observed ~5-fold enrichment in V β 14⁺ CD4⁺ T cells compared to cells expressing other V β chains (**Figure 2.11f**). Thus, V β 14⁺ CD4⁺ T cells expanded in response to flu are enriched for recognition of the NP peptide (LILR...) (**Figure 2.11g**).

Regulatory T cells (Tregs) have also been shown to impact outcomes of infection with flu⁵⁹. Therefore, we tested whether our method allowed us to observe expansions in clonal Treg populations in response to flu infection. Interestingly, when looking across all tissues, we only observed an increase in the activation of Tregs in the medLN, but not in the lungs, ndLN, or spleen (**Figure 2.10d**). By UMAP analysis of the lungs, two new Treg

clusters appeared during infection with differential expression of activation and differentiation markers (**Figure 2.12a, 2.12b**). Using Ki-67 expression to separate proliferating cells, we observed an expansion in the frequency of V β 9⁺ Tregs in the lungs that were enriched in the eTreg_1 cluster (**Figure 2.12c-2.12e**). Together, these results indicate that our mass cytometric approach can identify CD8⁺ and CD4⁺ T cell populations specific for endogenous viral antigens across different tissues. In addition, we identified an expansion of a Treg clonal population in response to flu infection.

2.5.5 Expanded T cells using different V β chains adopt distinct differentiation states in response to immunization versus primary infection with influenza

We asked whether prophylactic vaccination of mice would change the clonality or differentiation state of responding T cells in response to flu infection. We vaccinated mice by intramuscular (IM) injection of live flu virus (PR8). We then allowed mice to generate memory cells for one month prior to rechallenging mice with a respiratory flu infection (**Figure 2.13a**). Clustering analysis was performed to analyze different T cell populations in the context of no vaccination, IM vaccination, primary flu-infection, and flu rechallenge after prior IM vaccination. There was no difference in the composition of CD8⁺ T cell populations at baseline between vaccinated mice or naïve mice (**Figure 2.13b**). However, in the context of primary infection, there was a large representation of T_{eff} populations, similar to our previous analysis (**Figure 2.9**). However, in flu-challenged mice that were previously vaccinated, there was a dominant population present that expressed CD69 and CD39, which was not present in other memory populations (**Figures 2.13b, 2.13c**). Their expression of CD69, but not other markers of recently activated effector cells such as T-bet, KLRG1, and granzyme B, is consistent with a CD8⁺ tissue-resident memory

(T_{rm}) cell phenotype⁶⁰. Employing PD-1 and Ki-67 as pan-activation markers for all $CD8^+$ T cells, we observed a substantial expansion of only the $V\beta 8.3^+$ $CD8^+$ T cells in mice that were rechallenged after vaccination (**Figures 2.13d** and **2.13e**). In contrast, we did not see an expansion of $V\beta 6^+$ or $V\beta 7^+$ $CD8^+$ T cells in rechallenged mice as was seen in mice with primary flu infection (**Figures 2.13e** and **2.9f-g**). We assessed the activation and differentiation state of the $V\beta 8.3^+$ $CD8^+$ T cells in the primary infection versus rechallenge by visualizing $V\beta 8.3^+$ cells by UMAP (**Figure 2.13f**). Interestingly, the $V\beta 8.3^+$ $CD8^+$ T cells were enriched in the T_{eff} states in the primary infection, but in rechallenged mice they were instead enriched in the T_{rm} state (**Figure 2.13f**). The exclusive enrichment of $V\beta 8.3^+$ $CD8^+$ T cells in rechallenged mice within the T_{rm} cluster may indicate that vaccination can change the differentiation state of flu-specific cells that are recalled in response to respiratory flu infection. Furthermore, the $V\beta 6^+$ and $V\beta 7^+$ $CD8^+$ T cells that were enriched in T_{eff} states in the primary infection did not expand with rechallenge, indicative of changes in the clonal dominance of T cells after vaccination. Our results also suggest that $CD8^+$ T cells with different specificities may differentiate asymmetrically into different types of memory cells after vaccination, resulting in restricted secondary T cell specificities against a respiratory flu infection.

In parallel, we also examined the impact of vaccination on the clonal behavior of conventional $CD4^+$ T cells and Tregs. Like $CD8^+$ T cells, conventional $CD4^+$ T cells also contained a $CD69^+CD39^+$ population that expanded specifically in mice that were rechallenged with flu after vaccination (**Figure 2.14a** and **2.14b**). Analysis of the proliferating pool ($Ki-67^+$) of $CD4^+$ conventional T cells (**Figure 2.14c**) revealed $V\beta 14^+$ cells that expanded in flu-infected mice independent of vaccination status (**Figure 2.14d**

and **2-11d**). However, in the flu-infected mice without prior vaccination, V β 14⁺ CD4⁺ conventional T cells were enriched in Teff_1 and Tem_2 clusters, whereas in vaccinated mice rechallenged with flu, they were instead enriched in the T_{rm} cluster, paralleling the differences observed in V β 8.3⁺ CD8⁺ T cells between these contexts (**Figure 2.13f**). Examination of the Treg compartment showed that the V β 9⁺ Tregs that expanded during primary flu infection did not expand in pre-vaccinated mice (**Figure 2.15**). Taken together, these results demonstrate that vaccination prior to respiratory flu infection alters the CD8⁺, CD4⁺, and Treg TCR repertoire and the differentiation state of cells expressing specific TCRs during a subsequent flu infection.

2.5.6 Transfer of convalescent serum shortly after respiratory influenza infection mimics aspects of prophylactic vaccination by reshaping the TCR repertoire of responding T cells

Our prior results indicated that immunological memory alters the TCR repertoire and functional state of responding T cells after flu rechallenge. These changes could result from the formation of memory T cells with flu-specific TCRs. Alternatively, altered T cell responses could be due to T cell-extrinsic factors, such as antibody responses that could support or prevent T cell priming by antigen-presenting cells or impact the viral load and thus the magnitude of the T cell response. Therefore, we investigated the effect of antibodies against flu on the T cell response by treating mice with convalescent serum from mice that recovered from respiratory flu infection. This approach also has therapeutic implications, as convalescent serum therapy is a standard form of treatment for severe respiratory viral infections, such as COVID-19, but its impact on the antiviral T cell response remains incompletely understood⁶¹.

We therefore tested whether the administration of serum therapy early after infection (4 hours post-infection) or just prior to the development of disease symptoms (4 days post-infection) impacted the T cell response to influenza infection (**Figure 2.16a**). We observed that mice were protected from weight loss when treated early during infection (**Figure 2.16c**). Mice receiving serum early in infection exhibited effector and memory CD8⁺ T cell populations that expressed lower levels of inflammatory markers, though they still expressed general activation markers such as PD-1 and Ki-67 (**Figures 2.16d, 2.16e**). When comparing distinct clonal populations within these proliferating CD8⁺ T cells, mice receiving serum early during infection had augmented frequencies of V β 8.3⁺ CD8⁺ T cells, and an expansion in V β 6⁺ cells was no longer present (**Figure 2.16f**), similar to our observations in response to vaccination (**Figure 2.13**). However, these V β 8.3⁺ clonal populations are preferentially clustered in a Tem₁ population, as in the primary infection (**Figure 2.16g**), and not toward a T_{rm} phenotype, as observed after vaccination and rechallenge (**Figures 2.16g** and **2.13f**). We hypothesize that this change in differentiation states occurs because memory T cell differentiation requires time to develop after antigen encounter. In contrast, the V β 7⁺ CD8⁺ T cell response was unaltered by serum transfer, and CD8⁺ T cells expanded and differentiated equivalently to what was observed with primary flu infection (**Figures 2.16f** and **2.16g**). These results indicate that anti-flu antibodies can impact the CD8⁺ T cell response to infection, both in the specificity and the differentiation state of responding CD8⁺ T cells.

T cell priming occurs early during an infection^{62,63}. Therefore, we hypothesized that treatment with convalescent serum later in an infection, but prior to the onset of severe symptoms (i.e. weight loss), might have a minimal impact on the T cell repertoire and

differentiation states. Consistent with this hypothesis, we did not observe any protection from weight loss in mice treated with convalescent serum 4 days after infection (**Figure 2.16c**). We also did not observe any changes in the differentiation of CD8⁺ T cells using V β 8.3, V β 6, or V β 7 TCR chains, all of which similarly expanded and differentiated into multiple T_{eff} and T_{em} phenotypes, compared to mice undergoing a primary flu infection (**Figure 2.16b**). In contrast to early serum transfer, serum treatment later in the infection resulted in equivalent expansion and differentiation of V β 8.3⁺ CD8⁺ T cells as seen in the primary infection (**Figures 2.16f and 2.16g**). Thus, antibody responses to flu, particularly in the context of transferred antibodies from vaccinated mice that have affinity matured, class switched, and likely have neutralizing capacity, altered the TCR specificity of responding CD8⁺ T cells as well as their differentiation program only when administered early after flu infection.

In contrast to the impact on CD8⁺ T cells, mice receiving serum exhibited fewer changes in CD4⁺ T cells (**Figure 2.17a-c**). Although there were noticeable reductions in the generation of T_{eff} populations with serum treatment at 4 hours post-infection, they were mild reductions. Furthermore, there were not any changes in the frequency of CD4⁺ T cells using the V β 14 chains with serum treatment early or late after infection, although early serum transfer had modest impacts on the differentiation state of these V β 14⁺ CD4⁺ T cells (**Figure 2.17d,2.17e**). Interestingly, however, we did find that the expansion of V β 9⁺ Tregs was blunted by convalescent serum transfer 4 hours post-infection (**Figure 2.18**), which matched the impact of IM vaccination (**Figure 2.15**). This result demonstrates that convalescent serum treatment is sufficient to prevent the expansion of this V β 9⁺ Treg population even in the absence of memory T cell responses. We

hypothesize that this result is due to the presence of neutralizing antibodies in the sera, but this needs to be tested to draw definitive conclusions.

2.6 Discussion

The T cell receptor (TCR) repertoire changes dramatically as a result of the clonal expansion of antigen-specific T cells during immune responses to pathogens and cancer. However, it is not fully understood to what extent this repertoire must be remodeled to achieve a successful immune response or therapeutic intervention. This highlights the need for better systems to track the clonality and phenotype of T cells during immune responses. Here we demonstrated that mass cytometry (CyTOF) can be used to track T cell populations with specific V β and V α chains, allowing us to identify several antigen-responsive T cell populations while also assessing their functionality, differentiation state, and proliferation across different disease models.

This approach has complementary strengths and weaknesses in comparison to single-cell RNA-sequencing (scRNA-seq) that is paired with TCR sequencing. For paired scRNA-TCR sequencing, where ~45% of TCR V β chains were not assigned, TCR assignment can be affected by transcript recovery, leading to a variable proportion of input cells lacking full TCR alpha-beta assignment. In contrast, although our CyTOF method only missed assigning ~25% of TCR V β chains, the approach is currently limited by the lack of available antibodies against other TCR variable chains (i.e., V β 1, 15, 16, 18, 20). In addition, the antibodies against V β 5.1/2 (BD clone MR9-4) and V β 8.1/2 (BD clone MR5-2) each bind to two V β chains that cannot be distinguished by CyTOF but can be deconvoluted by sequencing. For these reasons, both datasets were not fully overlapping, but this was anticipated as experiments were performed in distinct mouse

cohorts at two different laboratories. Therefore, it was impressive that despite these limitations and differences in methods, there were comparable frequencies of V β chain assignments broadly and specifically when assessing SIINFEKL-reactive CD8⁺ T cells (**Figure 2-7i**). CyTOF could be used as a high-throughput pre-screening tool to narrow the cell sorting and higher cost scRNA-seq platforms to specific V α and V β chain-expressing T cells⁶⁴¹.

We validated our CyTOF method using OVA as a model antigen to first identify an endogenous OVA-specific CD8⁺ T cell population and examine its differentiation and function in different disease contexts. We found that OVA-specific CD8⁺ T cell populations were enriched within V β 14⁺ CD8⁺ T cells in the *LADD-OVA* infection model and two OVA-expressing tumor models. Further, we identified *Listeria* antigen-specific CD8⁺ T cells and conventional CD4⁺ cells and validated the specificity of these populations using peptide restimulation, tetramer-based assays, and scRNA-seq data. Interestingly, our system was sensitive enough to identify changes in both CD4⁺ conventional T cells and CD8⁺ T cell subtypes that recognized endogenous *Listeria*-derived antigens, even when the strong model antigen OVA was present. We detected infiltration of OVA-specific V β 14⁺ CD8⁺ T cells in B16F10 tumors that expressed OVA and expansion of these V β 14⁺ CD8⁺ T cells in the tumor-draining lymph nodes. Thus, our CyTOF approach can capture the behavior of T cell populations across different disease models by measuring changes in the expansion of specific V β chain-expressing T cells, even in the context of an immunodominant antigen such as OVA.

A major finding using our CyTOF approach during respiratory influenza infection was the enrichment of CD8⁺ T cells with a T_{rm}-like phenotype and the restriction of the

anti-influenza TCR repertoire ($V\beta 8.3^+$ enriched) with vaccination or convalescent serum therapy. Our data also suggest that influenza vaccination improves the immune response to subsequent infection by driving a subset of $V\beta 8.3^+$ $CD8^+$ T cells to take on a tissue resident memory-like differentiation state. Tissue-resident memory cells allow for control of broad viral serotypes against several viruses ranging from influenza to SARS-COV-2⁶⁵. The $V\beta 8.3^+$ T_{rm} -like cells were the most expanded population during infection in mice that were previously vaccinated. This suggests that this population of $CD8^+$ T cells expressing the $V\beta 8.3$ chain are poised to become memory cells, while populations expressing other $V\beta$ chains are either less efficient at differentiating toward a T_{rm} phenotype or are outcompeted by $V\beta 8.3^+$ T_{rm} -like cells upon rechallenge. Such differences in differentiation capacities have been observed previously for effector $CD8^+$ T cells during respiratory infections, where memory cell selection was driven by TCR avidity for peptide-MHC⁶⁶. Further studies must be conducted to determine if this $V\beta 8.3^+$ clonal population is critical for improved protection from disease upon rechallenge with the same serotype, and potentially against different serotypes. More broadly, it should be investigated why this particular clonal population is favored to differentiate toward a tissue resident memory-like state.

Convalescent serum therapy has been utilized to treat several respiratory viral infections due to the presence of neutralizing antibodies that can limit viral spread and improve viral phagocytosis by APCs⁶⁷. We were interested in analyzing the effect of this therapy on the clonal T cell response since it has been shown previously that convalescent plasma therapy from mild or severe COVID-19 patients can have differing effects on the percentage of activated effector T cells and memory T cells⁶⁸. Furthermore,

the timing of convalescent serum therapy has also been shown to correlate with its efficacy in preventing severe disease⁶⁹⁻⁷⁴. Indeed, treatment of mice with convalescent serum during the earliest stages of infection broadly restricted the expansion of inflammatory effector T cell populations in the lungs and reduced disease severity (**Figure 2-16c**). However, convalescent serum 4 hours after infection did lead to the increased expansion of the V β 8.3⁺ CD8⁺ T cells, which exhibited an effector memory phenotype. This may indicate that very early convalescent serum therapies directly impact viral load through antibody activities, but also impact the activation and differentiation of specific CD8⁺ T cell clones against the virus. The impact of antiviral antibody on T cell differentiation has been hypothesized previously and attributed to various effects of the presence of antibodies early, such as reducing the levels of circulating inflammatory cytokines, which could impact T cell response and disease severity, or antibody-mediated presentation of antigen that leads to expansion of T cells with particular specificities^{72,73,60}. However, it is challenging to draw direct parallels between observations in patients or other animal models with different respiratory viruses due to the difference in viruses, the physiology of infection and immune responses in each species, and the delivery and dosing of virus in each experimental model^{75,76}. Nevertheless, our results do concur with a series of studies that clearly show that earlier antibody treatment is more effective in controlling severe respiratory viral disease. We show that early treatment does impact the repertoire and differentiation of specific T cells, and thus our model will provide a new system to dissect whether altered T cell responses with convalescent serum therapy contribute to reduced disease severity.

Importantly, an advantage of this CyTOF approach is its capacity to immediately be translated to the setting of human diseases. Human V α and V β chain-specific antibodies are commercially available, making it possible to identify clonal T cell responses to chronic infections, new pathogens, microbiota, and cancer in humans⁷⁷⁻⁷⁹. Additionally, we found that this approach can identify V β chain-expressing Tregs that expand during infection, which has been difficult to do historically⁸⁰. This approach can also be used to rapidly identify antigens in several human diseases to inform the development of vaccines to treat cancers or infections. This would complement the use of strategies such as CITE-seq and scTCR-seq, which have been used recently to understand the behavior of clones in cancer patients in response to checkpoint blockade immunotherapy^{81,82}. Importantly, our CyTOF approach can be used as a preliminary screening method for identifying T cell populations of interest, independent of the identity of their antigenic target, prior to TCR sequencing of populations enriched for expansion during an immune response⁴⁴. The scalability of our CyTOF approach should allow for broader analyses across tissues, time points, or therapeutic perturbations prior to TCR sequencing experiments, vastly improving sequencing efficiency and cost.

In summary, we report a new application of CyTOF to quickly identify and phenotype clonal T cell populations across several disease models. In addition, we used these common V β and V α chains to track the states of particular clonal populations of interest during different therapeutic contexts, such as vaccinations and convalescent serum therapy for respiratory infection with flu. Collectively, our study provides a new approach for identifying and phenotyping relevant T cell populations containing clones

specific for antigens across multiple disease models that can be used with the aim of improving the efficacy of immunotherapies.

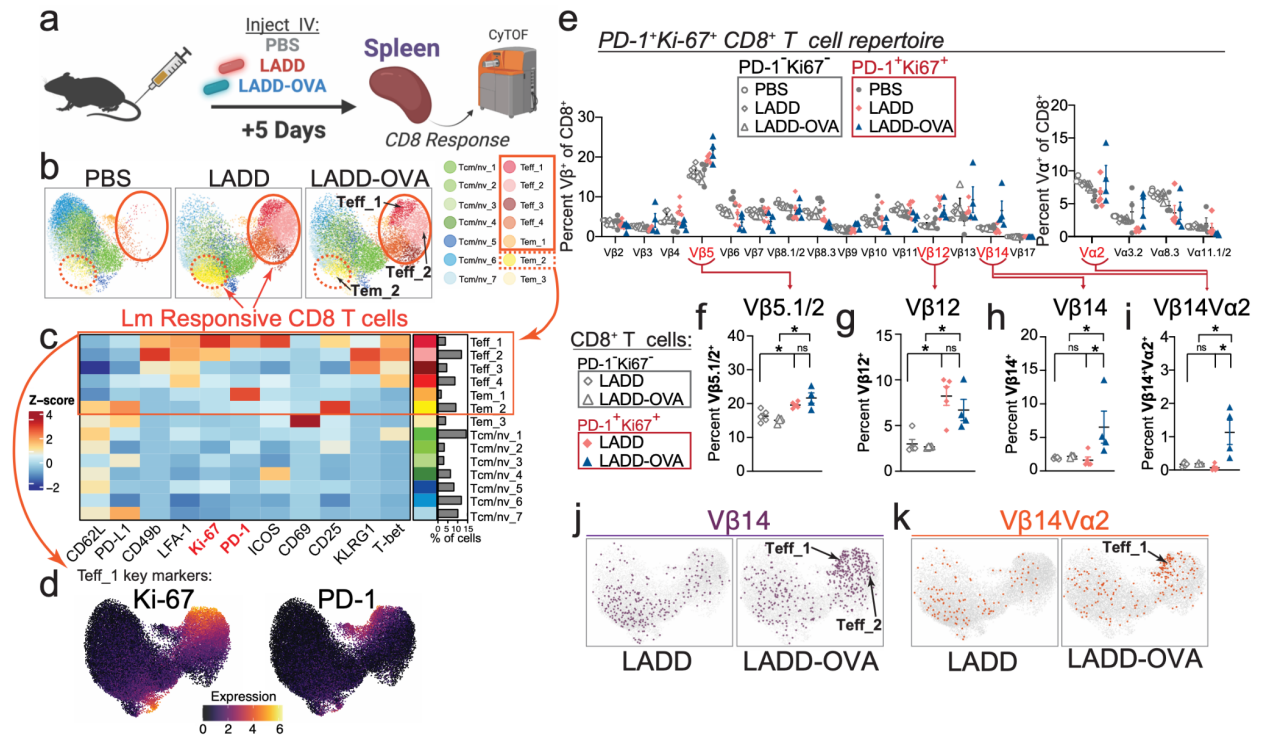


Figure 2.1 | Tracking the phenotypes of clonal T cell responses against attenuated *Listeria* (LADD) with CyTOF. (a) C57BL/6J mice were injected with *LADD*, *LADD-OVA*, or *PBS* intravenously (i.v.) and after 5 days splenocytes were analyzed by CyTOF. (b) UMAP visualization of CD8⁺ T cell clusters on expression of non-TCR proteins. (c) Heatmap of non-TCR protein expression annotated by cluster and the percentage of cells falling into each cluster. (d) UMAP visualization of CD8⁺ T cells colored by the expression of PD-1 and Ki-67 in *LADD*-infected mice. (e) Frequency of PD-1⁺Ki-67⁺ and PD-1⁻Ki-67⁻ CD8⁺ T cells using specific TCR Vβ (left) or Vα chains (right) in response to *PBS*, *LADD*, or *LADD-OVA*. (f-i) Frequency of Vβ5.1/2⁺ (f), Vβ12⁺ (g), Vβ14⁺ (h), or Vβ14⁺Vα2⁺ among PD-1⁺Ki-67⁺ versus PD-1⁻Ki-67⁻ CD8⁺ T cells in *LADD* or *LADD-OVA* infected mice. (j-k) UMAP visualization of pooled CD8⁺ T cells colored by the expression of Vβ14⁺ (j) and Vβ14⁺Vα2⁺ (k) in *LADD* or *LADD-OVA* infected mice. Results from n=5 for *PBS*, n=4 for *LADD*, n=4 for *LADD-OVA*, *P<0.05, **P<0.01, ***P<0.001 by unpaired two-tailed Student's t-test, mean ± s.e.m.

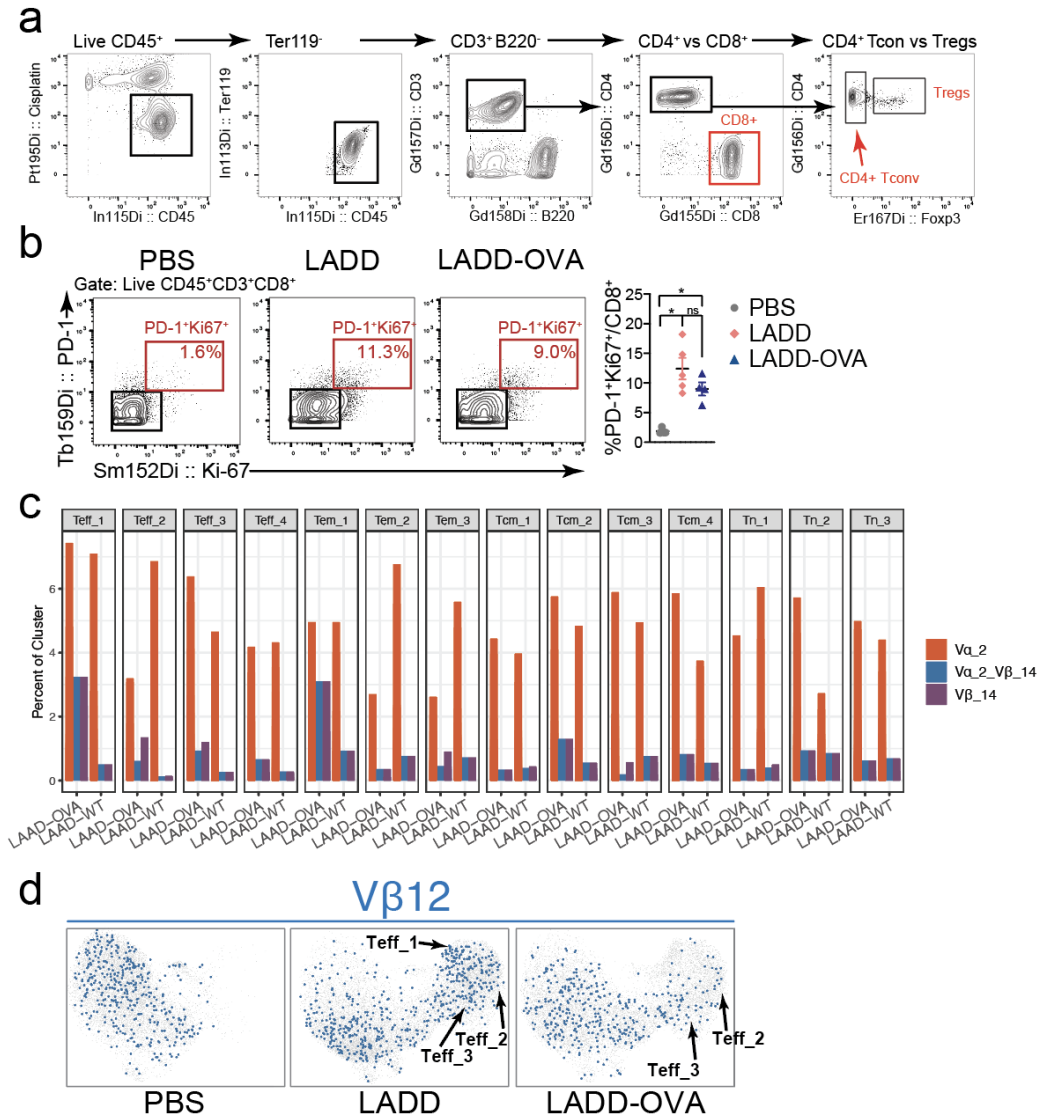


Figure 2.2 | Tracking a *Listeria*-specific CD8⁺ T cell response against *LADD* by TCR use and phenotyping with CyTOF. (a) Gating strategy for all CyTOF analyses preceding input into semi-supervised clonotype assignment script. (b) Representative flow plots and quantification of proliferating CD8⁺ T cells from spleens 5 days after *LADD*, *LADD-OVA*, or *PBS* injection IV. (c) Bar plot of Vα₂, Vβ₁₄, and Vα₂-Vβ₁₄ percentages in each cluster for conditions *LAAD* and *LAAD-OVA*. (d) UMAP visualization of pooled CD8⁺ T cells colored by the expression of Vβ₁₂⁺ in *LADD*, *LADD-OVA*, or *PBS* infected mice. For all plots, **P<0.05, **P<0.01, ***P<0.001 by unpaired two-tailed student's T-test, mean ± s.e.m.

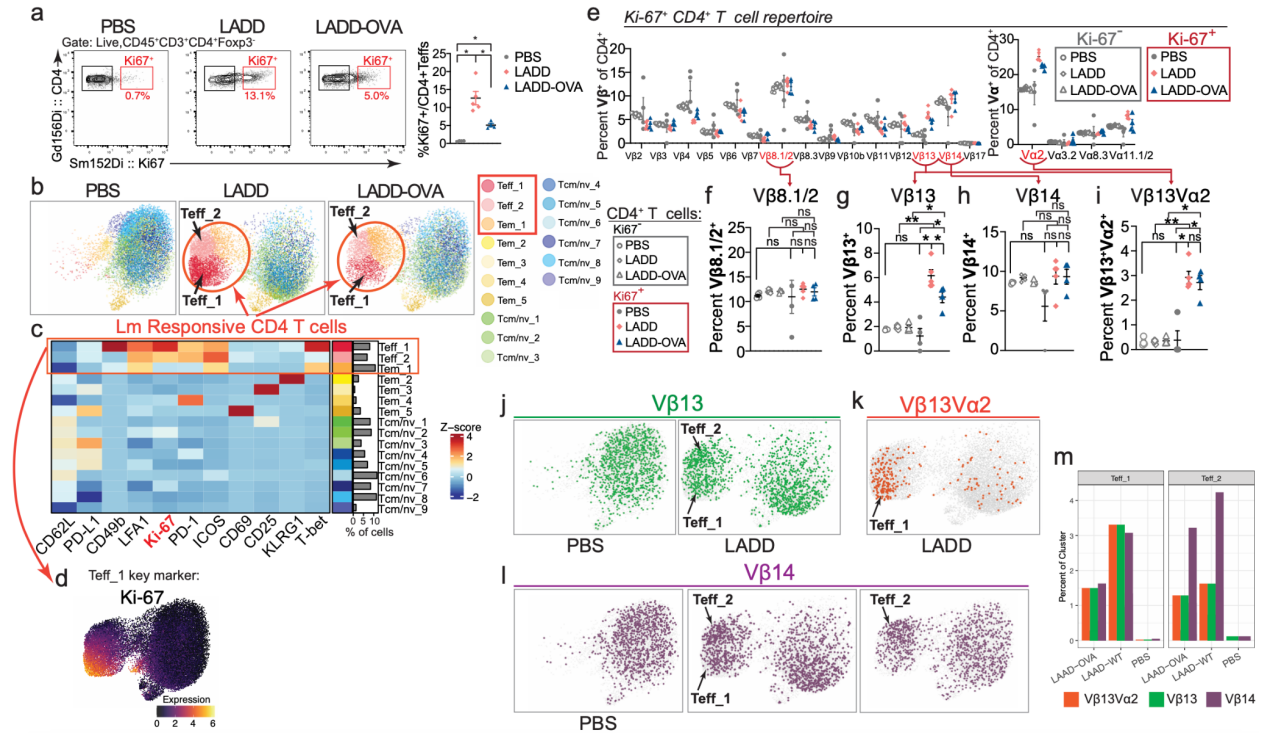


Figure 2.3 | Tracking *Listeria*-specific CD4⁺ T cells against *LADD* by TCR use and phenotyping with CyTOF. (a) Representative flow plots and quantification of proliferating (Ki-67⁺) CD4⁺ T cells from spleen 5 days after *LADD*, *LADD-OVA*, or *PBS* injection. (b) UMAP visualization of CD4⁺ T conventional (non-Treg) cell clusters based on expression of non-TCR proteins. (c) Heatmap of non-TCR protein expression annotated by cluster and fraction of cells falling into each cluster. (d) UMAP visualization of CD4⁺ T cells colored by the expression of Ki-67 in *Lm*-infected mice. (e) Frequency of Ki-67⁺ and Ki-67⁻ CD4⁺ T cells using specific TCR Vβ (left) or Vα chains (right) in response to *PBS*, *LADD*, or *LADD-OVA*. (f-h) Frequency of Vβ13⁺ (f), Vβ14⁺ (g), or Vβ13⁺Vα2⁺ among Ki-67⁺ (h) versus Ki-67⁻ CD4⁺ T cells in *Lm* or *LADD-OVA* infected mice. (i-k) UMAP visualization of pooled CD4⁺ T cells colored by the expression of Vβ13⁺ (i), Vβ13⁺Vα2⁺ (j), and Vβ14 (k) in *LADD*, *LADD-OVA*, or *PBS*-injected mice. (m) Bar plot of Vβ13⁺, Vβ13⁺Vα2⁺, and Vβ14⁺ percentages in Teff clusters. Results from n=5 for *PBS*, n=4 for *LADD*, n=4 for *LADD-OVA*, *P<0.05, **P<0.01, ***P<0.001 by unpaired two-tailed Student's t-test, mean ± s.e.m.

(Figure caption continued from the previous page.) analyzed by peptide restimulation or tetramer staining. (b) Representative flow plots and quantification of fold-enrichment in V β -chain usage by CD8⁺ T cells with OVA (SIINFEKL) peptide restimulation. (c) Representative flow plots and quantification for fold-enrichment using SIINFEKL-loaded H-2K^b tetramer staining. (d) Representative flow plots and quantification of fold-enrichment in V β -chain usage by CD8⁺ T cells with LLO1 (VAYGRQVYL) peptide restimulation. (e) Schematic summarizing CD8⁺ T cells using specific V β -chains enriched to recognize specific antigens from LADD. (f) Representative flow plots and quantification of fold-enrichment in V β -chain usage by CD4⁺ T cells with LLO2 (NEKYAQAYPNVS) peptide restimulation. (g) Representative flow plots and quantification for fold-enrichment in tetramer assay using IA^b-NEKYAQAYPNVS tetramer staining. (h) Representative flow plots and quantification of fold-enrichment in V β -chain usage by CD4⁺ T cells with LLO3 (AFDAAVSGKSVS) peptide restimulation. (i) Schematic summarizing CD4⁺ T cells using specific V β -chains enriched to recognize specific antigens from LADD. Results from n=2 independent experiments, *P<0.05, **P<0.01, ***P<0.001 by One-Way ANOVA for peptide restimulation assays and unpaired two-tailed Student's t-test for tetramer assays, mean \pm s.e.m.

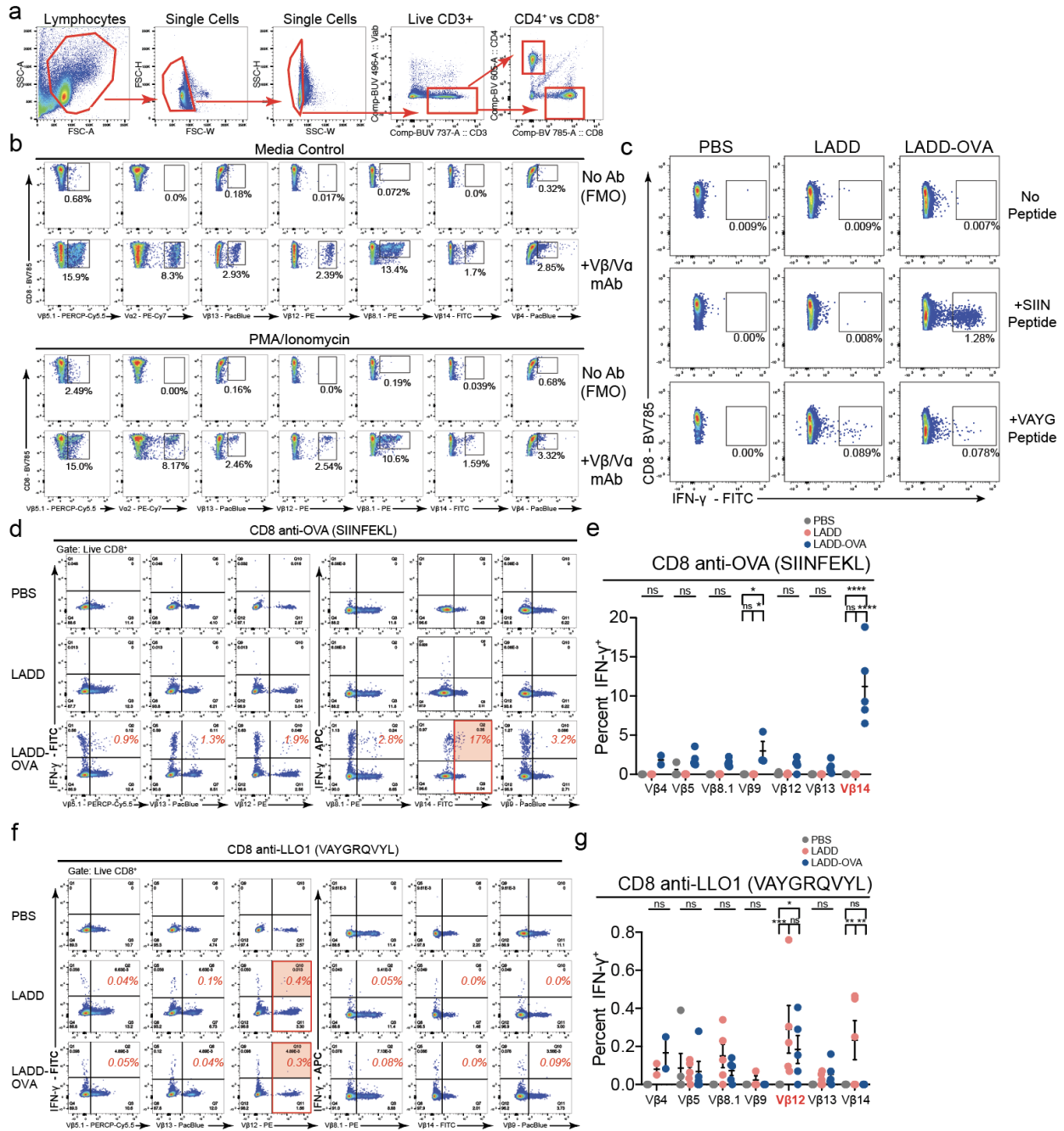


Figure 2.5 | CD8 response to Lm- and OVA-derived epitopes. (a) Manual gating strategy for all CD8 and CD4 Teff subsets. (b) FMO controls for all fluorescent-conjugated Vβ and Vα antibodies in naive splenocytes +/- stimulation with PMA + ionomycin (c) Frequency of IFN γ ⁺ CD8 T cells in splenocytes in unstimulated controls versus peptide conditions. (d) Representative flow plots of IFN γ ⁺ CD8s versus respective Vβ chains in splenocytes (*Figure caption continued on the next page.*)

(Figure caption continued from the previous page.) stimulated with SIINFEKL peptide. (e) Percent of IFN- γ ⁺ for respective V β ⁺ CD8s in splenocytes stimulated with SIINFEKL peptide. (f) Representative flow plots of IFN- γ ⁺ CD8s versus respective V β chains in splenocytes stimulated with LLO1 peptide. (g) Percent of IFN- γ ⁺ for respective V β ⁺ CD8 in splenocytes stimulated with LLO1 peptide. Results from n=5 for PBS, n=4 for *LADD*, n=4 for *LADD-OVA*, *P<0.05, **P<0.01, ***P<0.001 by unpaired two-tailed Student's t-test, mean \pm s.e.m.

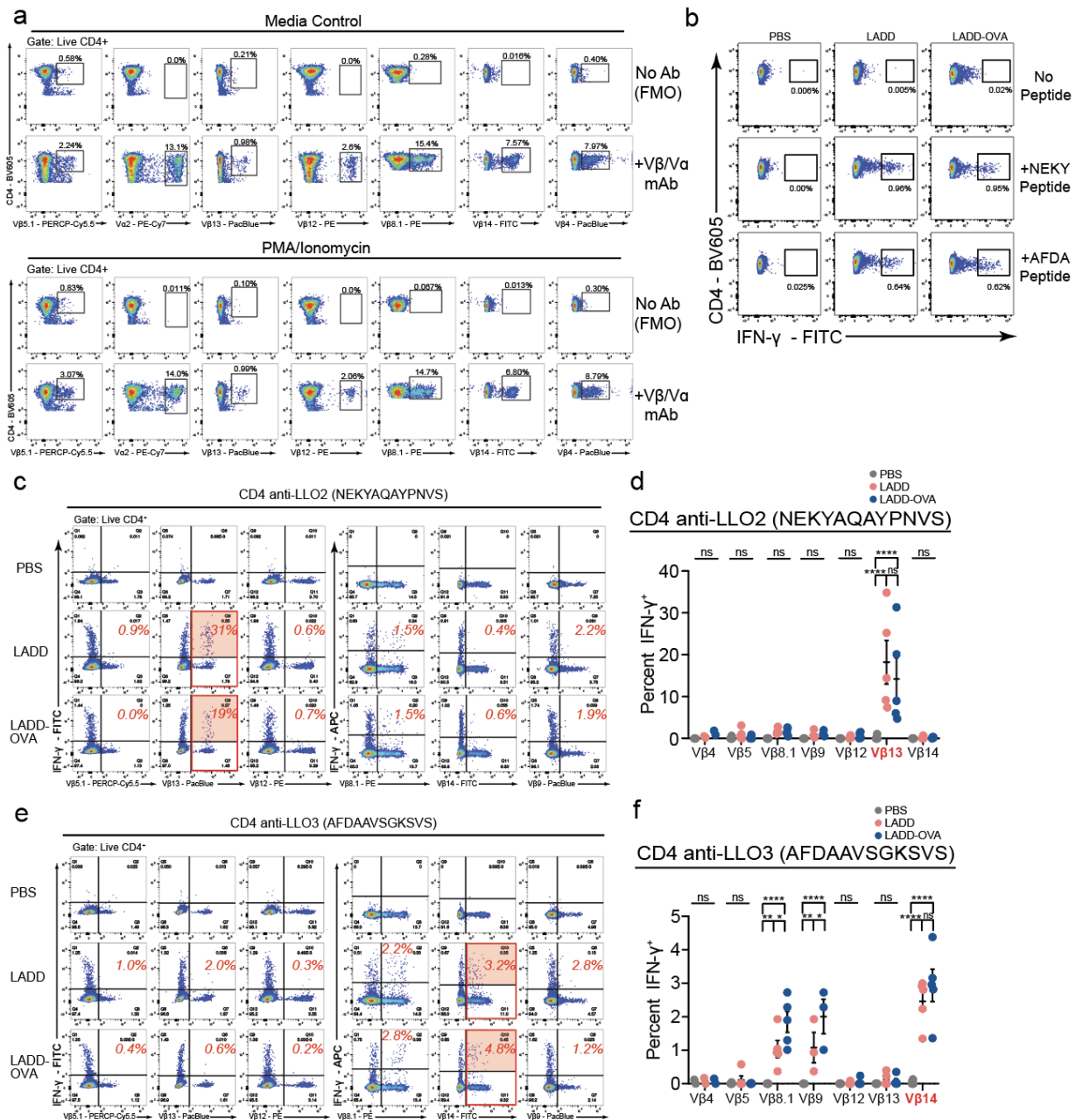


Figure 2.6 | CD4 T cell response to *Lm*-derived epitopes. (a) FMO controls for all fluorescent-conjugated Vβ and Vα antibodies in naive splenocytes +/- stimulation with PMA + ionomycin. (b) Frequency of IFN-γ⁺ CD4s in splenocytes in unstimulated controls versus peptide conditions. (c) Representative flow plots of IFN-γ⁺ CD4 T cells versus respective Vβ chains in splenocytes stimulated with LLO2 peptide. (d) Percent of IFN-γ⁺ for respective Vβ⁺ CD4 T cells in splenocytes stimulated with LLO2 peptide. (e) Representative flow plots of (*Figure caption continued on the next page.*)

(Figure caption continued from the previous page.) IFN- γ ⁺ CD4 T cells versus respective V β chains in splenocytes stimulated with LLO3 peptide. (f) Percentage of IFN- γ ⁺ for respective V β ⁺ CD4 T cells in splenocytes stimulated with LLO3 peptide. Results from n=5 for PBS, n=4 for *LADD*, n=4 for *LADD-OVA*, *P<0.05, **P<0.01, ***P<0.001 by unpaired two-tailed Student's t-test, mean \pm s.e.m.

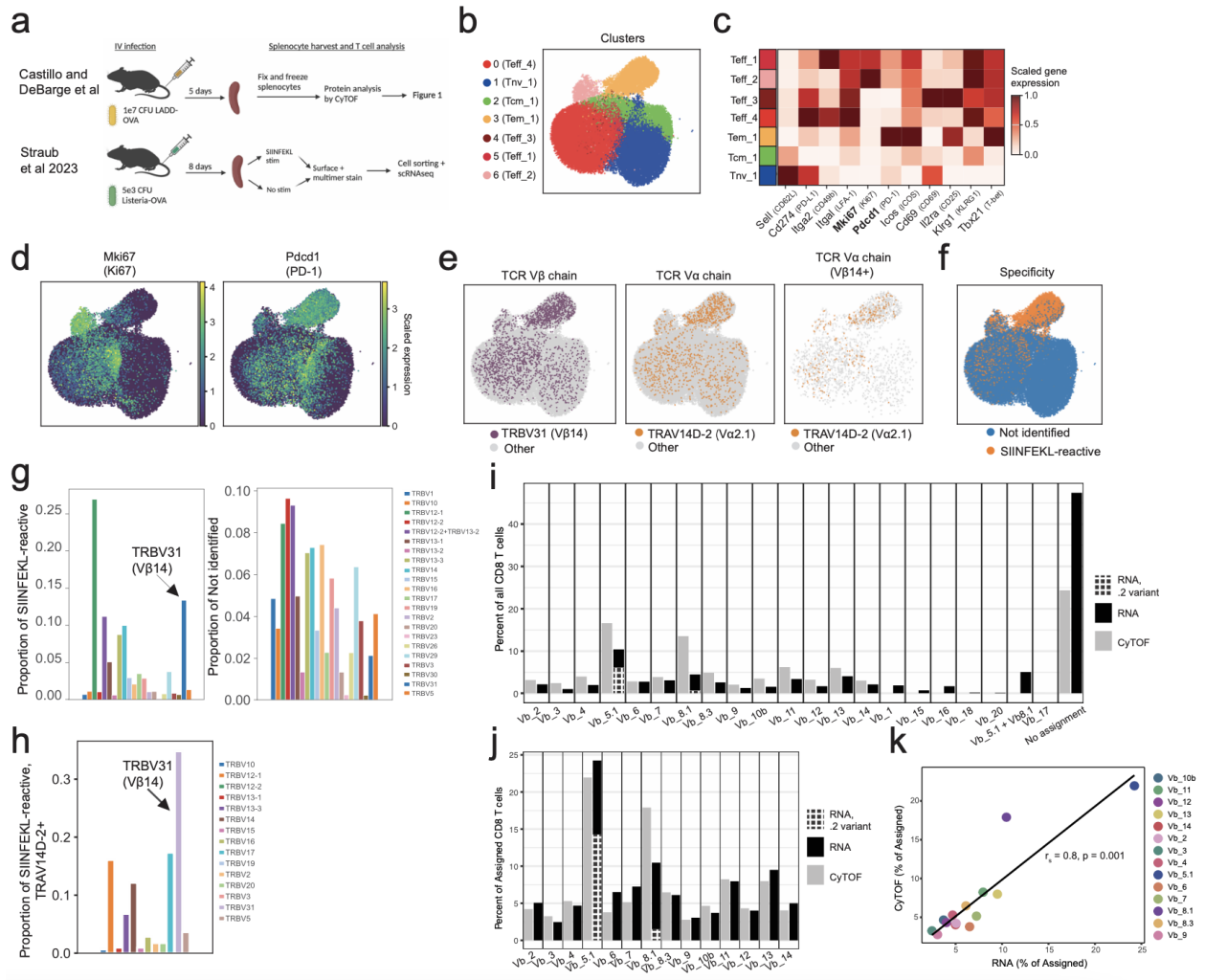


Figure 2.7 | Comparative analysis of V β 14+Va2+ CD8 T cell expansion with scRNA-seq during *Lm* infection. (a) Schematic comparison of approach used in this study compared to Straub *et al.* 2023. (b) Re-annotated clusters identified by Straub *et al.* plotted in UMAP space. (c) Scaled gene expression within the scRNA-seq dataset of genes encoding the proteins measured in Fig. 1, stratified by cluster. (d) UMAP visualization of all clustered cells colored by Ki67 or PD-1 gene expression. (e) UMAP visualization of all clustered cells colored by TRBV31 assignment or TRAV14D-2 assignment (**left**), and UMAP visualization of TRBV31-assigned cells colored by TRAV14D-2 assignment (**right**). (f) UMAP visualization of all clustered cells colored by identified specificity. (g) Quantification of TRBV gene usage among SIINFEKL-reactive cells (right) or of cells of unidentified reactivity (left). (h) Quantification of TRBV gene usage among SIINFEKL-reactive (*Figure caption continued on the next page.*)

(Figure caption continued from the previous page.) cells expressing TRAV14D-2. (i) Quantification of TRBV/V β chain assignment of all CD8 T cells as measured by CyTOF or scRNA-seq. (j) Quantification of the TRBV/V β chains measured in the CyTOF assay of all CD8 T cells that were assigned a TRBV/V β chain by either CyTOF or scRNA-seq. (k) Spearman correlation analysis of data shown in (j).

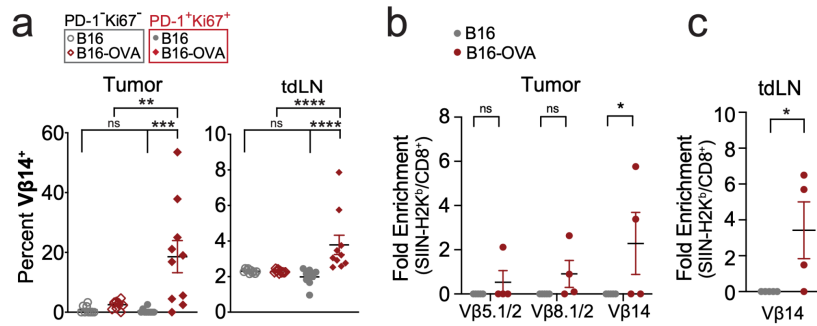


Figure 2.8 | Activated Vβ14⁺ CD8⁺ T cells expand in OVA-expressing tumor model.

(a) Frequencies of Vβ14⁺ CD8⁺ T cells in B16F10 tumors (+/- OVA expression) and tumor-draining lymph nodes (tdLN) separated by non-proliferating (PD-1⁻Ki67⁻) vs. proliferating (PD-1⁺Ki67⁺) cells. (b) Quantification for fold-enrichment of H2-K^b-SIINFEKL tetramer staining in tumors from B16F10 and B16F10-OVA tumor-bearing mice. (c) As in (b) except from tdLN. Results from n=10 for B16F10, n=10 for B16F10-OVA for CyTOF analysis and n=5 for B16F10, n=4 for B16F10-OVA for tetramer analysis, *P<0.05, **P<0.01, ***P<0.001 by unpaired two-tailed Student's t-test for flow analysis in tumors and tdLNs and one-way ANOVA for tetramer analysis in tumors, mean ± s.e.m.

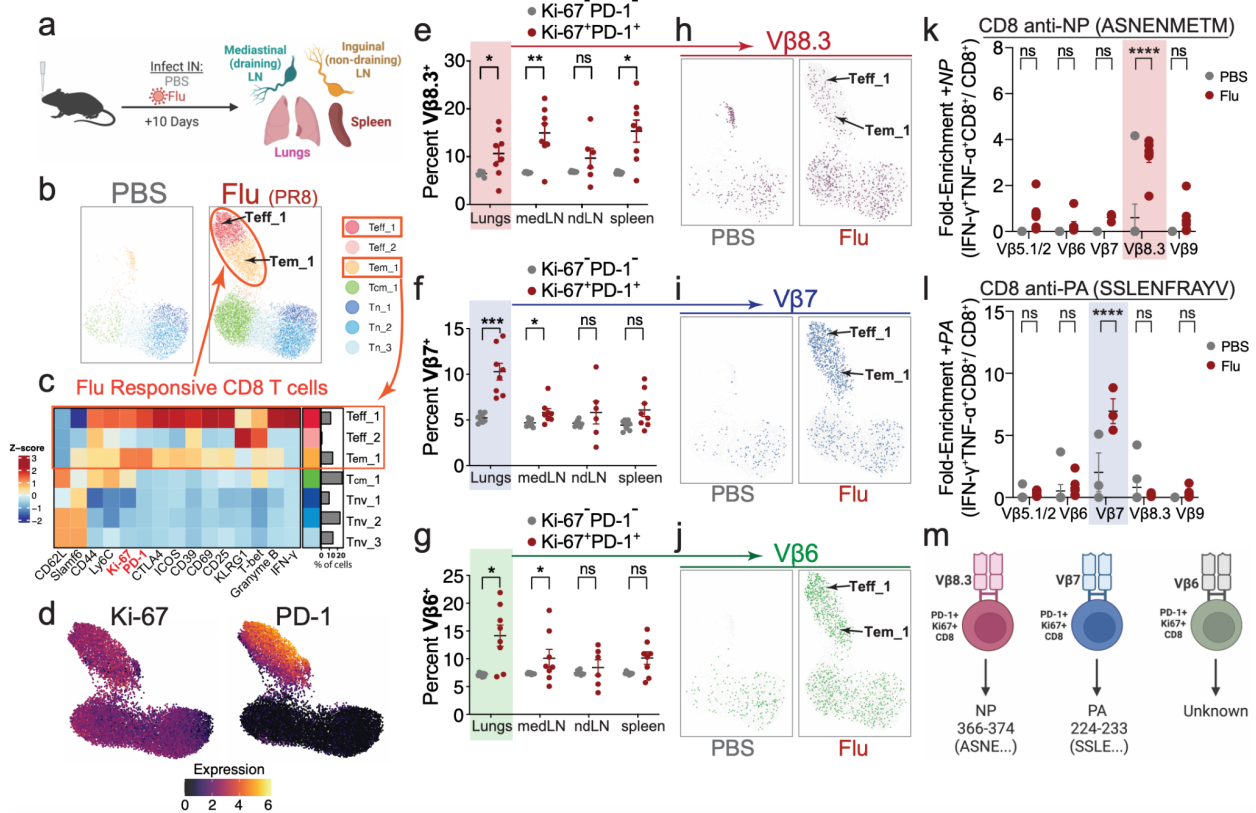


Figure 2.9 | Tracking the expansion and recognition of CD8⁺ T cells specific for influenza antigens across multiple tissues. (a) C57BL/6J mice were infected with PR8 H1N1 influenza (Flu) intranasally (IN), and indicated tissues were analyzed for T cell responses. (b) UMAP visualization of CD8⁺ T cell clusters based on expression of non-TCR proteins. (c) Heatmap of non-TCR protein expression annotated by cluster and fraction of cells falling into each cluster. (d) UMAP visualization of CD8⁺ T cells colored by the expression Ki-67 and PD-1 in flu-infected mice. (e-g) Comparison of the frequencies of CD8⁺ T cells using Vβ8.3 (e), Vβ7 (f), and Vβ6 (g) in non-proliferating (PD-1⁻Ki-67⁻) and proliferating (PD-1⁺Ki-67⁺) cells across tissues of flu-infected mice. (h-j) UMAP visualization of pooled CD8⁺ T cells colored by the expression of Vβ8.3 (h), Vβ7 (i), and Vβ6 (j) in PBS versus flu-infected mice. (k) Quantification of fold-enrichment in Vβ-chain usage by CD8⁺ T cells stimulated with the PR8 NP peptide (ASNENMETM). (l) Quantification of fold-enrichment in Vβ-chain usage by CD8⁺ T cells stimulated with the PR8 PA peptide (SSLENFRAYV). (m) Schematic summarizing CD8⁺ T cells using specific Vβ-chains enriched to recognize specific antigens from flu. Results from n=7 for PBS, n=7 for PR8, (Figure caption continued on the next page.)

(Figure caption continued from the previous page.) *P<0.05, **P<0.01, ***P<0.001 by unpaired two-tailed Student's t-test for CyTOF analysis and one-way ANOVA for peptide restimulation assay, mean \pm s.e.m.

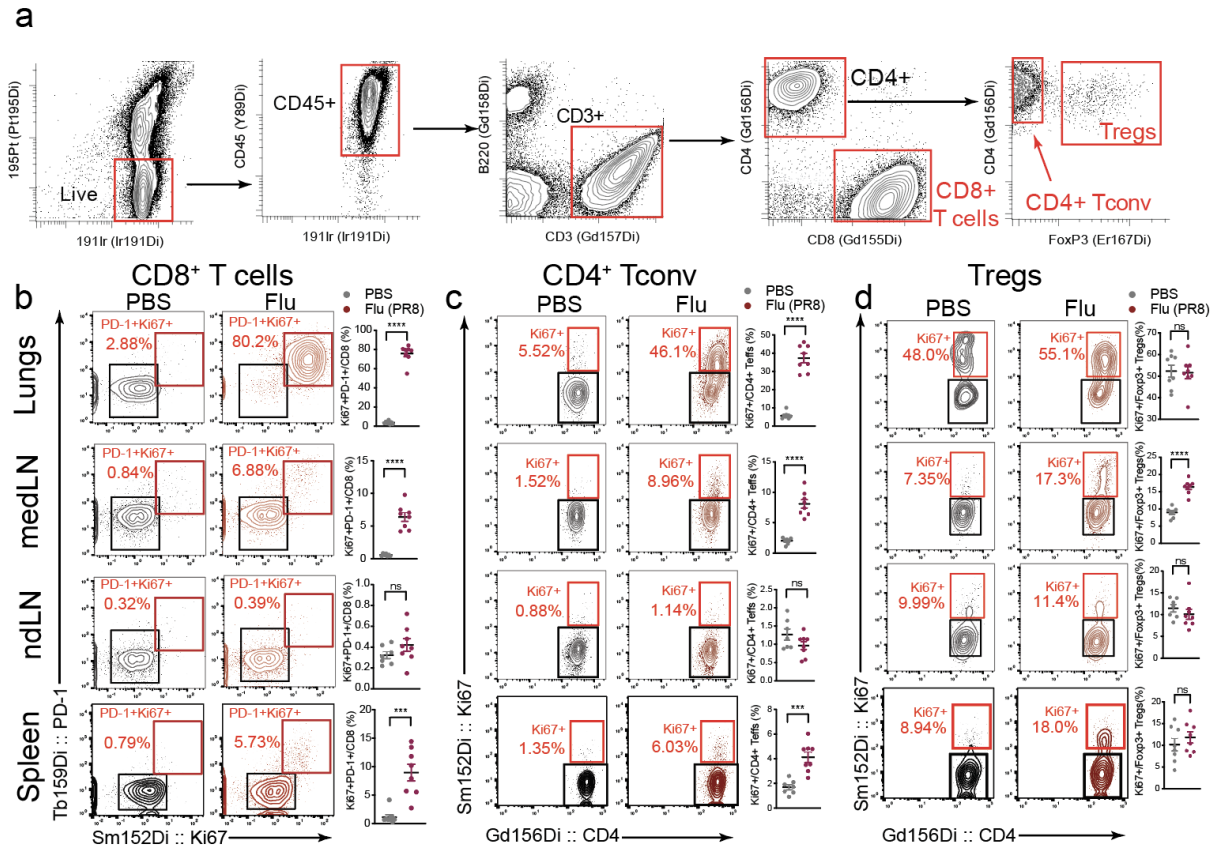


Figure 2.10 | Expansion and activation of T cell subsets during flu infection across multiple tissues. (a) Gating strategy for all CyTOF analyses preceding input into semi-supervised clonotype assignment script. (b) Representative flow plots and quantification of proliferating (PD-1⁺Ki67⁺) CD8⁺ T cells. (c) Representative flow plots and quantification of proliferating (Ki67⁺) Foxp3⁻ CD4⁺ Teff cells. (d) Representative flow plots and quantification of proliferating (Ki67⁺) Foxp3⁺ Tregs. For all plots, **P<0.05, ***P<0.01, ****P<0.001 by one-way ANOVA, mean ± s.e.m.

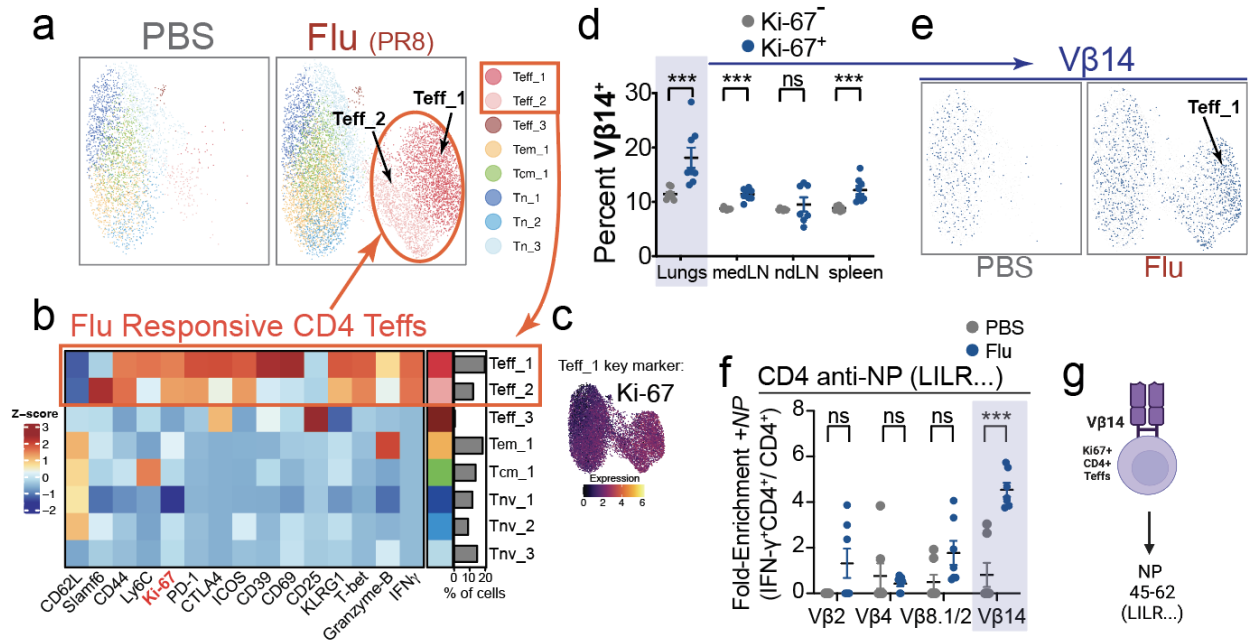


Figure 2.11 | Identification of flu NP-specific Vβ14⁺ CD4⁺ T cells. (a) UMAP visualization of CD4⁺ T conventional (non-Treg) cell clusters based on expression of non-TCR proteins. (b) Heatmap of non-TCR protein expression annotated by cluster and fraction of cells falling into each cluster. (c) UMAP visualization of CD4⁺ T cells colored by the expression Ki-67 in flu-infected mice. (d) Frequencies of Vβ14⁺ CD4⁺ T cells in non-proliferating (Ki-67⁻) vs. proliferating (Ki-67⁺) cells across indicated tissues. (e) UMAP visualization of pooled CD4⁺ T cells colored by Vβ14 expression. (f) Quantification of fold-enrichment in Vβ-chain usage by CD4⁺ T cells stimulated with the PR8 NP peptide (LILRGSVAHKSCLPACV). (g) Schematic summarizing that Vβ14⁺ CD4⁺ T cells are enriched to recognize PR8 NP antigen from flu. Results from n=7 for PBS, n=7 for PR8, *P<0.05, **P<0.01, ***P<0.001 by unpaired two-tailed Student's t-test, mean ± s.e.m.

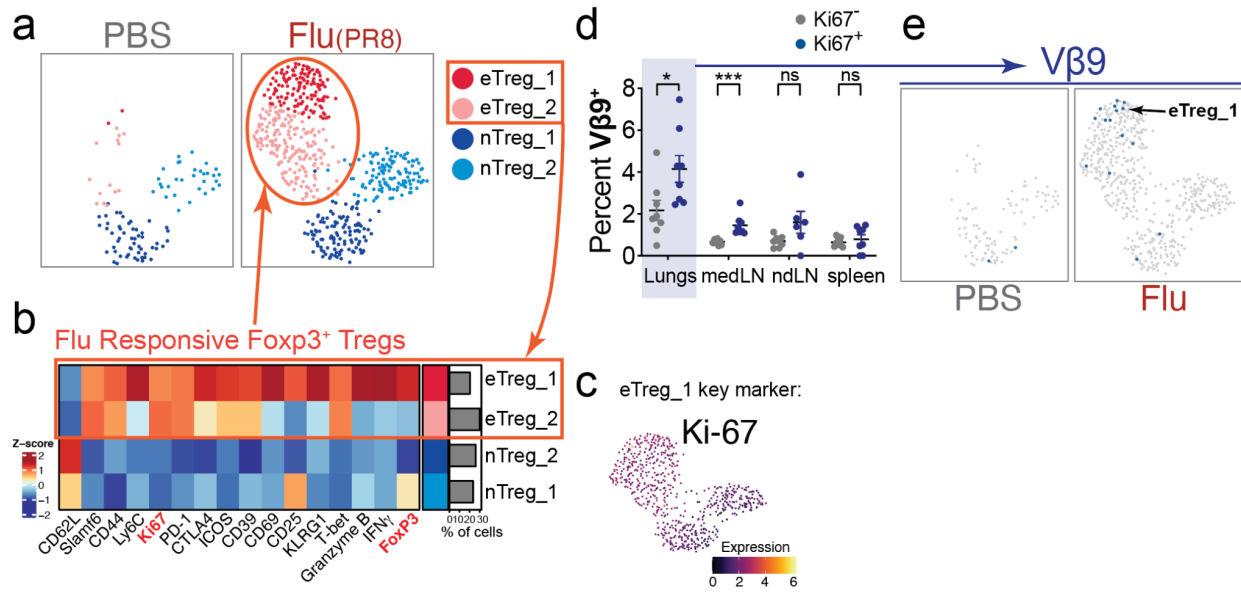


Figure 2.12 | Identification and phenotyping of Vβ9+ Treg expansion after flu infection. (a) UMAP of Treg populations based on expression of non-TCR proteins. (b) Heatmap of non-TCR protein expression annotated by cluster and fraction of cells falling into each cluster. (c) UMAP visualization of Tregs colored by the expression Ki-67 in flu-infected mice. (d) Frequencies of Vβ9+ Tregs in non-proliferating (Ki-67-) vs. proliferating (Ki-67+) cells across indicated tissues. (e) UMAP visualization of pooled Tregs from PBS or flu-infected mice colored by Vβ9 expression. Results from n=7 for PBS, n=7 for PR8, *P<0.05, **P<0.01, ***P<0.001 by unpaired two-tailed Student's t-test, mean ± s.e.m.

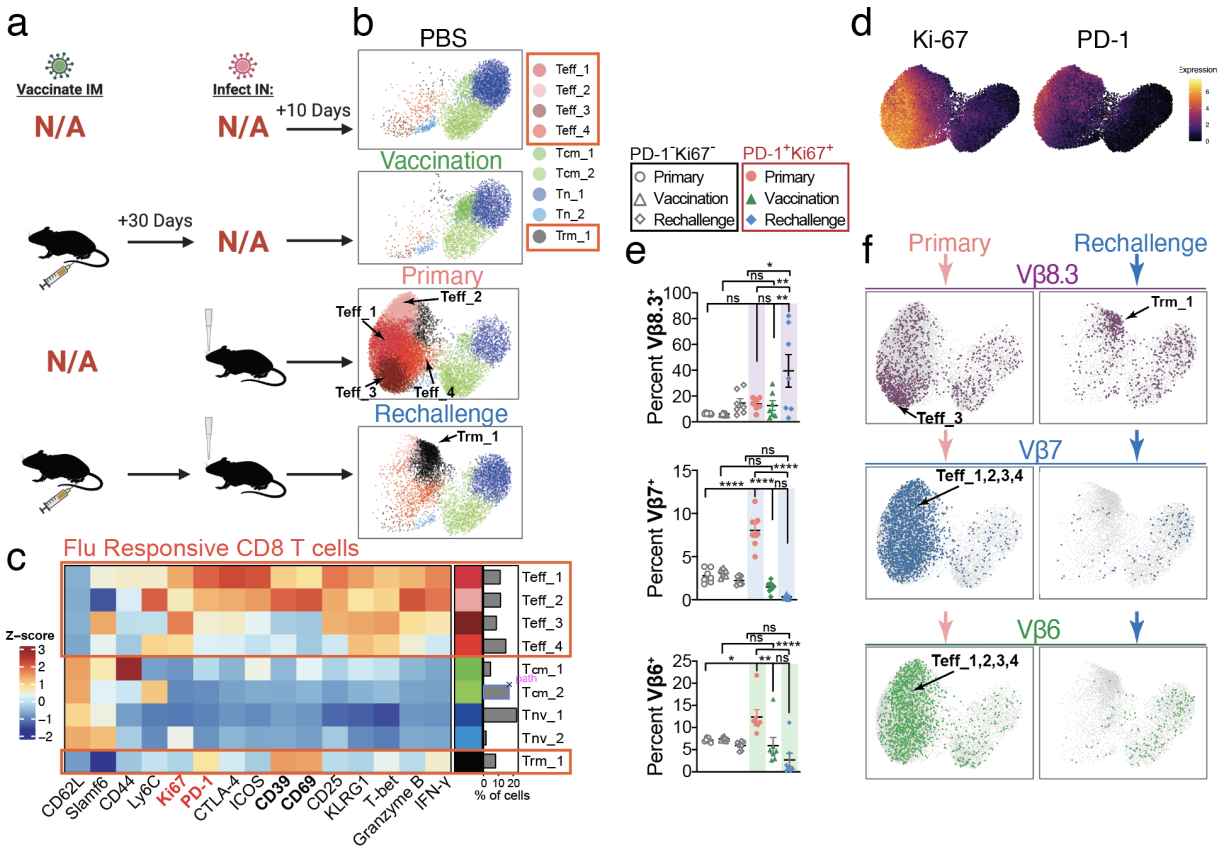


Figure 2.13 | Vβ8.3+ CD8s have different phenotypes and frequencies in the context of influenza immunization model. (a) C57BL/6J mice were vaccinated intramuscularly (IM) and later rechallenged intranasally (IN), vaccinated IM but not rechallenged, challenged with flu (IN) without prior vaccination, or injected with a PBS vehicle control. (b) UMAP visualization of CD8⁺ T cells based on expression of non-TCR proteins. (c) Heatmap of non-TCR protein expression annotated by cluster and fraction of cells falling into each cluster. (d) UMAP visualization of CD8⁺ T cells colored by the expression Ki-67 and PD-1 from all cohorts of mice. (e) Comparison of the frequencies of CD8⁺ T cells using Vβ8.3, Vβ7, and Vβ6 in non-proliferating (PD-1⁻Ki-67⁻) and proliferating (PD-1⁺Ki-67⁺) cells in the lungs of primary, vaccinated, or rechallenged mice. (f) UMAP visualization of pooled CD8⁺ T cells from primary or rechallenged mice colored by the expression of Vβ8.3, Vβ7, and Vβ6. Results from n=7 for PBS, n=7 for Primary, n=7 for Vaccination, n=7 for Rechallenge *P<0.05, **P<0.01, ***P<0.001 by one-way ANOVA, mean ± s.e.m.

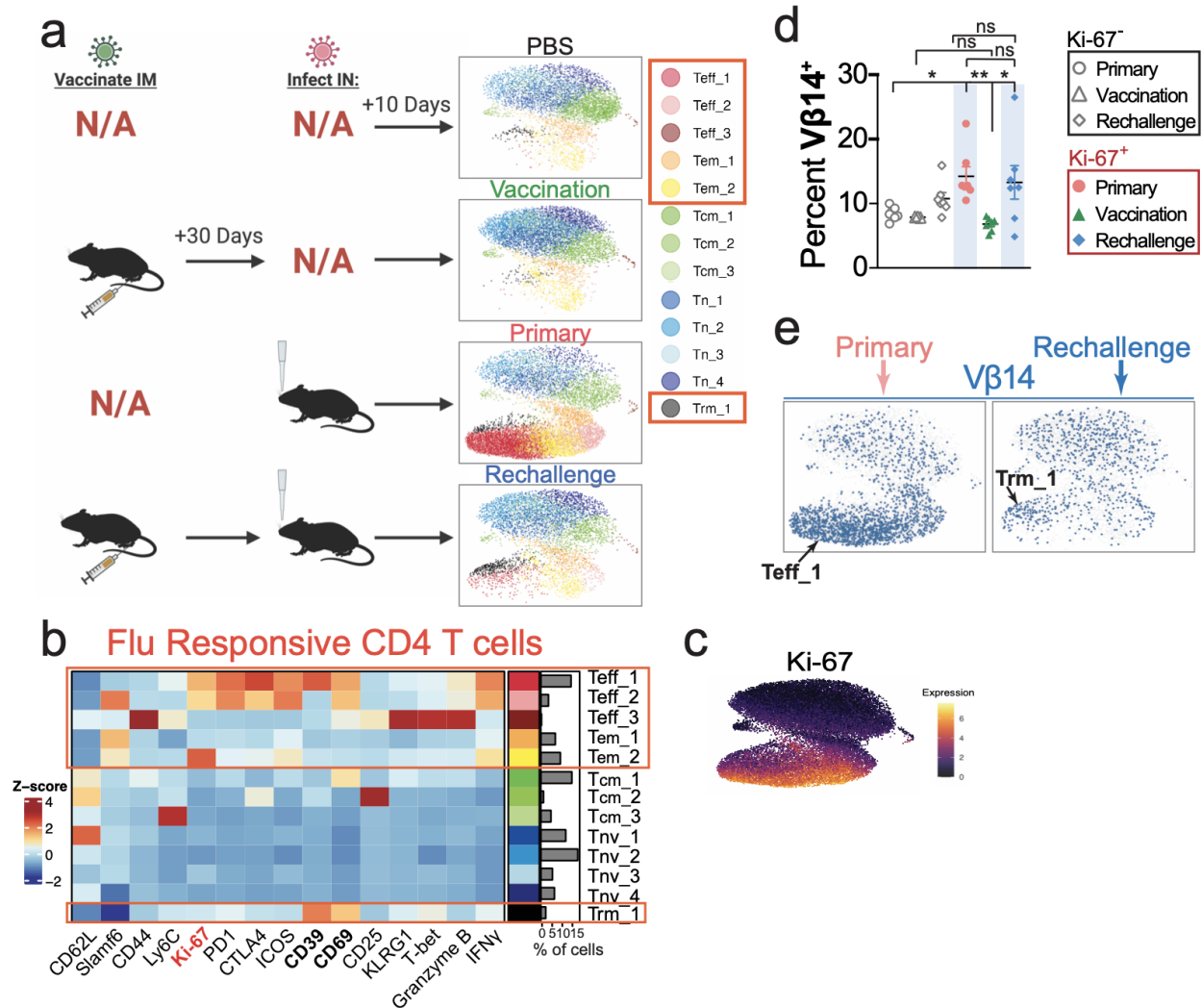


Figure 2.14 | *Flu*-specific conventional CD4⁺ T cell differentiation, but not repertoire, is altered by vaccination. (a) UMAP visualization of CD4⁺ T conventional (non-Treg) cell clusters based on expression of non-TCR proteins. (b) Heatmap of non-TCR protein expression annotated by cluster and fraction of cells falling into each cluster. (c) UMAP visualization of CD4⁺ T cells colored by the expression Ki-67 from all cohorts of mice. (d) Frequencies of V β 14⁺ CD4 T cells in non-proliferating (Ki-67⁻) vs. proliferating (Ki-67⁺) cells in lungs of primary, vaccinated, or rechallenge mice. (e) UMAP visualization of pooled CD4⁺ T cells from primary or rechallenge mice colored by V β 14 expression. Results from n=7 for PBS, n=7 for PR8, *P<0.05, **P<0.01, ***P<0.001 by one-way ANOVA, mean \pm s.e.m.

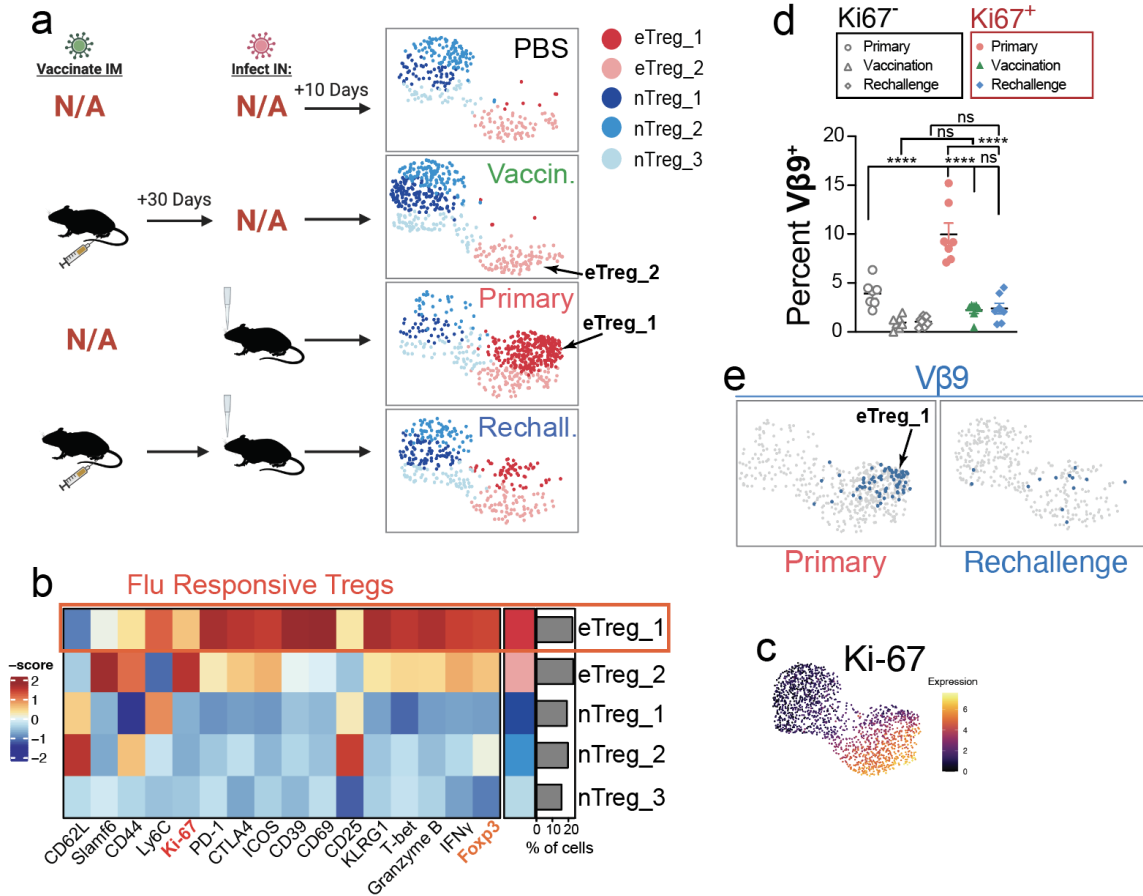


Figure 2.15 | $V\beta 9^+$ Treg clonal population is only present in the setting of a primary infection. (a) UMAP of Treg populations based on the expression of non-TCR proteins. (b) Heatmap of non-TCR protein expression annotated by cluster and fraction of cells falling into each cluster. (c) UMAP visualization of Tregs colored by the expression Ki-67 from all cohorts of mice. (d) Frequencies of $V\beta 9^+$ Tregs in non-proliferating (Ki-67⁻) vs. proliferating (Ki-67⁺) cells in lungs of primary, vaccinated, or rechallenged mice. (e) UMAP visualization of pooled Tregs from primary or rechallenged mice colored by $V\beta 9$ expression. Results from n=7 for PBS, n=7 for PR8, *P<0.05, **P<0.01, ***P<0.001 by one-way ANOVA, mean \pm s.e.m.

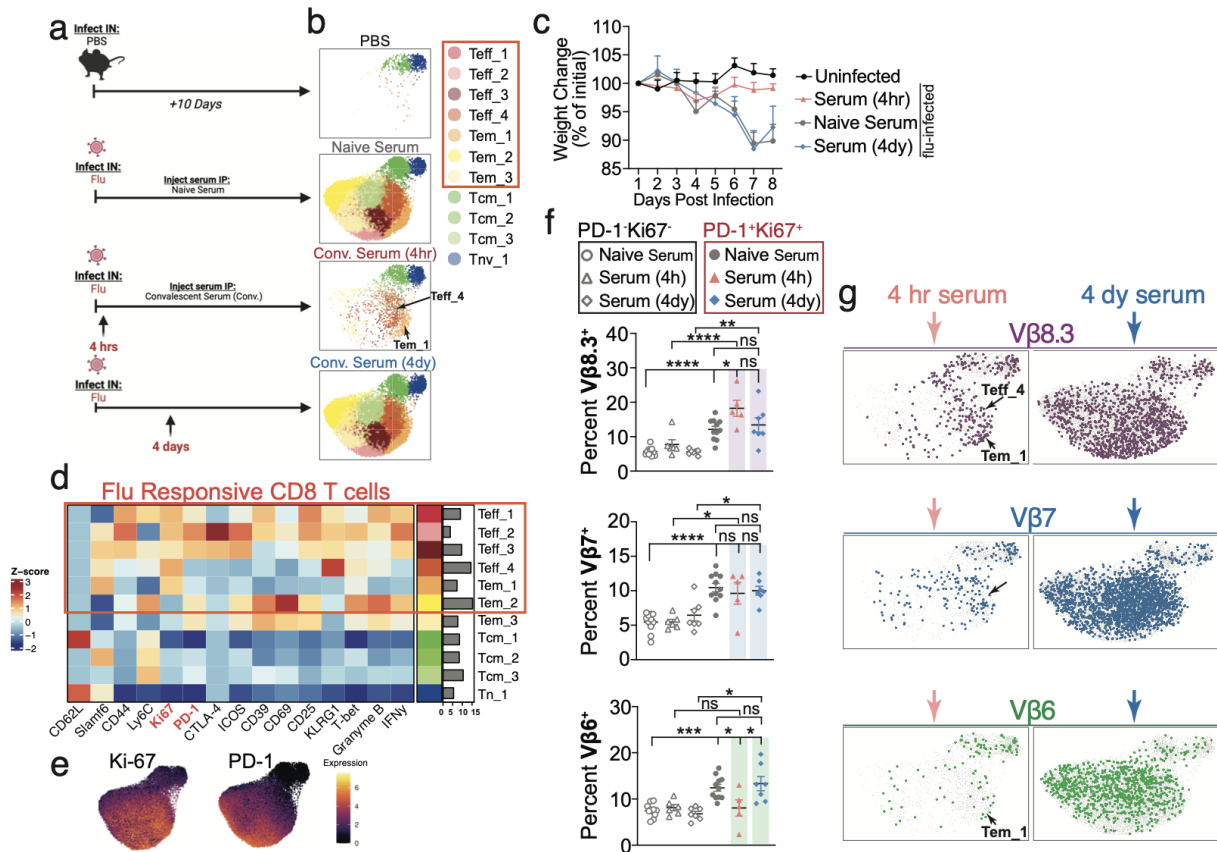


Figure 2.16 | Early convalescent therapy restricts the CD8⁺ T cell repertoire during influenza infection. (a) C57BL/6J mice were infected with influenza IN and then either untreated or treated with convalescent serum at 4 hours or 4 days after infection, and lungs were analyzed at day 10 for the T cell response. (b) UMAP of CD8⁺ T cells based on the expression of non-TCR proteins. (c) Weight change as percentage of initial weight of uninfected and flu-infected mice treated with serum as indicated. (d) Heatmap of non-TCR protein expression annotated by cluster and fraction of cells falling into each cluster. (e) UMAP visualization of CD8⁺ T cells colored by the expression Ki-67 from all cohorts of mice. (f) Comparison of the frequencies of CD8⁺ T cells using Vβ8.3, Vβ7, and Vβ6 in non-proliferating (PD-1⁻Ki-67⁻) and proliferating (PD-1⁺Ki-67⁺) cells in the lungs of flu-infected mice treated with naive or convalescent serum at specified times after infection. (g) UMAP visualization of pooled CD8⁺ T cells from early vs. late convalescent serum treated mice colored by the expression of Vβ8.3, Vβ7, and Vβ6. Results from n=7 for PBS, n=14 for naïve serum-treated infected mice, n=7 for convalescent serum-treated infected mice (*Figure caption continued on the next page.*)

(Figure caption continued from the previous page.) at 4 hours, n=7 for convalescent serum-treated infected mice at 4 days, *P<0.05, **P<0.01, ***P<0.001 by one-way ANOVA, mean \pm s.e.m.

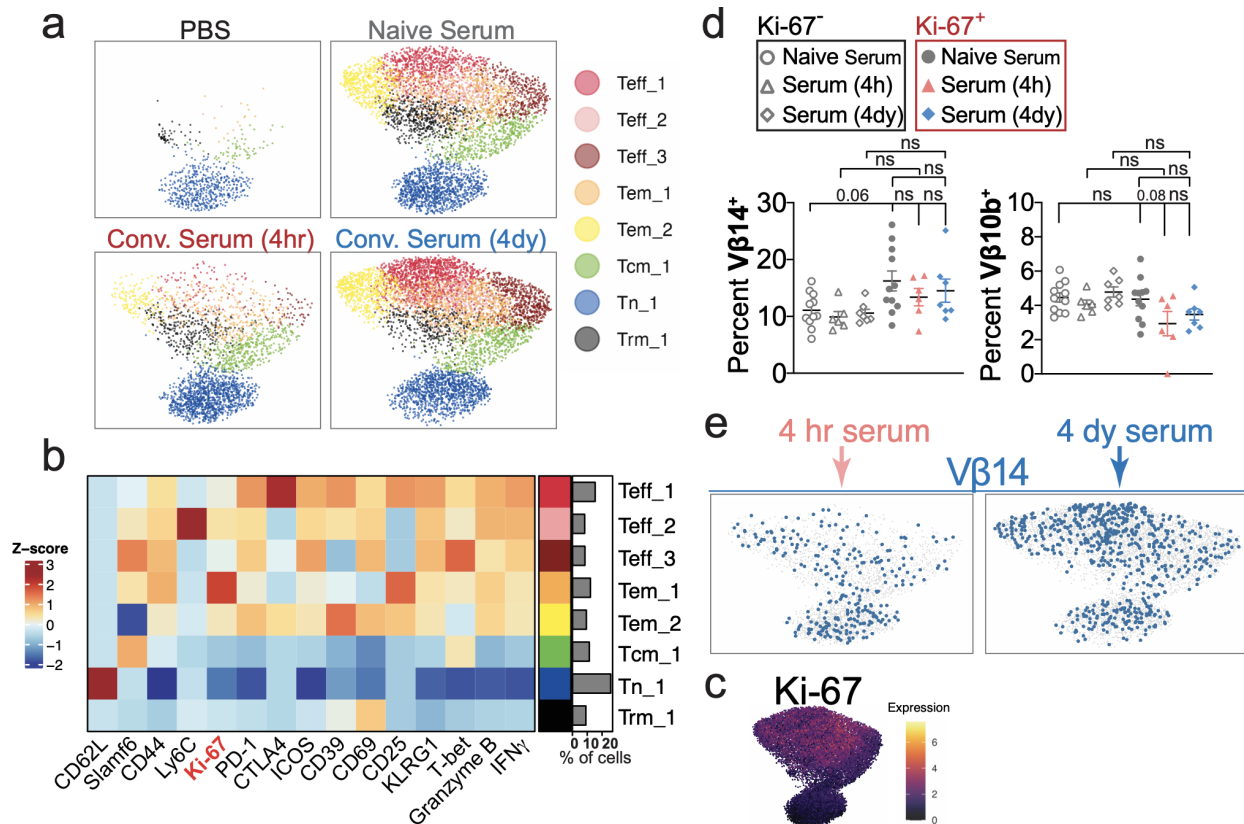


Figure 2.17 | Convalescent therapy has a limited effect on the CD4⁺ T cell repertoire during influenza infection. (a) UMAP visualization of CD4⁺ T conventional (non-Treg) cell clusters based on expression of non-TCR proteins. (b) Heatmap of non-TCR protein expression annotated by cluster and fraction of cells falling into each cluster. (c) UMAP visualization of CD4⁺ T cells colored by the expression Ki-67 from all cohorts of mice. (d) Frequencies of V β 14⁺ and V β 10b⁺ CD4 T cells in non-proliferating (Ki-67⁻) vs. proliferating (Ki-67⁺) cells from the lungs of flu-infected mice treated with naive or convalescent serum at specified times after infection. (e) UMAP visualization of pooled CD4⁺ T cells from early vs. late convalescent serum treated mice colored by V β 14 expression. Results from n=7 for PBS, n=14 for naïve serum-treated infected mice, n=7 for convalescent serum-treated infected mice at 4 hours, n=7 for convalescent serum-treated infected mice at 4 days, *P<0.05, **P<0.01, ***P<0.001 by one-way ANOVA, mean \pm s.e.m.

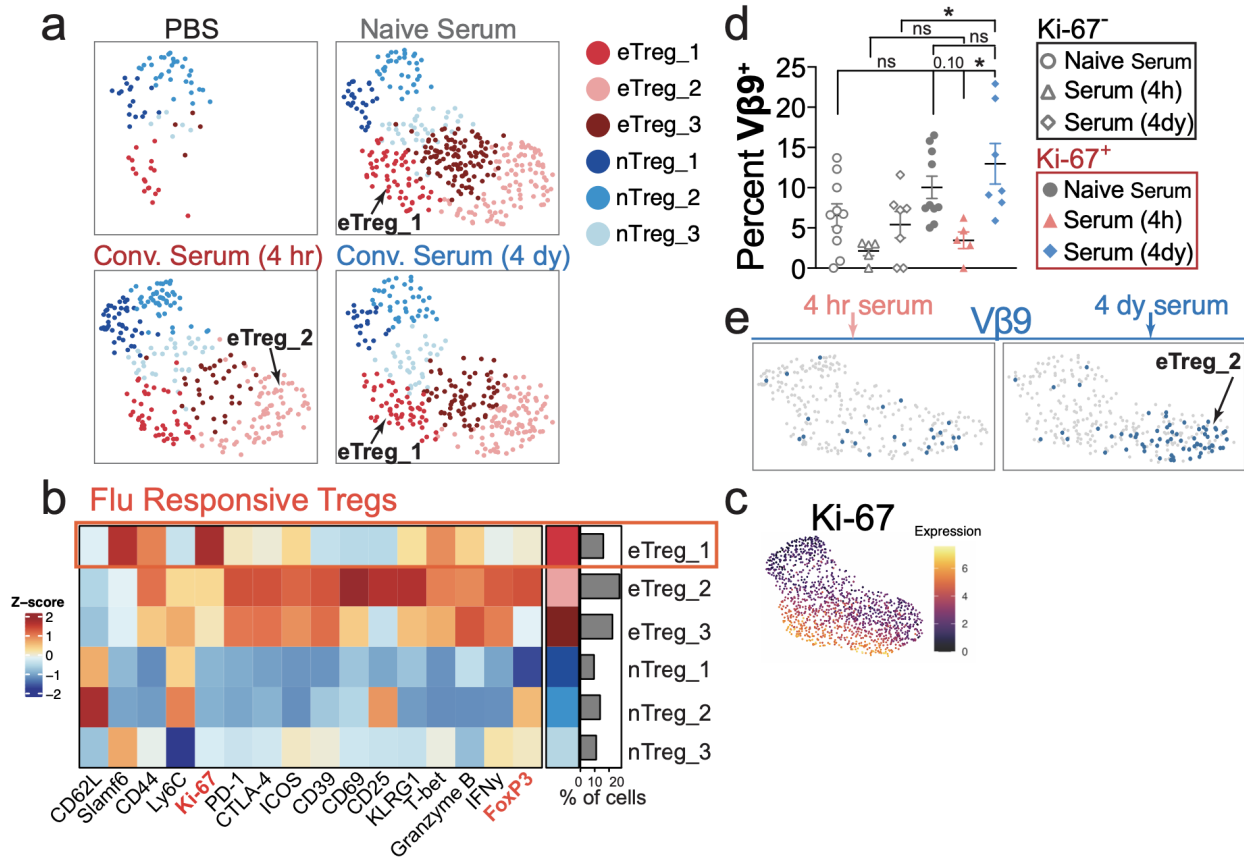


Figure 2.18 | V β 9⁺ Treg clonal population did not expand after early convalescent serum therapy. (a) UMAP of Tregs based on the expression of non-TCR proteins. (b) Heatmap of non-TCR protein expression annotated by cluster and fraction of cells falling into each cluster. (c) UMAP visualization of Tregs colored by the expression Ki-67 from all cohorts of mice. (d) Frequencies of V β 9⁺ Tregs in non-proliferating (Ki-67⁻) vs. proliferating (Ki-67⁺) cells from the lungs of flu-infected mice treated with naive or convalescent serum at specified times after infection. (e) UMAP visualization of pooled Tregs from early vs. late convalescent serum treated mice colored by V β 9 expression. Results from n=7 for PBS, n=14 for naive serum-treated infected mice, n=7 for convalescent serum-treated infected mice at 4 hours, n=7 for convalescent serum-treated infected mice at 4 days, *P<0.05, **P<0.01, ***P<0.001 by one-way ANOVA, mean \pm s.e.m.

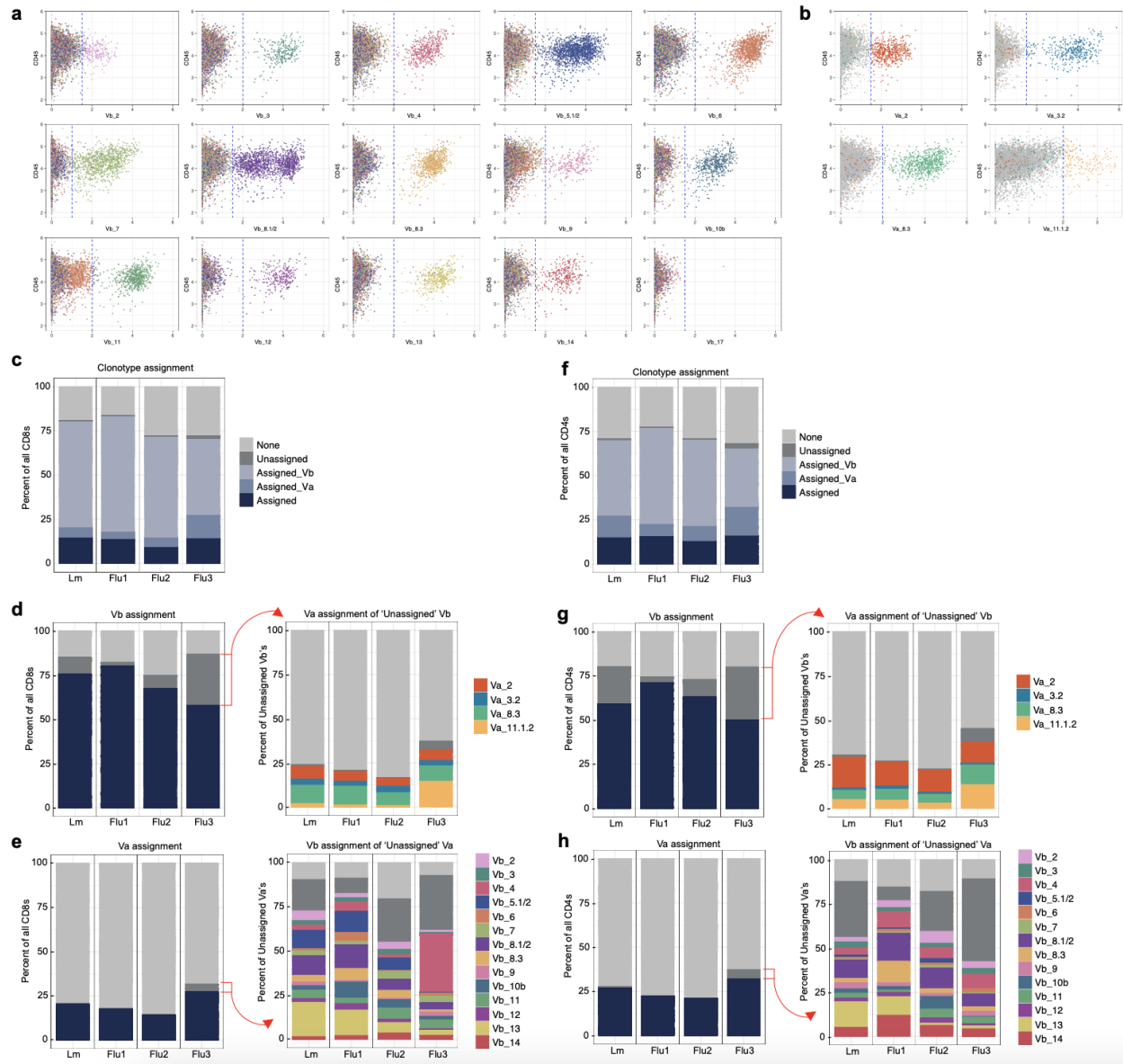


Figure 2.19 | Semi-supervised clonotyping assignment script efficiently streamlines high-dimensional single-cell proteomic analysis. (a) Representative dot plot visualizing T cell classification by variable chain expression by the semi-automated assignment script, colored by V β assignment. Blue line = threshold of positivity for each chain. (b) The same visualization as in (a) but colored by V α assignment. (c) Stacked bar plot of the composition of CD8 T cells from each experiment in this study, colored by clonotype assignment. (d) Left: Stacked bar plot of CD8 T cells from each experiment in this study, colored by V β assignment. Right: Stacked bar plot of CD8 T cells with an 'Unassigned' V β chain, colored by *(Figure caption continued on the next page.)*

V α assignment. (*Figure caption continued from the previous page.*) (e) Left: Stacked bar plot of CD8 T cells from each experiment in this study, colored by V α assignment. Right: Stacked bar plot of CD8 T cells with an ‘Unassigned’ V α chain, colored by V β assignment. (f) Same as (c) for CD4 T cells. (g) Same as (d) for CD4 T cells. (h) Same as (e) for CD4 T cells.

Table 2.1: Antibodies used for mass cytometry of T cell dynamics

Channel	Marker	Vendor	Cat Number	Clone	Species	[Optimal] (ug/mL)	Corresponding figures
89Y	CD45	Biologend	103102	30-F11	Mouse	6	Fig 4, 5, 6
113In	Ter119	Biologend	116202	TER119	Mouse	3	Fig 1, 4, 5, 6
115In	CD45	Biologend	103102	30-F11	Mouse	3	Fig 1
139La	CD44	Biologend	103002	IM7	Mouse	0.75	Fig 4, 5, 6
139La	Ly6G	Biologend	127602	1A8	Mouse	1.5	Fig 1
140Ce	KLRG1	R&D Systems	MAB69441-100	2F1	Mouse	3	Fig 1, 4, 5, 6
141Pr	Granzyme B	Biologend	372202	QA16A02	Mouse	3	Fig 4, 5, 6
141Pr	CD11b	Biologend	101202	M1/70	Mouse	1.5	Fig 1
142Nd	Ly6C	Biologend	128002	HK1.4	Mouse	0.75	Fig 4, 5, 6
142Nd	CD49b	Biologend	103501	HMa2	Mouse	0.1875	Fig 1
143Nd	Vb10b	BD	Custom order	B21.5	Mouse	0.75	Fig 1, 4, 5, 6
144Nd	Va2	BD	Custom order	B20.1	Mouse	0.75	Fig 1, 4, 5, 6
145Nd	CD39	Thermo Scientific	14-0391-82	24DMS1	Mouse	0.75	Fig 4, 5, 6
145Nd	NK1.1	Biologend	108702	PK136	Mouse	3	Fig 1
146Nd	Va11.1/11.2	BD	Custom order	RR8-1	Mouse	6	Fig 1, 4, 5, 6
147Sm	IFNy	Biologend	505834	XMG1.2	Mouse	3	Fig 4, 5, 6
147Sm	PD-L1	Biologend	135202	10F.9G2	Mouse	3	Fig 1
148Nd	Vb14	BD	Custom order	14-2	Mouse	3	Fig 1, 4, 5, 6
149Sm	Vb8.3	BD	Custom order	1B3.3	Mouse	3	Fig 1, 4, 5, 6
150Nd	Vb4	BD	Custom order	KT4	Mouse	3	Fig 1, 4, 5, 6
151Eu	Vb12	BD	Custom order	MR11-1	Mouse	0.75	Fig 1, 4, 5, 6
152Sm	Ki67	Thermo Scientific	12-5698-82	SoIA15	Mouse	6	Fig 1, 4, 5, 6
153Eu	Vb8.1/2	BD	Custom order	MR5-2	Mouse	3	Fig 1, 4, 5, 6
154Sm	Vb5.1/2	BD	Custom order	MR9-4	Mouse	3	Fig 1, 4, 5, 6
155Gd	CD8	Biologend	100702	53-6.7	Mouse	3	Fig 1, 4, 5, 6
156Gd	CD4	Biologend	100506	RM4-5	Mouse	0.75	Fig 1, 4, 5, 6
157Gd	CD3	Biologend	100202	17A2	Mouse	0.75	Fig 1, 4, 5, 6
158Gd	B220	Biologend	103202	RA3-6B2	Mouse	1.5	Fig 1, 4, 5, 6
159Tb	PD-1	Biologend	135202	29.F.1A12	Mouse	0.75	Fig 1, 4, 5, 6
160Gd	Vb3	BD	Custom order	KJ25	Mouse	0.375	Fig 1, 4, 5, 6
161Dy	Tbet	Biologend	644802	4B10	Mouse	6	Fig 1, 4, 5, 6
162Dy	Ly108 (Slamf6)	Thermo Scientific	14-1508-82	13G3-19D	Mouse	1.5	Fig 4, 5, 6
162Dy	TCRgd	Biologend	118101	GL3	Mouse	3	Fig 1
163Dy	Va8.3	BD	Custom order	B21.14	Mouse	3	Fig 1, 4, 5, 6
164Dy	Vb2	BD	Custom order	B20.6	Mouse	3	Fig 1, 4, 5, 6
165Ho	CD69	R&D Systems	AF2386	polyclonal	Mouse	0.75	Fig 1, 4, 5, 6
166Er	Vb17	BD	Custom order	KJ23	Mouse	0.75	Fig 1, 4, 5, 6
167Er	FoxP3	Thermo Scientific	14-4771-80	NRRF-30	Mouse	3	Fig 1, 4, 5, 6
168Er	CD25	Biologend	102040	PC61	Mouse	3	Fig 1, 4, 5, 6
169Tm	CTLA-4	Biologend	106302	UC10-4B9	Mouse	6	Fig 4, 5, 6
169Tm	CD62L-FITC	Biologend	104405 (CD62L-FITC); 408302 (a-FITC)	a-FITC: FIT-22; a-CD62L: MEL14	Mouse	1:100 CD62L-FITC then 6ug/mL a-FITC	Fig 1
170Er	Vb7	BD	Custom order	TR310	Mouse	0.75	Fig 1, 4, 5, 6
171Yb	ICOS	Biologend	313502	C398.4A	Mouse	3	Fig 1, 4, 5, 6
172Yb	Vb9	BD	Custom order	MR10-2	Mouse	0.375	Fig 1, 4, 5, 6
173Yb	Vb6	BD	Custom order	RR4-7	Mouse	1.5	Fig 1, 4, 5, 6
174Yb	Vb11	BD	Custom order	RR3-15	Mouse	0.75	Fig 1, 4, 5, 6
175Lu	Vb13	BD	Custom order	MR12-3	Mouse	0.75	Fig 1, 4, 5, 6
176Yb	Va3.2	BD	Custom order	RR3-16	Mouse	0.75	Fig 1, 4, 5, 6
209Bi	MHCII	Biologend	107602	M5/114.15.2	Mouse	0.1875	Fig 1
209Bi	CD62L	Fisher Scientific	MAB5761SP	95218	Mouse	6	Fig 4, 5, 6

Table 2.2: Markers used for cluster annotations

Conventional T cell cluster family	Cluster defining markers	Variable markers (among clusters of the same family)
Naive	CD62L+ CD44-	Slamf6
Central memory	CD62L+ CD44+	Slamf6, Ki67, ICOS, Ly6C
Effector memory	CD62L- CD44+ KLRG1-	Tbet, CD25, ICOS, Ki67, PD-1, IFN γ , Granzyme B, Ly6C, Slamf6, CD39, CD69, CTLA4
Effectors	CD62L- CD44- KLRG1+ Tbet+	LFA-1, CD25, ICOS, Ki67, PD-1, IFN γ , Granzyme B, Ly6C, Slamf6, CD39, CD69, CTLA4

2.7 Materials and Methods

Animals

C57BL/6J mice were obtained from Jackson laboratories (JAX:000664). For tumor studies, syngeneic C57BL/6J mice were inoculated with 5.0×10^5 MC38, 5.0×10^5 MC38 cells engineered to express ovalbumin (OVA), 5.0×10^5 B16F10 cells, or 5.0×10^5 B16F10 cells engineered to express OVA in PBS subcutaneously. All the experiments were conducted according to the Institutional Animal Care and Use Committee guidelines of the University of California, Berkeley.

Cell lines

MC38, MC38-OVA, B16F10, and B16F10-OVA were kindly provided by Dr. Jeff Bluestone's lab⁵³. All cell lines were maintained in DMEM (GIBCO) supplemented with 10% FBS, sodium pyruvate (GIBCO), 10 mM HEPES (GIBCO), and penicillin-streptomycin (GIBCO). Tumor cells were grown at 37 °C with 5% CO₂.

Intravenous *Listeria* (LADD) infection

All strains of *L. monocytogenes* used in this study were a gift from the Portnoy laboratory at University of California, Berkeley and were derived from the wild-type 10403S strain. The LADD constructs were based on Lm Δ actA/ Δ inIB. LADD-OVA expresses a secreted ActA-OVA fusion as described under the control of the actA promoter⁸³. All strains were cultured in filter-sterilized nutrient-rich Brain Heart Infusion (BHI) media (BD Biosciences) containing 200 μ g/mL streptomycin (Sigma-Aldrich). Overnight cultures were grown in BHI + 200 μ g/mL streptomycin at 30 °C. The following day, bacteria were grown to logarithmic-phase by diluting the overnight in new BHI + 200 μ g/mL streptomycin and culturing at 37°C shaking. Log-phase bacteria were washed and

frozen down in 9% glycerol in PBS. For infections, frozen stocks were diluted in PBS to infect via the tail vein with 1×10^7 CFU log-phase bacteria. The mice were euthanized 5 days post-infection and the spleens were collected for flow analysis.

Intranasal *influenza* infection and intramuscular vaccination

A stock of PR8 H1N1 influenza was a gift from the Arpaia laboratory at Columbia University. Prior to treatment of mice, aliquots were thawed and diluted in sterile PBS such that the desired dose was 54 PFU. Mice were then anesthetized with isoflurane and treated intranasally. For vaccination studies, viral stocks were diluted to inject 540 PFU intramuscularly into the right thigh. Mice were left for a month for viral clearance and generation of memory response before continuing studies.

Convalescent serum treatment

Mice were infected with 54 PFU intranasally and left for a month for viral clearance and generation IgG. Serum was harvested by collecting blood via cardiac puncture and incubating blood at room-temperature to allow coagulation. Samples were centrifuged aliquoted and maintained at 4°C. Quantification of IgG for samples was done by diluting serum samples and using the mouse IgG ELISA commercial kit (Molecular Innovations). For treatment, infected and control mice were given a single dose of 50 µg/mL serum derived from naive or previously infected mice by intraperitoneal (i.p.) injection.

Tissue Collection and preparation for Flow cytometry

Flow cytometry was performed on an BD LSR Fortessa X20 (BD Biosciences) or and datasets were analyzed using FlowJo software (Tree Star). Single cell suspensions were prepared in ice-cold FACS buffer (PBS with 2 mM EDTA and 1% BS) and subjected to red blood cell lysis using ACK buffer (150 mM NH₄Cl, 10 mM KHCO₃, 0.1 mM

Na₂EDTA, pH 7.3). Dead cells were stained with Live/Dead Fixable Blue or Aqua Dead Cell Stain kit (Molecular Probes) in PBS at 4°C. Cell surface antigens were stained at 4°C using a mixture of fluorophore-conjugated antibodies. Surface marker stains for mouse samples were carried out with anti-mouse CD3 (17A2, BioLegend), anti-mouse CD4 (RM4-5, BioLegend), anti-mouse CD8a (53-6.7, BioLegend), anti-mouse CD44 (IM7, BioLegend), anti-mouse CD45 (30-F11, BioLegend), anti-H-2Kb MuLV p15E tetramer-KSPWFTTL (MBL), anti-H-Kb-A2/SIINF EKEL tetramer (NIH tetramer core), anti-IAb/NEKYAQAYPNVS tetramer (NIH tetramer core) in PBS, 0.5% BSA. Cells were fixed using the eBioscience Foxp3/Transcription Factor staining buffer set (eBioscience), prior to intracellular staining. Intracellular staining was performed using anti-mouse Foxp3 (FJK-16S, eBioscience), anti-mouse TNF- α (MP6-XT22, BioLegend), anti-mouse IFN- γ (XMG1.2, eBioscience), at 4°C, according to manufacturer's instructions. Cells were resuspended in PBS and filtered through a 70- μ m nylon mesh before data acquisition. Datasets were analyzed using FlowJo software (Tree Star).

Peptide Restimulation Assays

Resected tumors and lung tissues were minced to 1 mm³ fragments and digested in RPMI-1640 media supplemented with 4-(2-hydroxyethyl)-1-piperazineethanesulfonic acid (HEPES), 20 mg/mL DNase I (Roche), and 125 U/mL collagenase D (Roche) using an orbital shaker at 37°C. Cells from lymphoid organs were prepared by mechanical disruption pressing against a 70- μ m nylon mesh. All the cell suspensions were passed through 40- μ m filters before in vitro stimulation. Cytokine staining was performed with 3-5 x 10⁶ cells in Opti-MEM media supplemented with brefeldin A (eBioscience), 1 μ g/mL peptides, or 10 ng/mL phorbol 12-myristate 13-acetate (PMA) (Sigma), and 0.25 μ M

ionomycin (Sigma). Fixation/permeabilization of cells was conducted for intracellular staining using the eBioscience Foxp3 fixation/permeabilization kit (BioLegend) or Tonbo Foxp3 / Transcription Factor Staining Buffer Kit.

Tissue collection and preparation for mass cytometry

To collect tissues for analysis, at the experimental endpoint mice were euthanized with CO₂ inhalation. Mice were then tracheally perfused with PBS + 5 mM EDTA, and relevant organs were collected. When tumor or lung tissue was collected, these tissues were finely minced and then digested at 37°C in digestion buffer: RPMI-1640 (UCSF Media Production) with 1 mg/mL collagenase IV (Worthington Biochemical) and 0.1 mg/mL DNase I (Sigma-Aldrich). All organs were then processed into a single cell suspension over a 70-µm filter and washed with PBS + 5 mM EDTA. Cells were resuspended 1:1 with PBS + 5mM EDTA and 100 µM cisplatin (Sigma-Aldrich) (diluted in PBS + 5 mM EDTA) for 60 s before quenching with 1:1 with PBS + 0.5% BSA + 5 mM EDTA to determine viability⁴⁰. Cells were again centrifuged and resuspended in PBS + 0.5% BSA + 5 mM EDTA. Samples were aliquoted into individual cluster tubes at ~1-10x10⁶ cells per tube and then fixed at 1.6% PFA (Thermo Fisher Scientific). After quenching the fixation with PBS + 0.5% BSA + 5mM EDTA and washing out the fixative, cells were frozen at -80°C for subsequent CyTOF analysis.

Mass cytometry antibodies

All antibodies used in this study can be found in **Table 2.1**. Antibodies were purchased unlabeled and conjugated to heavy metals in-house. Antibody conjugation to heavy metal tags was done using the MaxPar Antibody Conjugation Kit (Fluidigm) according to the manufacturer's protocol. After labeling, antibodies were diluted to 0.2

mg-0.5 mg/mL in antibody stabilization solution (Candor Bioscience) and stored at 4°C until use. Before using experimentally, conjugated antibodies were titrated on mouse tissue to determine optimal staining concentration (**Table 2.1**). Prior to sample staining, all antibodies were pooled together into either surface or intracellular master mixes and stained together.

Cellular Barcoding

Mass tag cellular barcoding was performed as previously described⁸⁴. Briefly, 1×10^6 cells from a set of 20 samples were stained with a unique 'barcode' that combines 3 Pd isotopes out of 6 total isotopes. This stain was done in 0.02% saponin (Fluidigm's 10x Barcode Perm Buffer diluted in PBS). These 20 samples were then pooled together into 1 tube, washed with PBS + 0.5% BSA + 0.02% NaN₃, and then all $\sim 20 \times 10^6$ cells were stained together for CyTOF. After running these samples by CyTOF, sample data were then deconvoluted according to their Pd isotope barcode as previously described⁸⁴.

Staining for CyTOF

After cellular barcoding, each sample was aspirated to exactly 95 μ L of volume. 5 μ L of TruStain FcX (anti-mouse CD16/32) (BioLegend) was then added and incubated at room temperature for 5 minutes. After Fc block, 400 μ L of the surface staining master mix was added to the samples for a total staining volume of 500 μ L. Sample tubes were then incubated for 30 minutes at room temperature shaking and washed with PBS + 0.5% BSA + 0.02% NaN₃. Each sample was then permeabilized with 100% methanol and incubated at 4°C. Samples were then quenched and washed twice with PBS + 0.5% BSA + 0.02% NaN₃. Intracellular master mix was then added to each sample for a final staining volume of 500 μ L and incubated for 30 minutes at room temperature shaking. Following the

intracellular stain, samples were washed with PBS + 0.5% BSA + 0.02% NaN₃ and resuspended in 1 mL PBS + 2-4% PFA + 1:4000 191/193Ir DNA intercalator (Fluidigm), and left to stain overnight or up to 7 days at 4°C⁸⁵.

CyTOF data collection and normalization

Immediately prior to data acquisition on the instrument, the sample of interest was removed from 4°C, washed with double distilled H₂O, and then washed with Cell Acquisition Solution (CAS) (Fluidigm). For sample running, a bead normalization solution was made by diluting Calibration beads, EQ™ Four Element (Fluidigm), 1:50 by volume in CAS. The sample was then resuspended in 1 mL of this bead solution, counted, and diluted to 1 x 10⁶ cells/mL prior to running on a CyTOF 2 mass cytometer. The entirety of each sample was then collected. After data collection and FCS file creation, samples were normalized as previously described using the internal bead control to account for acquisition fluctuations over time⁸⁵.

Semi-supervised CyTOF clustering and TCR chain analysis

After cellular debarcoding and normalization of samples, individual fcs files were uploaded to Cell Engine. For downstream analysis, T cells were gated according to the following strategy: live (cisplatin⁻, 191/193Ir⁺), CD45⁺, CD3⁺. From there, CD8⁺ T cells were then gated as CD8⁺, conventional CD4⁺ T cells were gated as CD4⁺ FoxP3⁻, and Tregs were gated as CD4⁺ FoxP3⁺. These 3 populations were then exported from Cell Engine as fcs files for each sample for each tissue for each experiment. These fcs files were then imported into R, arcsinh transformed, and compiled into a master data frame for use in the semi-supervised clonotyping assignment script as follows:

First, a matrix is created to store threshold assignments for each $V\alpha$ and $V\beta$ chain. The default threshold set is an arcsinh-transformed value of 1.5 ($\text{arcsinh}(x/5) \geq 1.5$), but this can be changed by the user based on the staining pattern of a particular antibody (**Figure 2.19a, 2.19b**). Then, new columns are created in the master dataframe for each subsequent $V\alpha$ and $V\beta$ assignments to be written in. Upon running the master function, each cell in the data frame will be iterated through and assessed for the expression value of each individual $V\alpha$ and $V\beta$ chain. If there is no $V\alpha$ channel that has a value over the threshold value, the cell's $V\alpha$ column was filled in with 'None.' The same process is implemented for the $V\beta$ channels. If there was more than one $V\alpha$ that has a value over the threshold value, the cell's $V\alpha$ column was filled in with 'Unassigned.' The same process was implemented for the $V\beta$ channels. If the cell had exactly one $V\alpha$ channel that had a value over the threshold value, the cell's $V\alpha$ column were populated with that channel name. The same process was implemented for the $V\beta$ channels. After iterating through each cell in the dataframe, the function creates an additional column called 'Clonotype' and concatenates the $V\alpha$ and $V\beta$ columns into this column (i.e., $V\alpha_2_V\beta_{14}$). Finally, the master data frame was written as a .csv file into the working directory such that clonotype assignment information was maintained for use in downstream analyses.

Rphenograph was used for clustering, and separate experiments, organs, and cell populations (i.e., CD8 cells, CD4 cells, Tregs) were clustered separately. Clustering was done in an unbiased manner using the following parameters: neighbors = 100, mindist = 0.4, k_pheno = 100. An analysis of this computational approach is included in **Figure 2.19**. Figure panels **2-19c** (CD8⁺ T cells) and **2-19f** (CD4⁺ T cells) show the percentage of cells categorized as 'Assigned,' 'Unassigned,' or 'None, by the semi-supervised

script for each experiment. For the 'Unassigned' condition, cells were further categorized by whether the V α , V β , or both chains were 'Unassigned.' This is further demonstrated at the individual chain level, with Figure panels **2.19d** and **2.19g** showing the V β assignment for CD8⁺ and CD4⁺ T cells, and Figure panels **2.19e** and **2.19h** showing the V α assignment for CD8⁺ and CD4⁺ T cells.

Data availability

Additional data available upon request.

Code availability

Automated Clonotyping assignments script is available at Github:

github.com/SpitzerLab/Semi-supervised-Clonotyping-Assignments

Chapter 3: Tumor IL-1 autocrine loop drives systemic chronic inflammation that constrains the ability of peripheral conventional type 1 dendritic cells to prime T cell responses

Rachel DeBarge^{1,2}, Kamir J. Hiam-Galvez^{1,2}, Maya Lopez-Ichikawa^{1,2}, Naa Asheley Ashitey¹, Nam Woo Cho^{1,3}, Matthew H. Spitzer¹

¹ Departments of Otolaryngology and Microbiology & Immunology, Helen Diller Family Comprehensive Cancer Center, Parker Institute for Cancer Immunotherapy, Chan Zuckerberg Biohub, University of California, San Francisco, San Francisco, CA, USA

² Graduate Program in Biomedical Sciences, University of California, San Francisco, San Francisco, CA, USA

³ Department of Radiation Oncology, University of California, San Francisco, San Francisco, CA, USA

Chapter 3 is reprinted as a manuscript in preparation

3.1 Author contributions

Conceptualization, R.D., M.H.S.; Experimental Methodology, R.D., K.J.H.G., M.L.I., N.A.A., N.W.C.; Computational Methodology, R.D.; Investigation, all authors; Writing, R.D.; Funding Acquisition, M.H.S.; Supervision, M.H.S.

3.2 Acknowledgements

We acknowledge the UCSF Parnassus Flow Cytometry CoLab (RRID:SCR_018206) for assisting in generating mass cytometry and flow cytometry data and assisting in cell sorting. We acknowledge the UCSF Functional Genomics Core Facility for assisting in generating RNA sequencing data. Research reported here was supported in part by NIH S10 Instrumentation Grant S10 1S10OD018040-01, DRC Center Grant NIH P30 DK063720, and DoD USAMRAA grant BC220499. R.D. is an NIH F31 Fellow.

3.3 Abstract

Tumors disrupt the homeostasis of the immune system, altering immune cell composition and phenotype in the tumor microenvironment (TME), lymph nodes, spleen, blood, and bone marrow. Mounting a *de novo* immune response both peripherally and intratumorally is required for tumor clearance. Conventional type I dendritic cells (cDC1s) are a critical component of this response and in the success of many immunotherapies. Tumors are known to impair the function of cDCs in the TME, but questions about peripheral cDCs remain. In this study, we use intravenous *Listeria monocytogenes* (*L.m.*) infection as a model of a peripheral Type-I immune response to study how tumors may be affecting secondary lymphoid organs distal to the primary tumor site. Here, we observed that tumor-burdened mice mount a subdued immune response to *L.m.* in the spleen – unless IFN γ is made early in infection, cDCs express less costimulatory molecules, and T cells proliferate less and produce less granzyme B. Upon blockade of IL-1R1 in these tumor-burdened mice, this phenotype is rescued. Investigation of the underlying mechanism revealed that a tumor-initiated IL-1 autocrine loop is the primary driver of peripheral cDC1 dysfunction, and that there is little effect of IL-1 on host cells themselves. Although further studies are necessary to elucidate what effect this autocrine loop has on distal immune cells, here we have advanced the scientific understanding of how chronic inflammation in cancer can drive peripheral immune dysfunction.

3.4 Introduction

Tumors disrupt the homeostasis of the immune system, altering immune cell composition and phenotype in the tumor microenvironment (TME), lymph nodes, spleen, blood, and bone marrow⁸⁶. Mounting a *de novo* immune response both peripherally and intratumorally is required for tumor clearance¹²⁻¹⁴. Conventional type I dendritic cells (cDC1s) are a critical component of this response and in the success of many immunotherapies. cDC1s present antigen, provide co-stimulation, and produce cytokines to prime *de novo* cytotoxic CD8 T cell responses. These CD8⁺ T cells can then go on to clear tumors and intracellular pathogens⁸⁷⁻⁹⁰. Tumors are known to impair the function of cDCs in the TME⁹, but the extent to which immunosuppressive mechanisms of tumors extend to peripheral cDCs distal to the tumor site has remained largely unexplored. Understanding ways in which tumors can exert this immunosuppressive reach will advance our understanding of cDC biology, tumor pathogenesis, and better inform effective immunotherapy development.

Type I immunity protects against intracellular pathogens and is also important in anti-tumor immunity⁹¹. *Listeria monocytogenes* (*L.m.*) is an intracellular bacterium that has long been used as a model pathogen for studying Type I immunity. After intravenous administration in mice, *L.m.* will acutely infect the spleen and liver. After innate recognition of *L.m.*, there will be production of pro-inflammatory cytokines such as IFN γ , TNF α , IL-1B, and IL-18⁹². The initial entry point of this pathogen is through direct infection and endocytosis of *L.m.* by cDC1s^{89,93,94}. Upon infection, cDC1s become activated, upregulating molecules such as CD80 and CD86, which bind to CD28 on T cells for co-stimulation³. Additionally, they produce IL-12, which is important for effector polarization

of T cells. During this activation process, cDC1s will also upregulate antigen processing machinery and present major histocompatibility I (MHCI)-peptide complexes to CD8⁺ T cells⁴. These phenotypic changes are the three signals necessary for a proper *de novo* CD8⁺ T cell response: MHCI-peptide complexes on the surface, costimulatory molecule expression, and cytokine production.

We have shown that in a tumor-burdened mouse, costimulatory molecule expression is lower on splenic cDCs in response to *L.m.*⁸⁶. Additionally, these tumor-burdened mice had reduced CD8⁺ T cell expansion in response to *L.m.*, suggesting a functional defect in splenic cDC1s. Functionality of splenic CD8⁺ T cells from tumor-burdened mice was not impaired in competitive transfer and *ex vivo* experiments, suggesting a T cell -extrinsic defect in priming. Further, these impaired anti-infection responses in tumor-burdened mice were rescued with antigen-presenting cell (APC)-focused treatments such as anti-CD40 agonist but not T cell-directed treatments such as anti-CTLA4, further suggesting a deficit in APC function⁸⁶. Analysis of circulating cytokines in the peripheral blood of tumor-burdened mice revealed elevated levels of G-CSF and IL-1 α . Blockade of these factors in an AT3 tumor-burdened mouse partially restored splenic immune landscapes, but functional tests remained unexplored.

Therefore, we hypothesized that soluble factors in the periphery of tumor-burdened hosts alter the ability of cDC1s to prime *de novo* CD8⁺ T cell responses to secondary infection. In this study, we show upon blockade of IL-1R1 in these tumor-burdened mice, splenic cDC1 activation and T cell proliferation in response to *L.m.* infection is rescued. Investigation of the underlying mechanism revealed that a tumor-initiated IL-1 autocrine loop is the primary driver of peripheral cDC1 dysfunction, and that there is little effect of

IL-1 on host cells themselves. Although further studies are necessary to elucidate the direct effects of this autocrine loop on distal immune cells, here we have advanced the scientific understanding of how chronic inflammation in cancer can drive peripheral immune dysfunction.

3.5 Results

3.5.1 Reduced cDC1 activation in AT3 tumor-bearing mice results in constrained T cell response to *Listeria*

Building off our former study, we first aimed to replicate prior findings and expand the characterization of this model. We began by transplanting AT3 tumors in the mammary fat pad of mice and allowing them to grow to sufficient size. We then performed intravenous infection of *Listeria monocytogenes* expressing whole ovalbumin protein (Lm-OVA) in tumor-bearing mice and healthy controls. We harvested the spleens of mice days 0 through 4 of infection and performed mass cytometry by time of flight (CyTOF) to quantify activation markers on conventional type I dendritic cells (cDC1s). Consistent with prior findings, we saw a peak in activation of cDC1s at 2 days post-infection in control mice, and this activation was diminished in tumor-bearing mice (**Figure 3.1a**). Deconvolution of this activation score at day-2 post-infection, a key T cell priming time point, showed reduced median expression of PDL1, PDCA1, CD70, and CD86 on splenic cDC1s from tumor-burdened mice as compared to controls (**Figure 3.1b**). We then sought to replicate our prior CD8⁺ T cell results. We similarly transplanted AT3 tumors, allowed them to grow to ~100-150 mm², infected with Lm-OVA, and harvested spleens at peak T cell proliferation time point, 7 days post-infection. We again saw that CD8⁺ T cells

from tumor-burdened spleens exhibited reduced granzyme B expression as well as reduced proliferation (**Figure 3.1c**). Further, tumor-burdened CD8⁺ T cells differentiated far less into short-lived effector cells (CD44⁺ CD62L⁻ KLRG1⁺), and a large fraction remained naive (CD44⁻ CD62L⁺) (**Figure 3.1d**).

To establish causation between these two phenotypes, we utilized a reductionist *ex vivo* co-culture system. To do this, we sorted cDC1s from the spleens of tumor-burdened or control mice 2 days post-infection with Lm-OVA and co-cultured them with OT-1 CD8⁺ T cells (**Figure 3.1e**). We quantified proliferation of OT-1 cells 72 hours later by CFSE dye dilution. We were immediately able to see that OT-1 cell cultured with tumor-burdened cDC1s exhibited fewer rounds of division (**Figure 3.1f**). When we quantified this proliferation using a replication index, we indeed saw that tumor-burdened cDC1s drove less T cell proliferation (**Figure 3.1g**). This demonstrated tumor-burdened cDC1s from a Lm-OVA infected spleen day 2 post-infection were sufficient to drive the reduced T cell proliferation we saw at day 7 *in vivo*.

We addressed whether tumor burden intrinsically alters the capacity of splenic cDC1s to perform their functions, or whether this was a primarily *in vivo* phenotype driven by tumor presence. To assess whether tumor-burdened cDC1s were intrinsically capable of antigen uptake, processing, and presentation, we performed a comparative *ex-vivo* co-culture but with the addition of exogenous OVA antigen (**Figure 3.2a**). We saw that addition of this protein rescued the ability of tumor-burdened cDC1s to drive T cell proliferation (**Figure 3.2b**). To assess IL-12 production capabilities, we sorted cDC1s from the spleens of tumor-burdened or healthy control mice, stimulated them *in vitro* with LPS, and then collected culture supernatant the next day (**Figure 3.2c**). We saw no

difference in IL-12 secretion between the conditioned supernatant taken from tumor-burdened and control cDC1s (**Figure 3.2d**). From these experiments we concluded that reduced cDC1 activation in the spleen of tumor-burdened mice in response to *L.m.* infection was driven *in vivo* by tumor presence, and this can be rescued *ex vivo* with perturbation.

3.5.2 Initiation of immune response and cytokine cascade is impaired in AT3 tumor-bearing mice responding to Listeria infection

We investigated why this disruption in splenic cDC1 activation in response to *L.m.* occurred in tumor-burdened mice. The immune response to Listeria infection has been well studied, so we were able to ask whether other components of the infection response upstream of cDC1 activation was disrupted in tumor-burdened mice. We started with a broad comparative characterization of splenic cytokines early in the response to Lm-OVA infection. By performing a fold-change analysis, we observed that there was far less cytokine production in tumor-burdened spleens as compared to control spleens upon Lm-OVA infection (**Figure 3.3a**). Specifically, we determined that key proinflammatory cytokines such as TNF α , IL-6, IL-1B, and IFN γ had a 2-10-fold reduction in tumor-burdened mice. We have previously shown the importance of early bystander NK cell and CD8⁺ T cell activation and IFN γ production for proper cDC1 activation in response to Lm-OVA⁹⁵, so we examined if this cascade was also disrupted. Indeed, NK and CD8⁺ T cell activation as by determined by CD69 expression was significantly reduced at the key cDC1 activation time point, 2 days post-infection (**Figure 3.3b**). Consistent with cytokine results, intracellular cytokine staining of CD8⁺ T cells at day 2 post-infection also showed a reduction in IFN γ production (**Figure 3.3c**).

Up to this point, we had primarily utilized protein measurement of costimulatory molecule expression to characterize cDC1 dysfunction. However, given this broad remodeling of the early immune response to L.m., we examined whether tumor-burdened cDC1s exhibited alterations in basic cellular functioning and cytokine signaling. To this end, we sorted cDC1s from day 2-infected spleens from tumor-burdened and control mice and performed RNA sequencing. Comparing genes differentially expressed in tumor-burdened mice (**Figure 3.3d**, top) to genes differentially expressed in control mice (**Figure 3.3d**, bottom), we observed many differences at the gene ontology level. Specifically, control cDC1s expressed far more gene programs related to pathogen-related immune response and cytokine signaling, particularly interferon signaling. Further, when we compared expression of interferon-stimulated genes (ISGs) between these groups, we saw a substantial reduction in expression in tumor-burdened cDC1s (**Figure 3.3e, 3.3f**). Taken together, these data demonstrated a broad dysregulation of the initiation of the adaptive immune response to Lm-OVA in tumor-burdened mice.

3.5.3 Blockade of IL-1R1 signaling rescues altered immune response to Listeria in AT3 tumor-bearing mice

We determined what was different about tumor-burdened mice that could be driving these changes in the capacity of immune cells to respond to Lm-OVA infection in the spleen. We had previously observed increased circulating G-CSF and IL-1a in the serum of tumor-burdened mice⁸⁶. Consistent with this observation, we also detected these cytokines elevated in the spleens of tumor-burdened mice as compared to control prior to infection (**Figure 3.4a**). Previously, we showed that *in vivo* treatment with an IL-1R1 blocking antibody in tumor-burdened mice reduced both G-CSF and IL-1a circulating

concentrations, as well as remodeling the composition of the spleen. Therefore, we tested how IL-1R1 blockade treatment affected the immune response to Lm-OVA in the spleens of tumor-burdened mice. To do this, we transplanted tumors, allowed them to become established (~20 days of tumor growth), and then split them into two treatment groups. One set of tumor-burdened mice received 200 ug of anti-IL-1R blocking antibody, and the other set of tumor-burdened mice received 200 ug of an isotype-matched control antibody along with a cohort of healthy mice. These mice were treated a total of 3 times every 3 days (days 20, 23, and 26 of tumor growth) leading up to the day of infection (day 28 of tumor growth).

On day 2 post-infection, we found that anti-IL-1R blockade was sufficient to rescue costimulatory molecule upregulation on cDC1s in tumor-burdened mice (**Figure 3.4b**). We repeated this experiment and sorted splenic cDC1s from these mice for analysis by RNA-seq to determine if there were other gene programs altered by anti-IL-1R blockade. To do this, we determined differentially expressed genes between tumor-burdened mice and tumor-burdened mice treated with anti-IL-1R blockade, as well as differentially expressed genes between tumor-burdened mice and control mice. We then plotted these results using a 4-way plot to find concordant gene programs (**Figure 3.4c**). After filtering for significant hits, we found that control mice and anti-IL-1R-treated tumor-burdened mice shared 350 upregulated genes and 58 downregulated genes as compared to tumor-burdened mice alone. Consistent with our protein-level readouts, shared upregulated genes included many costimulatory molecules, but we also found differentially expressed transcripts for chemokines, cytokines, and receptors (**Figure 3.4c**, upper right quadrant), which we also summarized at the gene ontology level (**Figure 3.4d**).

Measurement of spleen supernatant between these groups at day 2 post-infection showed a slight boost in IFN γ secretion in anti-IL-1R-treated mice as compared to tumor-burdened mice alone (**Figure 3.4e**). Despite this seemingly minor boost, we found that many interferon-stimulated genes were back upregulated in tumor-burdened mice treated with anti-IL-1R blockade as compared to tumor-burden alone (**Figure 3.4f**). Lastly, if we examined the CD8⁺ T cell response 7 days post-infection with anti-IL-1R blockade, we also detected a rescue in granzyme B production, proliferation, and effector cell differentiation (**Figure 3.4g**). These data suggested that anti-IL-1R blockade was alleviating chronic IL-1a signaling and inflammation happening in tumor-burdened mice that was affecting the ability of cDC1s in the spleen to respond properly to secondary infection stimulus.

Hypothesizing that cDC1s in the spleen of tumor-burdened mice had access to less to Listeria antigen, we also infected mice with Lm-RFP (red fluorescent protein) and quantified RFP⁺ splenocytes as a measure of pathogen/antigen uptake. Comparison of overall RFP⁺ splenocytes 1-day post-infection showed a minor but insignificant increase in tumor-burdened mice (**Figure 3.5a**). We previously reported that tumor-burdened mice are still able to clear Listeria infection, so this is not unexpected, as the vast majority of RFP⁺ splenocytes were macrophages. However, a deeper characterization showed that RFP⁺ macrophages from tumor-burdened spleens were less activated by determined by MHCII expression as compared to controls (**Figure 3.5b**). Further, we detected slightly less RFP⁺ cDC1s in tumor-burdened spleens as compared to controls (**Figure 3.5c**). As cDC1s are not fully activated until day 2 post-infection, we repeated this experiment at a later time point, and included an anti-IL-1R blockade treatment group. We found that there

was a decrease in RFP+ cDC1s cells in tumor-burdened mice as compared to control, and that anti-IL-1R blockade rescued this decrease to a minor extent (**Figure 3.5d**). Due to the high dose of Lm-RFP treatment required for detectable quantification of RFP+ cDC1s in a small mouse cohort, these results are inconclusive but suggest differential access to antigen in the spleens of tumor-burdened mice. To draw definitive conclusions, these experiments will need to be repeated and validated orthogonally, for example by sorting and lysing cDC1s to quantify bacterial colony formation.

3.5.4 Tumor-initiated IL-1 autocrine loop is a primary driver of peripheral cDC1 dysfunction

We conducted experiments to narrow in on the primary source and target of this circulating IL-1a. Because we had previously shown tumors themselves make IL-1a *in vitro* in addition to it being elevated *in vivo* in tumor-burdened mice, we tested whether knockout of IL-1a in the tumor cells themselves was able to phenocopy the rescue we observed with anti-IL-1R blockade. As we had also identified G-CSF to be elevated in tumor-burdened mice and *in vitro* in tumor supernatants and know this cytokine can be induced by IL-1a, we tested knock out of this cytokine alone and in combination with IL-1a in the tumor cells. To this end, we used CRISPR-cas9 editing to create 4 cell lines: G-CSF knockout, IL-1a knockout, G-CSF and IL-1a double-knockout, and a control-edited tumor line with an irrelevant *Rosa26* gene knocked out. We transplanted all these lines in mice, allowed them to reach sufficient size, and then infected with Lm-OVA alongside healthy controls. At day 2 post-infection, we found that these knock out cell lines were insufficient to rescue CD80⁺CD86⁺ expression on cDC1s, with all lines having significantly reduced expression compared to control Lm-OVA, and no cytokine-knock out line having

any increase compared to the *Rosa26* knock out tumors (**Figure 3.6a**). These results revealed that knockout of IL-1a in the tumor line itself was insufficient to replicate our blockade results, and suggested tumor cells were not the only source of IL-1a and/or there are compensatory signaling from IL-1b that this model did not account for.

Conversely, we also investigated which cells were directly affected by the chronic presence of IL-1a in tumor-burdened mice. We hypothesized that there was a direct effect of IL-1a on immune cells, perhaps including cDC1s themselves. To test this first at a high level, we utilized IL-1R knockout mice. We transplanted tumors into these mice alongside wildtype (WT) mice and then infected with Lm-OVA. Again, we did not see the rescue we had seen with anti-IL-1R blockade, with CD80⁺CD86⁺ expression only marginally different between WT tumor-burdened mice and IL-1R knockout tumor-burdened mice (**Figure 3.6b**). As IL-1 is also an important Type-I cytokine that helps initiate infection response cascades, we confirmed that the cDC1 response to control Lm-OVA infection was not affected by IL-1R knockout (**Figure 3.7a**). As this IL-1R knock out mouse model affected all host cells, these data suggested there was little direct effect of IL-1a on cDC1s or other immune cells. We further demonstrated this utilizing Cre-Lox models we created to delete IL-1R in immune cells of interest. Deletion of IL-1R in all conventional dendritic cells utilizing a CD11c-Cre (**Figure 3.7b**, left) or cDC1s specifically utilizing a XCR1-Cre (**Figure 3.7b**, center) also showed no rescue in CD80⁺CD86⁺ upregulation on day 2 in response to Lm-OVA. We confirmed this *in vitro* using bone marrow-derived dendritic cells (BMDCs). After differentiation, BMDCs were treated with 200 pg/mL IL-1a (circulating serum concentration in tumor-burdened mice) for 5 days, pulsed with whole OVA protein, stimulated with LPS, and then co-cultured with OT-1 CD8⁺ T cells. This

showed there was no significant difference in replication index of OT-1 CD8⁺ T cells cultured with IL-1a-treated BMDCs as compared to untreated controls (**Figure 3.7c**). However, there was a downward trend that warrants follow-up studies such as longer IL-1a treatment and BMDC derivation from IL-1R knockout bone marrow to firmly rule out any direct contribution of IL-1a on cDC1s. Given the broad dysregulation of the early immune response to Lm-OVA we observed in tumor-burdened mice (**Figure 3.2**), we also deleted IL-1R in macrophages, monocytes, and granulocytes utilizing a LysM-Cre (**Figure 3.7b**, right). This mouse model also showed no rescue in CD80⁺CD86⁺ upregulation on day 2 in response to Lm-OVA. Although we need to confirm efficient deletion of the IL-1R gene in the Cre⁺ cells of these 3 mouse models to definitively conclude DCs and other myeloid cells are not directly affected by circulating IL-1a, our whole mouse knockout study is suggestive of minimal direct effects.

These results led us to stain the tumor line for expression of IL-1R1. We found as compared to whole splenocytes, the tumor line itself had extremely high expression of IL-1R (**Figure 3.7d**). To pilot whether knockout of IL-1R in the tumor cells themselves influenced our phenotype, we utilized a strain of this cell line created to have high microsatellite instability (MSI-high) by gene editing with CRISPR-cas9 using either a scrambled guide or IL-1R1 targeting guide. We transplanted these two cell lines into mice and then infected them with Lm-OVA. At day 2 post-infection, we detected a significant rescue of CD80⁺ CD86⁺ expression in the IL-1R1 knockout line as compared to the scrambled control (**Figure 3.6**). Although this cell line had high microsatellite instability as compared to the parental, the peripheral spleen phenotype remained comparable. However, this experiment should be repeated with the microsatellite stable version of the

cell line for confirmation and applicability of these findings. Despite these caveats, this result suggest that blockade with anti-IL-1R antibody was primarily acting on the tumor cells themselves. Because these tumor cells make IL-1a themselves, and there is elevated IL-1b in the TME, we hypothesize that these tumors are creating and driving an autocrine loop that leads to the production of a factor(s) that can migrate to the spleen and affect secondary immune responses.

Lastly, a consistent observation we have made in this tumor model is that it drives increased CD11b⁺ Ly6C⁺ myeloid cells in the spleen, seemingly immature neutrophils and monocytes. This is unsurprising given the increase of IL-1a and G-CSF seen in the serum of these mice, and the role these cytokines have in monocyte and neutrophil recruitment and proliferation. Consistent with this canonical role, we often see a correlative drop in these CD11b⁺ Ly6C⁺ cells in the spleen upon anti-IL-1R blockade (**Figure 3.7e**). As cancer-driven monocytic and granulocytic cells have been previously described to acquire a suppressive phenotype, we wanted to rule out a contributing role of these cells on cDC1 activation, despite most previous studies primarily describing a direct T cell effect. Direct depletion of these cells has been challenging, but data generated in our cell line knockout studies has suggest that the inverse correlation we see with cDC1 activation and CD11b⁺ Ly6C⁺ accumulation seems to not be a significant cause of the phenotype. In our tumor cell line IL-1R knockout study, as we saw significant differences in CD80⁺CD86⁺ expression on cDC1s (**Figure 3.6c**), we assume that if the presence of these CD11b⁺ Ly6C⁺ cells were a primary contributor that there would also be significantly different percentages between the IL-1R knockout and control cell line conditions. However, we instead detected comparable percentages of these cells

between conditions (**Figure 3.7f**). Further, examining the spleen composition absent of infection in mice transplanted with cytokine-knockout tumor cell lines, we detected a substantial decrease in CD11b⁺ Ly6C⁺ cells in the cytokine -knockout lines as compared to Rosa26 control (**Figure 3.7g**). However, these knockout tumors were not sufficient to rescue the cDC1 activation phenotype as measured by CD80⁺CD86⁺ expression (**Figure 3.6a**). Although these experiments were not designed to directly ask the question of whether CD11b⁺ Ly6C⁺ cells contribute to the decrease in cDC1 activation upon *L.m.* infection, these data suggest they are not major contributors. However, more direct tests and comprehensive phenotype characterization of these cells should be performed, such as a reductionist co-culture of tumor-driven CD11b⁺ Ly6C⁺ cells with cDC1s.

3.6 Discussion

The central question of this study focused on whether tumor-induced immunosuppressive mechanisms extend into the periphery to restrict cDC1 function. There are many cancer patients that do not respond to cancer immunotherapeutic intervention. As peripheral antigen-presenting cell function is important for the success of many cancer immunotherapies such as cancer vaccines and checkpoint blockade, this is an important gap in knowledge to address. Here, we show how chronic, systemic inflammation can drive a dysfunctional adaptive immune response to secondary immune stimulus in tumor-bearing mice.

We began by recapitulating prior findings that showed reduced cDC1 costimulatory molecule upregulation in the spleens of AT3 tumor-bearing mice upon secondary *Listeria* infection. This resulted in constrained splenic CD8⁺ T cell response later in infection, and we were able to show reduced cDC1 activation was causal of this phenotype. Notably,

this reduction in T cell priming capacity of cDC1s was driven by *in vivo* tumor presence, and cDC1s were not intrinsically deficient. We went on to demonstrate that beyond the dysfunctional priming ability of cDC1s, the immune response to *Listeria* in the spleens of tumor-burdened mice was broadly dysregulated. There was less early activation of NK cells and CD8⁺ T cells, and a reduced secretion of pro-inflammatory cytokines. Particularly, we detected less IFN γ being secreted at the key DC activation time point of 2 days post-infection, and correspondingly observed reduced interferon-stimulated genes upregulated in tumor-burdened cDC1s.

Mechanisms of suppression by tumors have generally focused locally on the tumor microenvironment, or proximally in draining lymph nodes. Tumors can interfere with proper cDC differentiation, disrupt activation signals, create metabolic stress, inhibit antigen processing and presentation, affect cellular viability, and more⁹⁻¹¹. Whereas acute exposures to pro-inflammatory cytokines are generally thought to promote immune cell activation and recruitment in canonical responses such as infection and wound healing⁹⁶, chronic exposure and signaling has long been described to be pro-tumorigenic⁹⁷⁻⁹⁹. This can happen through direct tumor cell adaptation to this chronic inflammation, but it can also create feedback loops that can be suppressive towards immune cells attempting an anti-tumor response¹⁰⁰. These mechanisms have been described for cytokines such as TNF α , IL-6, and IL-1, and the inherent heterogeneity of tumors results in pleiotropic effects of these cytokines based on tumor model and duration of exposure.

In our tumor model, we observed elevated IL-1a levels in the serum and spleen of mice. Upon treatment with an IL-1R blocking antibody in tumor-burdened mice, the dysfunctional splenic immune responses to *L.m.* were rescued. After ruling out a direct

effect of IL-1a on cDC1s and host cells more broadly, we were able to show that the primary target of this anti-IL-1R blockade was the tumor cells themselves. Although AT3 tumors appear to be an important source of IL-1a in these mice, knock out of this cytokine in tumor cells alone was not sufficient to replicate anti-IL-1R blockade results. This may be due to additional IL-1a production from host cells, or compensatory increase in IL-1 β upon its knockout. Although IL-1a and not IL-1 β was elevated in the serum of tumor-burdened mice, we do see production of IL-1 β in the tumor microenvironment. As AT3 tumor cells seem to be the primary cell signaling through IL-1R, follow up studies should be performed to determine if contribution from both IL-1a and IL-1 β in the tumor microenvironment drives peripheral immunosuppression. Notably, blockade of IL-1 signaling with an IL-1R antagonist, Anakinra, is a clinically approved therapeutic^{101,102}. This warrants deeper interrogation of available clinical datasets utilizing Anakinra to identify any concordant or divergent immunological effects as compared to our study to rationally design immunotherapeutic combinatorial approaches.

This study is not without caveats, and further studies need to be done to determine the actual cause of peripheral immune cell dysfunction in this tumor model, as it seems the effect of IL-1a is primarily indirect. Comparing splenic supernatants from infected mice transplanted with AT3-IL-1R knockout tumors to parental AT3 tumors may help identify candidate factors. These factors could then be cross-compared with cytokine, chemokine, or other candidate pathways that may be dysregulated at the gene expression level in cDC1s. Overall, fully understanding the effect of the chronic inflammation present in this tumor model, and its downstream effects on peripheral immune cell response to

secondary stimulus, will advance our understanding of cDC biology, tumor pathogenesis, and ways in which immunotherapies can be improved.

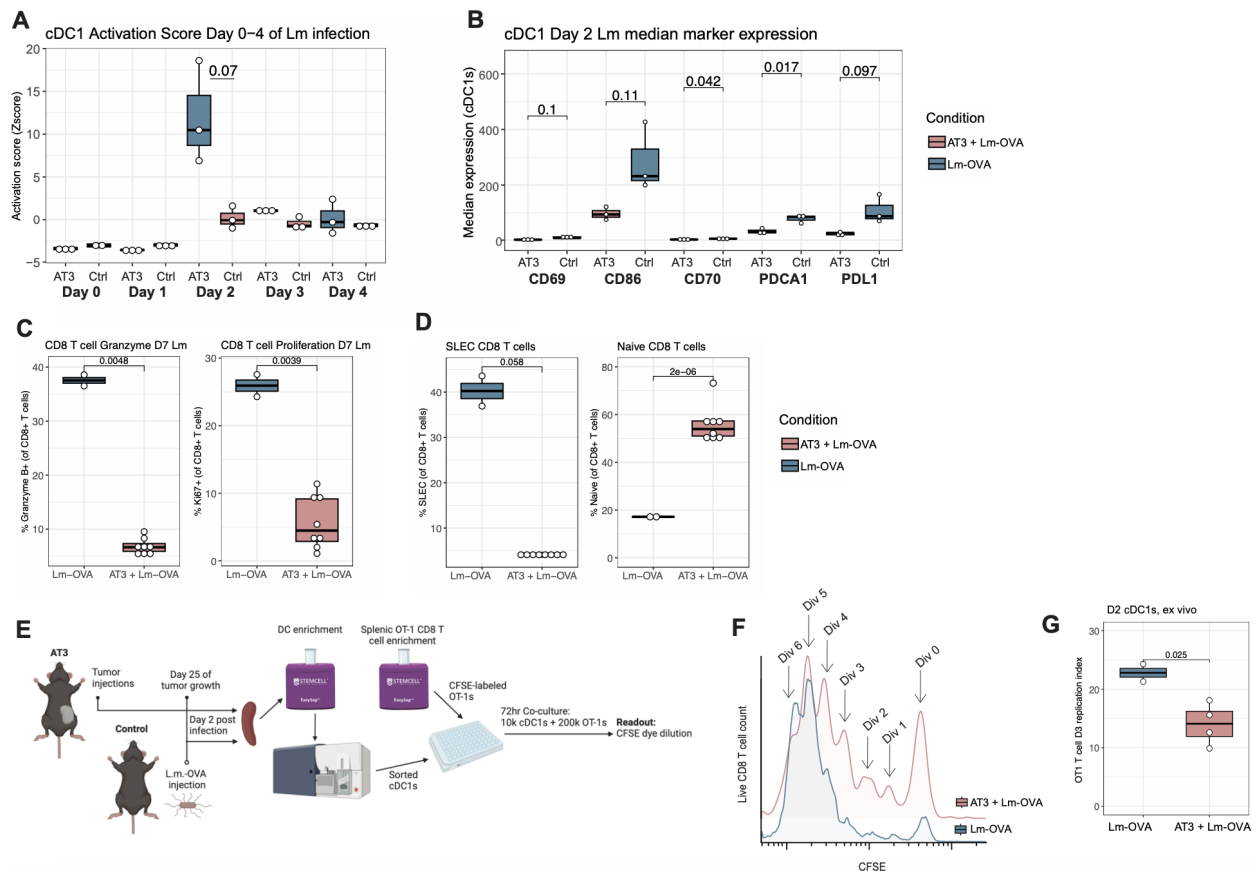


Figure 3.1 | Reduced cDC1 activation in AT3 tumor-bearing mice results in constrained T cell response to Listeria. (a) Comparison of scaled ‘activation score’ of cDC1s in control mice and tumor-bearing mice days 0-4 after Lm-OVA infection. (b) Raw median expression of ‘activation score’ markers of cDC1s in control mice and tumor-bearing mice Lm day 2 after Lm-OVA infection. (c) Frequency of granzyme B (left) and Ki67 (right) expressing CD8⁺ T cells in the spleens of control mice and tumor-bearing mice day 7 after Lm-OVA infection. (d) Frequency of short-lived effector CD8⁺ T cells (left) and naive CD8⁺ T cells (right) in the spleens of control mice and tumor-bearing mice day 7 after Lm-OVA infection. (e) Schematic of *ex vivo* cDC1 and OT-1 CD8⁺ T cell co-culture set-up. (f) Overlay of raw CFSE dye dilution histogram of OT-1 CD8⁺ T cells from one biological replicate from each condition. (g) Quantification of CFSE dye dilution by replication index of OT-1 CD8⁺ T cells cultured with control cDC1s or tumor-burdened cDC1s.

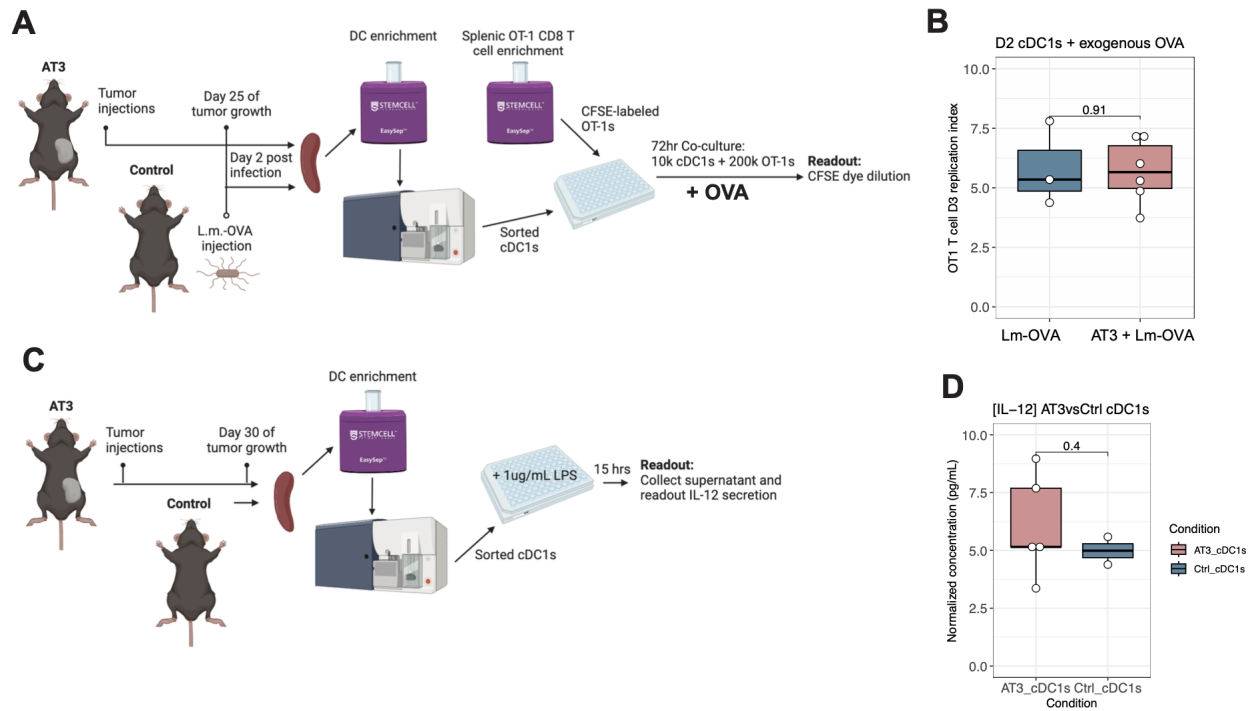


Figure 3.2 | Reduced splenic cDC1 function driven by *in vivo* tumor presence. (a) Schematic of *ex vivo* cDC1 and OT-1 CD8⁺ T cell co-culture with OVA protein experimental design. (b) Quantification of CFSE dye dilution by replication index of OT-1 CD8⁺ T cells cultured with control cDC1s or tumor-burdened cDC1s. (c) Schematic of *ex vivo* cDC1 stimulation for IL-12 secretion measurement. (d) Cell input-normalized IL-12p70 concentration in conditioned media of cDC1s from control and tumor-burdened mice.

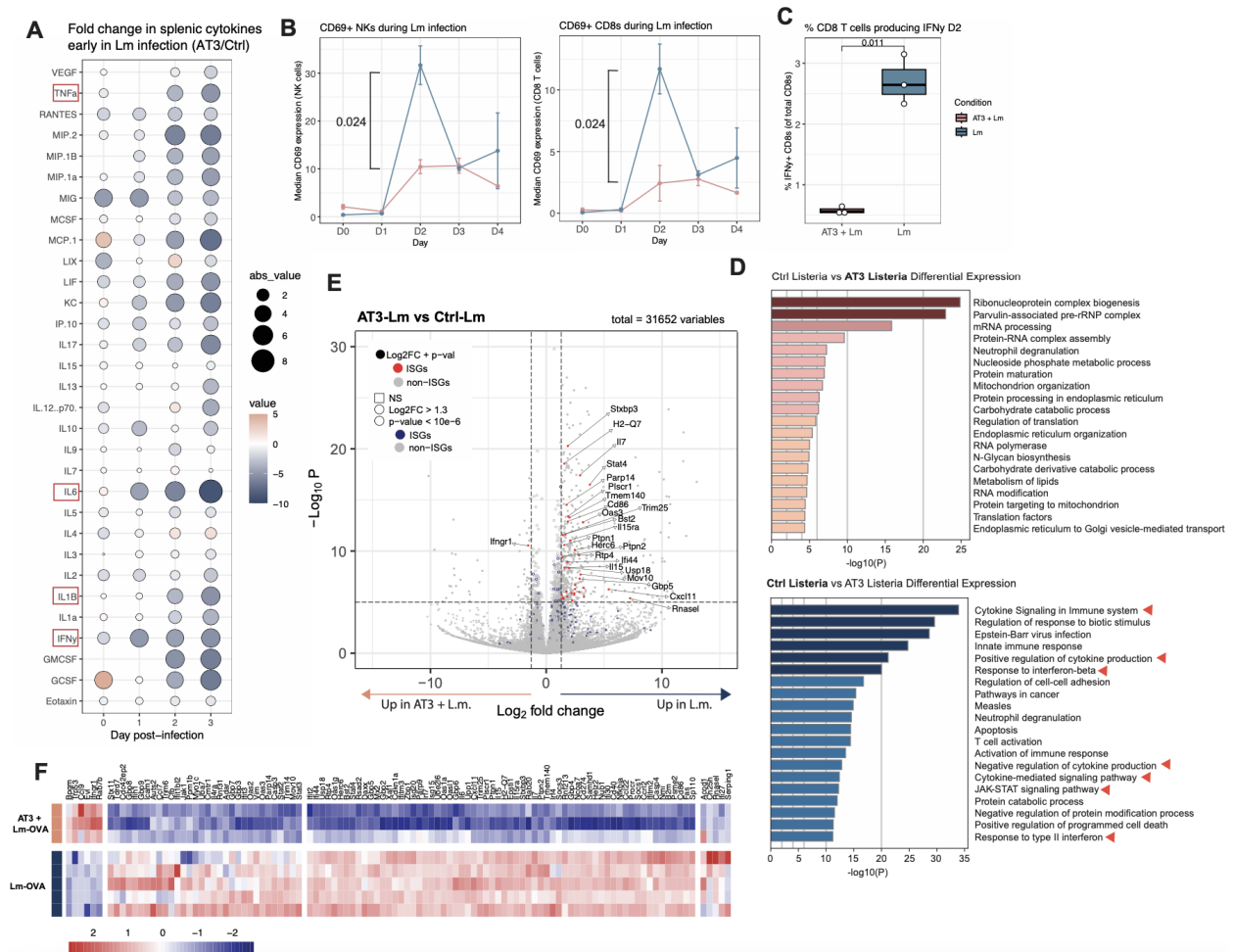


Figure 3.3 | Initiation of immune response and cytokine cascade is impaired in AT3 tumor-bearing mice responding to Listeria infection. (a) Fold change quantification of cytokines from tumor-burdened spleens over control spleens days 0-3 after Lm-OVA infection (n=3 mice per group per day). (b) Median CD69 expression of NK cells (left) and CD8⁺ T cells (right) from tumor-burdened spleens and control spleens days 0-4 after Lm-OVA infection. (c) Frequency of IFN γ + CD8⁺ T cells from tumor-burdened spleens and control spleens day 2 after Lm-OVA infection. (d) Top 20 pathways identified by gene ontology analysis of genes differentially expressed by splenic cDC1s day 2 after Lm-OVA infection from tumor-burdened mice (top) or control mice (bottom). (e) Volcano plot comparing genes expressed by control and tumor-burdened cDC1s day 2 after Lm-OVA infection, colored and annotated by whether genes are or are not interferon-stimulated genes. (f) Scaled heatmap of all interferon-stimulated genes differentially (*Figure caption continued on the next page.*)

(Figure caption continued from the previous page.) expressed between control and tumor-burdened cDC1s day 2 after Lm-OVA infection.

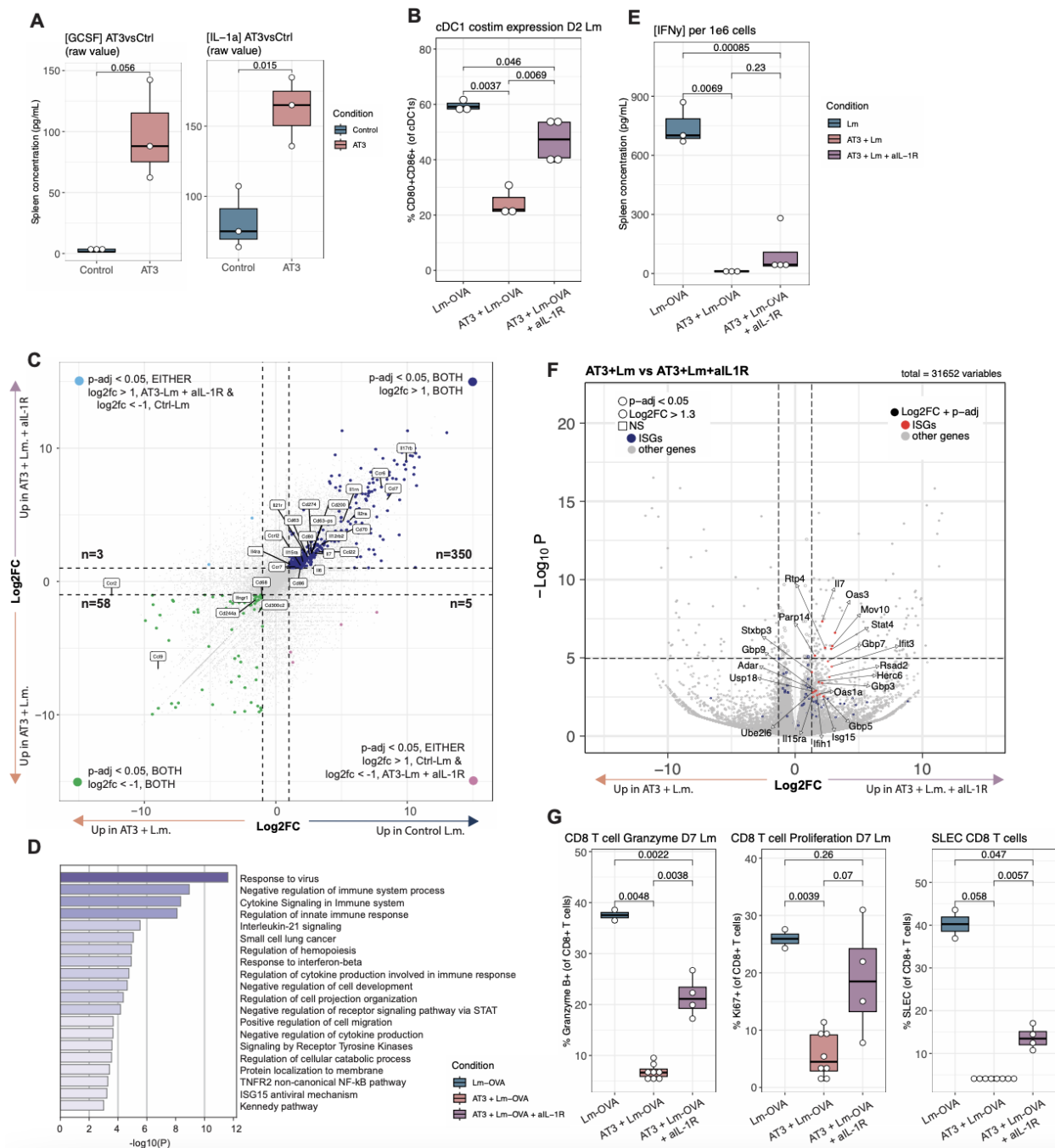


Figure 3.4 | Blockade of IL-1R1 signaling rescues altered immune response to Listeria in AT3 tumor-bearing mice. (a) Raw concentration of G-CSF and IL-1a in the spleens of tumor-burdened and control spleens. (b) Frequency of CD80⁺CD86⁺ splenic cDC1s day 2 after Lm-OVA infection from control, tumor-burdened, and anti-IL-1R treated tumor-burdened mice. (c) 4-way plot comparing fold change of genes differentially expressed by cDC1s day 2 (*Figure caption continued on the next page.*)

(Figure caption continued from the previous page.) after Lm-OVA infection in control vs tumor-burdened mice (x-axis) and anti-IL-1R treated tumor-burdened mice vs tumor-burdened mice (y-axis). (d) Top 20 pathways identified by gene ontology analysis of genes differentially expressed by splenic cDC1s day 2 after Lm-OVA by both control mice and anti-IL-1R treated tumor-burdened mice as compared to tumor-burdened mice. (e) Normalized concentration of IFN γ after Lm-OVA infection in the spleens of control, tumor-burdened, and anti-IL-1R treated tumor-burdened mice. (f) Volcano plot comparing genes expressed by anti-IL-1R treated tumor-burdened and tumor-burdened cDC1s day 2 after Lm-OVA infection, colored and annotated by whether genes are or are not interferon stimulated genes. (g) Frequency of granzyme B-expressing (left), Ki67-expressing (middle), short-lived effector (right) CD8⁺ T cells in the spleens of control mice and tumor-bearing mice day 7 after Lm-OVA infection.

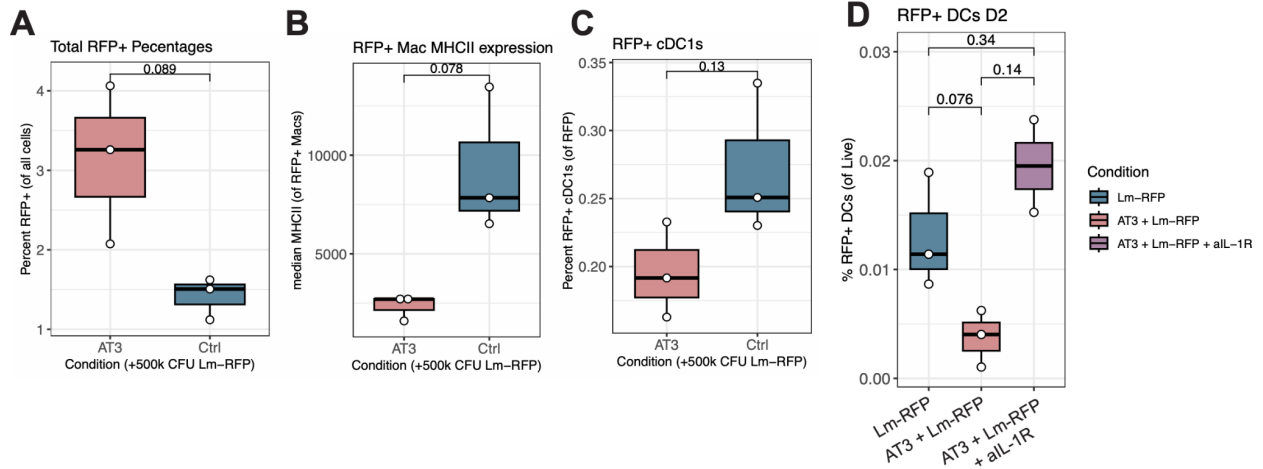


Figure 3.5 | Immune cell uptake of Lm-RFP affected by tumor burden. (a) Frequency RFP+ splenocytes in tumor-burdened and control mice day 1 after high-dose Lm-RFP infection. (b) Median expression of MHCII on RFP+ macrophages day 1 after high-dose Lm-RFP infection. (c) Frequency RFP+ cDC1s in tumor-burdened and control mice day 1 after high-dose Lm-RFP infection. (d) Frequency RFP+ DCs in control, tumor-burdened, and antiIL-1R treated tumor-burdened mice day 2 after high-dose Lm-RFP infection.

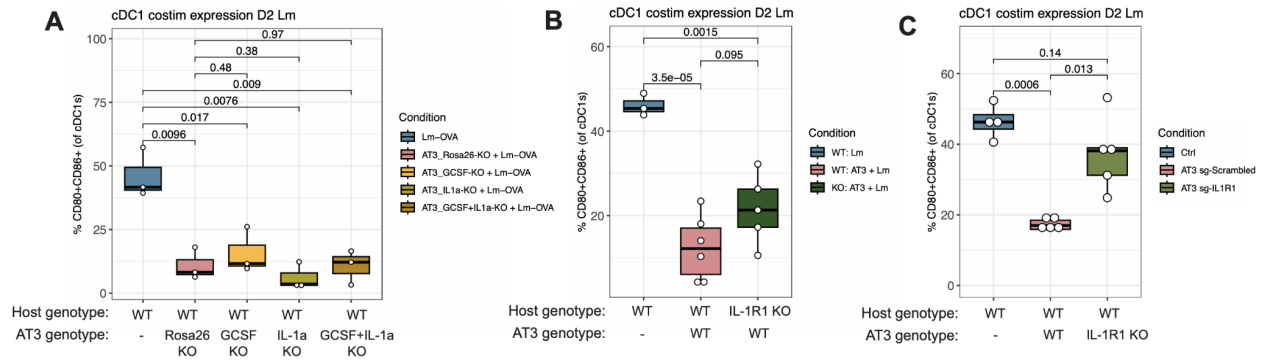


Figure 3.6 | Tumor-initiated IL-1 autocrine loop primary driver of peripheral cDC1 dysfunction. (a) Frequency of CD80⁺CD86⁺ splenic cDC1s day 2 after Lm-OVA infection in control mice and mice transplanted with parental or cytokine knockout tumors. (b) Frequency of CD80⁺CD86⁺ splenic cDC1s day 2 after Lm-OVA infection in WT control, WT tumor-burdened, and IL-1R knockout tumor-burdened mice. (c) Frequency of CD80⁺CD86⁺ splenic cDC1s day 2 after Lm-OVA infection in control mice and mice transplanted with parental or IL-1R knockout tumors.

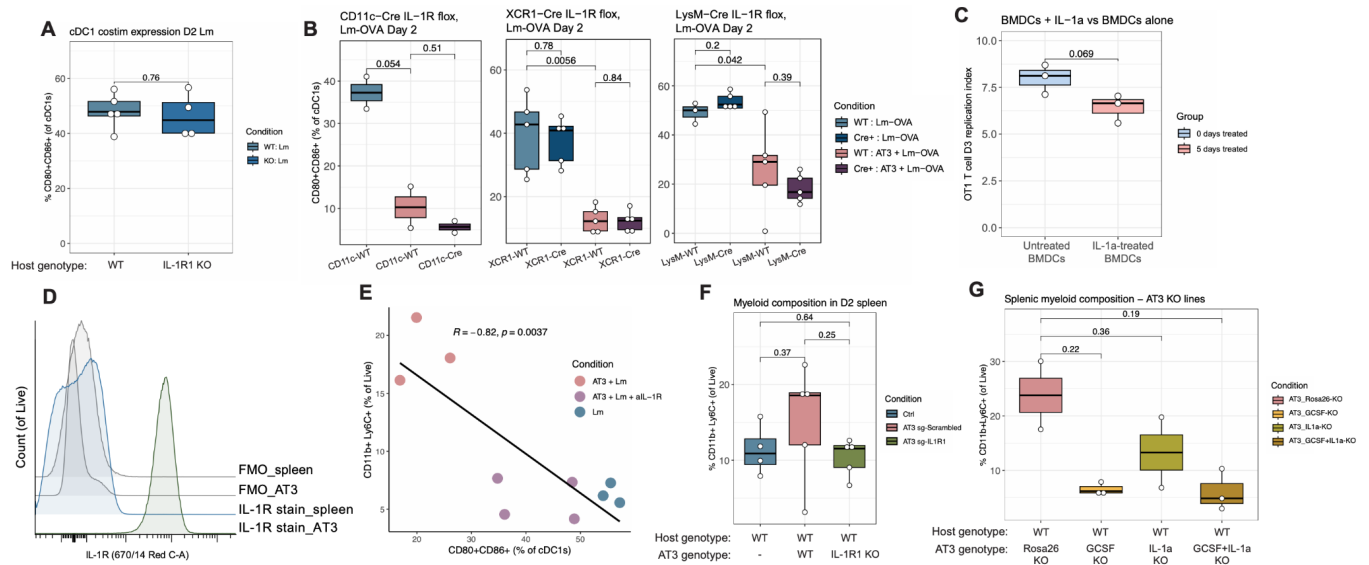


Figure 3.7 | Direct effects of IL-1R signaling constrained to tumor cells. (a) Frequency of CD80⁺CD86⁺ splenic cDC1s day 2 after Lm-OVA infection in WT and IL-1R knockout mice. (b) Frequency of CD80⁺CD86⁺ splenic cDC1s day 2 after Lm-OVA infection in tumor-burdened mice as compared to control in WT mice as compared to a CD11c-Cre IL-1R-flox background (left), XCR1-Cre IL-1R-flox background (center), or LysM-Cre IL-1R-flox background (right) mice. (c) Quantification of CFSE dye dilution by replication index of OT-1 CD8⁺ T cells cultured with control BMDCs or BMDCs treated with IL-1a for 5 days. (d) Histogram plot of IL-1R staining on AT3 tumor cells and splenocytes, as well as respective fluorescence minus one (FMO) controls. (e) Dot plot of CD80⁺CD86⁺ cDC1s (x-axis) versus CD11b⁺Ly6C⁺ splenocytes (y-axis) within the same samples, quantified with Pearson correlation trendline. (f) Frequency of CD11b⁺Ly6C⁺ cells day 2 after Lm-OVA infection in the spleens of control mice and mice transplanted with parental or IL-1R knockout tumors. (g) Frequency of CD11b⁺Ly6C⁺ cells in the spleens of mice transplanted with parental or cytokine knockout tumors.

Table 3.1: CRISPR-Cas9 cell line editing information.

Cell line	gRNA target	crRNA sequence	Indel %	KO %
Parental (Rosa26 KO)	Thumpd3 (Rosa26)	TTACCAGTTCAAAGATACGA	-	-
GCSF KO	Csf3 (GCSF)	AAATACCCGATAGAGCCTGC	87	79
	Csf3 (GCSF)	GGGGTGACACAGCTTGTAGG		
IL-1a KO	IL-1a	TTACCTGATTCAGAGAGAGA	87	76
	IL-1a	TCCATAACCCATGATCTGGA		
GCSF + IL-1a KO	Csf3 (GCSF)	AAATACCCGATAGAGCCTGC	79	71
	Csf3 (GCSF)	GGGGTGACACAGCTTGTAGG		
	IL-1a	ATGTATGCCTACTCGTCGGG	71	66
	IL-1a	TTACCTGATTCAGAGAGAGA		
MSI-high IL-1R KO	IL-1R	AGCATACAATTGTAGCCGTG	sorted based on IL-1R-staining	
	IL-1R	CAGCAAGACCCCATATCAG		
	MSH2	GGTTAATACCCTGATACAGT	-	-
	MSH2	CACATGAGCGAAGCTAACAA		

Table 3.2: CyTOF antibodies used for time course studies.

Label	Marker	[optimal staining] (ug/mL)	Vendor	Catalog Number	Clone
113In	Ter119	3	Biologend	116202	TER119
115In	CD45	3	Biologend	103102	30-F11
139La	Ly6G	1.5	Biologend	127602	1A8
140Ce	KLRG1	3	R&D Systems	MAB69441-100	2F1
141Pr	LFA1	3	Biologend	141002	H155-78
142Nd	CD49b	0.75	Biologend	103501	HMa2
143Nd	CD11c	0.75	DVS Sciences	3142003B	N418
144Nd	CD49d	3	Biologend	103701	R1-2
145Nd	CD27	0.75	Biologend	302802	LG.3A10
146Nd	CD138	3	Biologend	142502	281-2
147Sm	PD-L1	3	Biologend	135202	10F.9G2
148Nd	CD103	3	Biologend	121402	2E7
149Sm	SiglecF	1.5	BD	552125	E50-2440
150Nd	PDCA-1	0.75	Biologend	127002	120G8.04
151Eu	Ly6c	0.75	Biologend	128002	HK1.4
152Sm	Ki67	6	Thermo Scientific	12-5698-82	SoIA15
153Eu	CD11b	3	Biologend	101202	M1/70
154Sm	SIRPa	3	Biologend	144002	P84
155Gd	CD8	3	Biologend	100702	53-6.7
156Gd	CD4	0.75	Biologend	100506	RM4-5
157Gd	CD3	0.75	Biologend	100202	17A2
158Gd	B220	1.5	Biologend	103202	RA3-6B2
159Tb	PD-1	3	Biologend	135202	29.F.1A12
160Gd	NK1.1	1.5	Biologend	108702	PK136
161Dy	Tbet	6	Biologend	644802	4B10
162Dy	TCRgd	3	Biologend	118101	GL3
163Dy	CD62L	0.75	Fisher Scientific	MAB5761SP	95218
164Dy	CD86	6	Biologend	105002	GL-1
165Ho	CD69	0.75	R&D Systems	AF2386	polyclonal
166Er	CD70	3	Thermo Scientific	14-0701-82	FR70
167Er	FoxP3	3	Thermo Scientific	14-4771-80	NRRF-30
168Er	CD25	3	Biologend	102040	PC61
169Tm	a-CD45-FITC	6	Biologend	103108 (CD45-FITC); 408302 (a-FITC)	a-FITC: FIT-22; a-CD45: 30-F11
170Er	CD115	1.5	Biologend	135502	AFS98
171Yb	CD64	6	Biologend	139302	X54-5/7.1
172Yb	CD68	3	Biologend	137002	FA-11
173Yb	CD19	0.75	Biologend	115547	6D5
174Yb	GrzmB	3	Biologend	372202	QA16A02
175Lu	CD44	0.375	Biologend	103002	IM7
176Yb	CD54	3	Biologend	116102	YN1/1.7.4
209Bi	MHC II	0.1875	Biologend	107602	M5/114.15.2

Table 3.3: Antibodies used for flow cytometry and cell sorting.

Channel(s)	Marker	Clone	Catalog number(s)	Vendor
BV421	CD11b	M1/70	101236	Biolegend
PE			117308	
APC	CD11c	N418	117310	Biolegend
BV510			117353	
BV711	CD127	A7R34	135035	Biolegend
APC-Cy7	CD19	6D5	115529	Biolegend
PE-Cy7			115519	
BV605			100237	
APC-Cy7	CD3	17A2	100222	Biolegend
PE-Cy7			100220	
BV421	CD4	GK1.5	100437	Biolegend
PerCPCy5.5	CD44	IM7	103032	Biolegend
PE-Cy7			103029	
FITC	CD45	30-F11	103108	Biolegend
PE	CD62L	MEL-14	553151	BD Biosciences
BV421			104436	Biolegend
BV605	CD64	X54-5/7.1	139323	Biolegend
PE-Cy7	CD70	FR70	104612	Biolegend
BV650			100741	
FITC	CD8a	53-6.7	100708	Biolegend
PerCPCy5.5			100734	
BV650	CD80	16-10A1	104732	Biolegend
FITC	CD86	GL-1	105005	Biolegend
APC-Cy7	F4/80	BM8	123117	Biolegend
PE-Cy7			25-4801-82	Thermo Fisher
PE-Dazzle 594	Granzyme B	QA16A02	372216	Biolegend
PE	IFN γ	XMG1.2	505808	Biolegend
APC	IL-1R	JAMA-147	113505	Biolegend
APC	Ki67	SolA15	17-5698-80	Thermo Fisher
PE-Cy7			138416	
PerCPCy5.5	KLRG1	2F1/KLRG1	138418	Biolegend
BV711			138427	
APC			128016	
BV785	Ly6C	HK1.4	128041	Biolegend
BV605			128035	
APC			107614	
BV785	MHCII	M5/114.15.2	107645	Biolegend
PE-Cy7			107630	
BV650			107641	
APC	PD-1	29F.1A12	135210	Biolegend
PE	PDL1	10F.9G2	124307	Biolegend

3.7 Materials and methods

Animals

All mice were housed in an American Association for the Accreditation of Laboratory Animal Care–accredited animal facility and maintained in specific pathogen-free conditions. Animal experiments were approved and conducted in accordance with AN200691-00C. Wild-type female C57BL/6 mice between 7-10 weeks old were purchased from The Jackson Laboratory and housed at our facility. OT-1 mice were kindly provided by Lewis Lanier (UCSF). IL-1R knockout mice were kindly provided by Arun Prakash (UCSF). Animals were housed under standard SPF conditions with typical light/dark cycles and standard chow.

In vivo treatments

For studies testing pharmacological blockade of IL-1R1, mice were treated with 200 ug of anti-mouse IL-1R (CD121a) (clone JAMA-147, Bioxcell, cat #BE0256) or an isotype-matched control antibodies (polyclonal Armenian hamster IgG, Bioxcell, cat #BP0091). This was done every 3 days for a total of 3 doses prior to infection with *Listeria*.

Cell lines

AT3 cells were gifted by Dr. Ross Levine (Memorial Sloan Kettering Cancer Center). Cells were cultured in DMEM supplemented with 10% fetal calf serum, 1% penicillin and streptomycin, and 1% HEPES. For *in vivo* studies, AT3 (5×10^5 cells per 100 μ l) cells were transplanted into the fourth mammary fat pad. OP9-DL1 cells were gifted by Art Weiss (UCSF). Cells were cultured in MEM-alpha supplemented with 20% fetal calf serum and 1% penicillin-streptomycin.

Generation of cell line knockouts

AT3 cell line knockout of genes was performed using an electroporation-based CRISPR-Cas9 system. All crRNA sequences are listed in **Table 3.1**. First, tracrRNA and crRNA were incubated together at a molar ratio of 1:1 for 30 minutes at 37° C. For conditions targeting multiple DNA sequences, crRNAs were added at a lower fraction for a final molar ratio of 1:1 with tracrRNA. After creating the sgRNA(s) for each condition, cas9 protein was then added for a final molar ratio of 4 sgRNA: 1 cas9 and incubated for 15 minutes at 37° C to form RNP. AT3 cells were resuspended in SE electroporation buffer (Lonza, cat # V4XC-1032) and added to a Lonza electroporation plate. Immediately before electroporation, RNP was added to each respective well. AT3 cells were then electroporated with the Lonza 4D 96-well electroporation system using code DSS-120. Immediately following electroporation, pre-warmed media was added to each well for recovery before plating in cell culture vessels for expansion.

Cytokine knockout lines were validated at a polyclonal level with Sanger sequencing. Multiple gRNA combinations were tested, and the cell lines with the best indel percentage and knockout score were chosen for *in vivo* testing (**Table 3.1**). Knockout of the IL-1R in the MSI-high AT3 line was confirmed by staining cells for IL-1R and sorting on negative cells by flow cytometry for downstream culture. MSH2 knockout was not relevant for this study, but gRNAs used were also included in **Table 3.1**.

Intravenous *Listeria* infection

Listeria monocytogenes strain 10403s expressing OVA (Lm-OVA) was kindly provided by Shomyseh Sanjabi (UCSF). *Listeria monocytogenes* strain expressing RFP was kindly provided by Michel DuPage (UC Berkeley). Lm-OVA stocks frozen at -80° C

were grown overnight at 37° C in BHI broth supplemented with antibiotics (5 ug/ml erythromycin for Lm-OVA and 5 ug/ml streptomycin for Lm-RFP). Then, overnight cultures were subcultured by diluting into fresh BHI broth supplemented with antibiotics and grown for 3 hours. Bacteria CFU was then quantified by measuring optical density at 600 nm. Bacteria were then diluted to 5×10^4 CFU in 100 μ l sterile PBS and 100 μ l was injected per mouse i.v. via the retro-orbital vein.

Tissue collection and preparation for cytometry

All tissue preparations were performed simultaneously from each individual mouse, as previously reported¹³. After euthanasia by CO₂ inhalation, spleens were collected and homogenized in PBS + 5 mM EDTA at 4° C. All tissues were washed with PBS + 5 mM EDTA and re-suspended 1:1 with PBS with EDTA and 100 mM cisplatin (Enzo Life Sciences, Farmingdale, NY) for 60 s before quenching 1:1 with PBS + 5 mM EDTA + 0.5% BSA to determine viability as previously described. Cells were centrifuged at 500 x g for 5 min at 4° C and re-suspended in PBS/EDTA/BSA at a density between $1-10 \times 10^6$ cells/ml. Care was taken to maintain all samples at 4° C during all phases of tissue harvest and preparation except viability staining and fixation. Suspensions were then divided and either stained and run fresh for analysis by flow cytometry or fixed for 10 min at RT using 2% PFA in PBS (Fisher Scientific) and frozen at -80° C for CyTOF or other flow cytometry analysis.

Cell sorting and flow cytometry

Cells were stained for viability with Zombie-NIR fixable dye (BioLegend, cat #423105). Cell surface staining was performed in cell staining media (PBS with 0.5% BSA and 0.02% NaN₃) for 20 minutes at 4° C. For intracellular staining, cells were fixed in 2%

PFA in PBS following the surface stain. Cells were then permeabilized with 0.1% Triton-X for 10 minutes at RT. After washing, cells were stained intracellularly in cell staining media (PBS with 0.5% BSA and 0.02% NaN₃) for 30 minutes at room temperature. Stained cells were analyzed with an LSR II flow cytometer (BD Biosciences). Cell sorting was performed on a FACSAria II (BD Biosciences). Antibodies used for staining are listed in **Table 3.2**.

Sample prep for RNAseq

Cells were prepared with a surface stain as described for flow cytometry and then sorted into lysis buffer (1X Takara single-cell lysis buffer) containing an RNase inhibitor (Takara, cat #2313B) using a FACSAria II (BD Biosciences). After collection, tubes were vortexed for 30 s and flash frozen on dry ice and stored at -80° C. Library preparation was performed by the UCSF CoLabs Genomics Core by converting mRNA for each biological replicate into cDNA and amplified using the Takara SMART-Seq v4 Ultra low Input RNA kit (Takara Bio). Library quality control was performed by the Genomics Core prior to sequencing. Sequencing was then performed by the Chan-Zuckerberg Biohub on a NovaSeq (Illumina).

Splenic cell co-cultures

For coculture of cDC1s and OT-1 CD8⁺ T cells, cDC1s from spleens of interest were first enriched using EasySep Mouse Pan-DC Enrichment Kit (StemCell Technologies). Samples were then prepared as described for flow cytometry. F480-CD11c⁺MHCII⁺CD8⁺CD11b⁻ cDC1s were then sorted and cocultured with immunomagnetically enriched OT1 CD8⁺ T cells. Prior to addition to culture, OT1 CD8⁺ T cells were labeled with CFSE dye (BioLegend, cat #423801) at 5 uM for 30 minutes at

37° C. Cells were cultured in RPMI-1640 (UCSF Media Core Facility) supplemented with 10% FBS (Omega Scientific), 100 U/mL penicillin-streptomycin (UCSF Media Core Facility), 2 mM L-glutamine (Sigma-Aldrich), and 50 μ M β -mecaptoethanol (Thermo Fisher Scientific). For cultures testing direct *ex vivo* functionality of cDC1s from Lm-OVA infected spleens, no exogenous antigen was added so as to not skew T cell fate or priming capacity. For cultures testing the inherent capacity of cDC1s from tumor-burdened spleens to endocytose, process, and present antigen, whole ovalbumin protein (OVA) (Invivogen, cat #vac-pova) was added into cultures at 0.5 mg/mL. Calculation of replication index for comparison of cocultures between groups was performed as previously described using quantification of CFSE dye dilution¹⁰³. Briefly, this calculation incorporates the percent of the total cells that have divided at least once, the percent of total cells actively dividing, and the overall fold expansion of the culture.

Bone-marrow derived dendritic cell (BMDC) differentiation

BMDCs were generated as previously described to differentiate primarily cDC1-like cells¹⁰⁴. Briefly, bone marrow was harvested from the femurs of mice and made into a single-cell suspension. This suspension was then filtered over a 70- μ m filter and plated at 0.5×10^6 cells per well in a 24-well plate in 2mLs DC media (DMEM + 10% FBS + 1% L-glutamine + 1% sodium pyruvate + 1% MEM non-essential amino acids + 1% penicillin and streptomycin + 50 μ M beta-mercaptoethanol) supplemented with 100 ng/mL FLT3L (Peprotech). After 3 days, bone marrow cells were plated with fresh FLT3L media on a monolayer of OP9-DL1 cells previously treated with mitomycin-c for 2 hours. After another 3 days, OP9-DL1 cells were refreshed, and BMDCs were considered fully differentiated and ready to use in downstream assays.

Mass cytometry, antibodies

All antibodies used in this study are listed in **Table 3.2**. Antibodies were purchased unlabeled and conjugated to heavy metals. Antibody conjugation to heavy metal tags was done using the MaxPar Antibody Conjugation Kit (Fluidigm) according to the manufacturer's protocol. After labeling, antibodies were diluted to 0.2-0.5 mg/mL in antibody stabilization solution (Candor Bioscience) and stored at 4° C until use. Before using experimentally, conjugated antibodies were titrated to determine optimal staining concentration (**Table 3.2**). Prior to sample staining, all antibodies were pooled together into either surface or intracellular master mixes and stained together.

Cellular Barcoding

Mass tag cellular barcoding was performed as previously described⁸⁴. Briefly, 1×10^6 cells from a set of 20 samples were stained with a unique 'barcode' that combines 3 Pd isotopes out of 6 total isotopes. This stain was done in 0.02% saponin (Fluidigm's 10x Barcode Perm Buffer diluted in PBS). These 20 samples were then pooled together into 1 tube, washed with PBS + 0.5% BSA + 0.02% NaN₃, and then all $\sim 20 \times 10^6$ cells were stained together for CyTOF. After running these samples by CyTOF, sample data were then deconvoluted according to their Pd isotope barcode as previously described.

Staining for CyTOF

After cellular barcoding, each sample was aspirated to exactly 95 μ L of volume. Five μ L of TruStain FcX (anti-mouse CD16/32) (BioLegend) was then added and incubated at room temperature for 5 minutes. After Fc block, 400 μ L of the surface staining master mix was added to the samples for a total staining volume of 500 μ L. Sample tubes were then incubated for 30 minutes at room temperature shaking and

washed with PBS + 0.5% BSA + 0.02% NaN₃. Each sample was then permeabilized with 100% methanol and incubated at 4°C. Samples were then quenched and washed twice with PBS + 0.5% BSA + 0.02% NaN₃. Intracellular master mix was then added to each sample for a final staining volume of 500 µL and incubated for 30 minutes at room temperature shaking. Following the intracellular stain, samples were washed with PBS + 0.5% BSA + 0.02% NaN₃ and resuspended in 1 mL PBS + 2-4% PFA + 1:4000 191/193I DNA intercalator (Fluidigm), and left to stain overnight or up to 7 days at 4° C⁸⁵.

CyTOF data collection and normalization

Immediately prior to data acquisition on the instrument, the sample of interest was removed from 4° C, washed with double distilled H₂O, and then washed with Cell Acquisition Solution (CAS) (Fluidigm). For sample running, a bead normalization solution was made by diluting Calibration beads, EQ™ Four Element (Fluidigm), 1:50 by volume in CAS. The sample was then resuspended in 1 mL of this bead solution, counted, and diluted to 1 x 10⁶ cells/mL prior to running on a CyTOF 2 mass cytometer. The entirety of each sample was then collected. After data collection and FCS file creation, samples were normalized as previously described using the internal bead control to account for acquisition fluctuations over time⁸⁵.

Cytokine quantification

For *in vivo* measurement of splenic cytokines, mouse spleens were processed in a minimal 500 uL volume of sterile PBS. Then, samples were centrifuged at 1,000 x g for 10 minutes and the supernatant was removed for analysis. Samples were sent to Eve Technologies and analyzed using a multiplex cytokine array.

RNAseq analysis

Sequencing reads were demultiplexed and adapter reads were trimmed by the Chan-Zuckerberg sequencing core. Quality of raw FastQ files was performed using FastQC. Alignment of paired reads of each sample was then performed using the STAR aligner¹⁰⁵. Gene counts for each sample were then summarized using featureCounts¹⁰⁶. These raw counts were then filtered for quality and count, and then normalized using DESeq2. Differential expression analysis was then performed using DESeq2¹⁰⁷. Gene ontology analysis was performed using Metascape¹⁰⁸. All other analyses were performed in R using Complex Heat Map, Enhanced Volcano, and ggplot2. Interferon stimulated gene lists were compiled using the Molecular Signatures Database (MSigDB)^{109–111}.

Statistics

Statistical tests of protein expression and cytokine secretion data were performed using unpaired two-sided student's t-test.

Chapter 4: Closing and Future Directions

Development of a high-throughput proteomic approach to study clonal T cell dynamics at the same time as phenotypic characterization has revealed many interesting observations that warrant follow up study. For one, questions emerged about the inherent capacity of T cells utilizing certain V β chains to protect against certain immune challenges. Studies should be performed to determine the contribution of primary tissue infection site versus infectious strain or model antigen used in the challenge to drive expansion of particular V β ⁺ T cells. It's of particular interest to investigate why certain clonal populations are favored to differentiate toward a tissue-resident memory-like state. Findings involving convalescent serum transfer also warrant more detailed follow-up studies to determine the specific timing required for protective effect, as well as whether Tregs contribute to this protection. Given the differences we observed in TCR V β use in CD8⁺ T cells as compared to conventional and regulatory CD4 T cells, it would also be interesting to deplete certain T cell populations using V β antibodies and study the resulting pathological effect and clonal dynamics. Overall, the application of this CyTOF panel to various contexts such as Type 2 immune challenges and infections of different tissues can be extremely powerful for understanding concordant and divergent regulators of T cell expansion and differentiation.

Study into ways tumors can exert broad-reaching immunosuppressive signals to disrupt T cell priming has created many additional questions. Primarily, follow-up studies are needed to determine what soluble factor, or factors, are secreted as a result of autocrine IL-1 signaling in tumor cells. Given the broad remodeling of the immune response to secondary infection we documented in the spleens of tumor-burdened mice,

this chronic inflammation affects many immune cells. However, the effects may be direct or indirect depending on the factor. It is also of interest to use high-dimensional imaging such as MIBI to understand the spatial component of the immune response to Listeria. Migration and colocalization of cDC1s and T cells is vital for priming, so understanding if there is a spatial component to the impaired infection response is important. Further, this study raises the question of whether other mediators of chronic inflammation that have been described to be immunosuppressive, such as high circulating IL-6 concentrations, suppress the immune response in similar or diverging ways to IL-1.

Overall, these studies advance our understanding of T cell priming and differentiation dynamics by investigating signals upstream of cDC1 activation as well as T cell TCR use and differentiation across disease. We created a useful tool to study T cell dynamics, and deeply characterized a model of peripheral immune dysfunction. These studies advanced our understanding of how diverse T cell dynamics can be across subtypes, disease, and treatment modalities. These studies also revealed a mechanism by which tumors can systematically disrupt immune responses through mediation of chronic inflammation. Follow-up of these studies utilizing orthogonal technologies and other models will continue to build our understanding of the requirements for effective adaptive immunity.

References

1. Mellman, I. Dendritic cells: master regulators of the immune response. *Cancer Immunol Res* **1**, 145–149 (2013).
2. Merad, M., Sathe, P., Helft, J., Miller, J. & Mortha, A. The dendritic cell lineage: ontogeny and function of dendritic cells and their subsets in the steady state and the inflamed setting. *Annu. Rev. Immunol.* **31**, 563–604 (2013).
3. Balan, S., Saxena, M. & Bhardwaj, N. Dendritic cell subsets and locations. *Int. Rev. Cell Mol. Biol.* **348**, 1–68 (2019).
4. Reis e Sousa, C. Dendritic cells in a mature age. *Nat. Rev. Immunol.* **6**, 476–483 (2006).
5. Kaech, S. M. & Cui, W. Transcriptional control of effector and memory CD8⁺ T cell differentiation. *Nat. Rev. Immunol.* **12**, 749–761 (2012).
6. Reina-Campos, M., Scharping, N. E. & Goldrath, A. W. CD8 T cell metabolism in infection and cancer. *Nat. Rev. Immunol.* **21**, 718–738 (2021).
7. Beuneu, H. *et al.* Visualizing the functional diversification of CD8⁺ T cell responses in lymph nodes. *Immunity* **33**, 412–423 (2010).
8. Kakaradov, B. *et al.* Early transcriptional and epigenetic regulation of CD8 T cell differentiation revealed by single-cell RNA sequencing. *Nat. Immunol.* **18**, 422–432 (2017).
9. Wculek, S. K. *et al.* Dendritic cells in cancer immunology and immunotherapy. *Nat. Rev. Immunol.* **20**, 7–24 (2020).
10. Garner, H. & de Visser, K. E. Immune crosstalk in cancer progression and metastatic spread: a complex conversation. *Nat. Rev. Immunol.* **20**, 483–497

- (2020).
11. DeVito, N. C., Plebanek, M. P., Theivanthiran, B. & Hanks, B. A. Role of Tumor-Mediated Dendritic Cell Tolerization in Immune Evasion. *Front. Immunol.* **10**, 2876 (2019).
 12. Spitzer, M. H. *et al.* Systemic Immunity Is Required for Effective Cancer Immunotherapy. *Cell* **168**, 487–502.e15 (2017).
 13. Yost, K. E. *et al.* Clonal replacement of tumor-specific T cells following PD-1 blockade. *Nat. Med.* **25**, 1251–1259 (2019).
 14. Kagamu, H. *et al.* CD4 T-cell Immunity in the Peripheral Blood Correlates with Response to Anti-PD-1 Therapy. *Cancer Immunol Res* **8**, 334–344 (2020).
 15. Sheikh, N. *et al.* Clonotypic Diversification of Intratumoral T Cells Following Sipuleucel-T Treatment in Prostate Cancer Subjects. *Cancer Res.* **76**, 3711–3718 (2016).
 16. De Simone, M., Rossetti, G. & Pagani, M. Single Cell T Cell Receptor Sequencing: Techniques and Future Challenges. *Front. Immunol.* **9**, 384005 (2018).
 17. T-cell repertoire analysis and metrics of diversity and clonality. *Curr. Opin. Biotechnol.* **65**, 284–295 (2020).
 18. Jiang, N., Schonnesen, A. A. & Ma, K.-Y. Ushering in Integrated T Cell Repertoire Profiling in Cancer. *Trends Cancer Res.* **5**, 85–94 (2019).
 19. Carter, J. A. *et al.* Single T Cell Sequencing Demonstrates the Functional Role of $\alpha\beta$ TCR Pairing in Cell Lineage and Antigen Specificity. *Front. Immunol.* **10**, 464451 (2019).
 20. Fehlings, M. *et al.* Checkpoint blockade immunotherapy reshapes the high-

- dimensional phenotypic heterogeneity of murine intratumoural neoantigen-specific CD8⁺ T cells. *Nat. Commun.* **8**, 1–12 (2017).
21. Hombrink, P. *et al.* High-Throughput Identification of Potential Minor Histocompatibility Antigens by MHC Tetramer-Based Screening: Feasibility and Limitations. *PLoS One* **6**, e22523 (2011).
 22. Abdelbary, M., Hobbs, S. J., Gibbs, J. S., Yewdell, J. W. & Nolz, J. C. T cell receptor signaling strength establishes the chemotactic properties of effector CD8⁺ T cells that control tissue-residency. *Nat. Commun.* **14**, 1–14 (2023).
 23. Huppa, J. B., Gleimer, M., Sumen, C. & Davis, M. M. Continuous T cell receptor signaling required for synapse maintenance and full effector potential. *Nat. Immunol.* **4**, 749–755 (2003).
 24. The role of T cell receptor signaling thresholds in guiding T cell fate decisions. *Curr. Opin. Immunol.* **33**, 43–48 (2015).
 25. Moon, J. J. *et al.* Naive CD4(+) T cell frequency varies for different epitopes and predicts repertoire diversity and response magnitude. *Immunity* **27**, 203–213 (2007).
 26. Tan, T. C. J. *et al.* Suboptimal T-cell receptor signaling compromises protein translation, ribosome biogenesis, and proliferation of mouse CD8 T cells. *Proc. Natl. Acad. Sci. U. S. A.* **114**, E6117–E6126 (2017).
 27. Soerens, A. G. *et al.* Functional T cells are capable of supernumerary cell division and longevity. *Nature* **614**, 762–766 (2023).
 28. Bouso, P. *et al.* Diversity, functionality, and stability of the T cell repertoire derived in vivo from a single human T cell precursor. *Proc. Natl. Acad. Sci. U. S. A.* **97**,

- 274–278 (2000).
29. DuPage, M. & Bluestone, J. A. Harnessing the plasticity of CD4(+) T cells to treat immune-mediated disease. *Nat. Rev. Immunol.* **16**, 149–163 (2016).
 30. Akondy, R. S. *et al.* Origin and differentiation of human memory CD8 T cells after vaccination. *Nature* **552**, 362–367 (2017).
 31. Sarkar, S. *et al.* Strength of Stimulus and Clonal Competition Impact the Rate of Memory CD8 T Cell Differentiation¹². *J. Immunol.* **179**, 6704–6714 (2007).
 32. Joshi, N. S. & Kaech, S. M. Effector CD8 T Cell Development: A Balancing Act between Memory Cell Potential and Terminal Differentiation¹. *J. Immunol.* **180**, 1309–1315 (2008).
 33. Wei, S. C. *et al.* Distinct Cellular Mechanisms Underlie Anti-CTLA-4 and Anti-PD-1 Checkpoint Blockade. *Cell* **170**, 1120–1133.e17 (2017).
 34. Cha, E. *et al.* Improved survival with T cell clonotype stability after anti-CTLA-4 treatment in cancer patients. *Sci. Transl. Med.* **6**, 238ra70 (2014).
 35. Reuben, A. *et al.* Comprehensive T cell repertoire characterization of non-small cell lung cancer. *Nat. Commun.* **11**, 1–13 (2020).
 36. Anderton, S. M. & Wraith, D. C. Selection and fine-tuning of the autoimmune T-cell repertoire. *Nat. Rev. Immunol.* **2**, 487–498 (2002).
 37. Peri, A. *et al.* The landscape of T cell antigens for cancer immunotherapy. *Nature Cancer* 1–18 (2023).
 38. Salerno, F., Turner, M. & Wolkers, M. C. Dynamic Post-Transcriptional Events Governing CD8 T Cell Homeostasis and Effector Function. *Trends Immunol.* **41**, 240–254 (2020).

39. Anthony, D. D. & Lehmann, P. V. T-cell epitope mapping using the ELISPOT approach. *Methods* **29**, 260–269 (2003).
40. Spitzer, M. H. *et al.* IMMUNOLOGY. An interactive reference framework for modeling a dynamic immune system. *Science* **349**, 1259425 (2015).
41. Good, Z. *et al.* Proliferation tracing with single-cell mass cytometry optimizes generation of stem cell memory-like T cells. *Nat. Biotechnol.* **37**, 259–266 (2019).
42. Pilch, H. *et al.* Improved assessment of T-cell receptor (TCR) VB repertoire in clinical specimens: combination of TCR-CDR3 spectratyping with flow cytometry-based TCR VB frequency analysis. *Clin. Diagn. Lab. Immunol.* **9**, 257–266 (2002).
43. Cukalac, T. *et al.* Paired TCR $\alpha\beta$ analysis of virus-specific CD8(+) T cells exposes diversity in a previously defined ‘narrow’ repertoire. *Immunol. Cell Biol.* **93**, 804–814 (2015).
44. Yang, Y. *et al.* Focused specificity of intestinal TH17 cells towards commensal bacterial antigens. *Nature* **510**, 152–156 (2014).
45. Brockstedt, D. G. *et al.* Listeria-based cancer vaccines that segregate immunogenicity from toxicity. *Proc. Natl. Acad. Sci. U. S. A.* **101**, 13832–13837 (2004).
46. Qiu, Z., Khairallah, C. & Sheridan, B. S. Listeria Monocytogenes: A Model Pathogen Continues to Refine Our Knowledge of the CD8 T Cell Response. *Pathogens* **7**, 55 (2018).
47. Levine, L. S. *et al.* Single-cell analysis by mass cytometry reveals metabolic states of early-activated CD8+ T cells during the primary immune response. *Immunity* **54**, 829–844.e5 (2021).

48. Kelly, J. M. *et al.* Identification of conserved T cell receptor CDR3 residues contacting known exposed peptide side chains from a major histocompatibility complex class I-bound determinant. *Eur. J. Immunol.* **23**, 3318–3326 (1993).
49. T cell receptor antagonist peptides induce positive selection. *Cell* **76**, 17–27 (1994).
50. Safley, S. A., Cluff, C. W., Marshall, N. E. & Ziegler, H. K. Role of listeriolysin-O (LLO) in the T lymphocyte response to infection with *Listeria monocytogenes*. Identification of T cell epitopes of LLO. *J. Immunol.* **146**, 3604–3616 (1991).
51. Geginat, G., Schenk, S., Skoberne, M., Goebel, W. & Hof, H. A Novel Approach of Direct Ex Vivo Epitope Mapping Identifies Dominant and Subdominant CD4 and CD8 T Cell Epitopes from *Listeria monocytogenes*. *J. Immunol.* **166**, 1877–1884 (2001).
52. Straub, A. *et al.* Recruitment of epitope-specific T cell clones with a low-avidity threshold supports efficacy against mutational escape upon re-infection. *Immunity* **56**, 1269–1284.e6 (2023).
53. Sockolosky, J. T. *et al.* Selective targeting of engineered T cells using orthogonal IL-2 cytokine-receptor complexes. *Science* **359**, 1037–1042 (2018).
54. Hufford, M. M., Kim, T. S., Sun, J. & Braciale, T. J. The Effector T Cell Response to Influenza Infection. *Influenza Pathogenesis and Control - Volume II* 423–455 (2014).
55. Multiplex peptide-MHC tetramer staining using mass cytometry for deep analysis of the influenza-specific T-cell response in mice. *J. Immunol. Methods* **453**, 30–36 (2018).
56. Vitiello, A. *et al.* Immunodominance analysis of CTL responses to influenza PR8

- virus reveals two new dominant and subdominant Kb-restricted epitopes. *J. Immunol.* **157**, 5555–5562 (1996).
57. Belz, G. T., Xie, W., Altman, J. D. & Doherty, P. C. A Previously Unrecognized H-2Db-Restricted Peptide Prominent in the Primary Influenza A Virus-Specific CD8+T-Cell Response Is Much Less Apparent following Secondary Challenge. *J. Virol.* (2000) doi:10.1128/jvi.74.8.3486-3493.2000.
58. Nayak, J. L., Richards, K. A., Chaves, F. A. & Sant, A. J. Analyses of the specificity of CD4 T cells during the primary immune response to influenza virus reveals dramatic MHC-linked asymmetries in reactivity to individual viral proteins. *Viral Immunol.* **23**, 169–180 (2010).
59. Arpaia, N. *et al.* A Distinct Function of Regulatory T Cells in Tissue Protection. *Cell* **162**, 1078–1089 (2015).
60. Kok, L., Masopust, D. & Schumacher, T. N. The precursors of CD8+ tissue resident memory T cells: from lymphoid organs to infected tissues. *Nat. Rev. Immunol.* **22**, 283–293 (2021).
61. Montelongo-Jauregui, D., Vila, T., Sultan, A. S. & Jabra-Rizk, M. A. Convalescent serum therapy for COVID-19: A 19th century remedy for a 21st century disease. *PLoS Pathog.* **16**, e1008735 (2020).
62. Mercado, R. *et al.* Early Programming of T Cell Populations Responding to Bacterial Infection¹. *J. Immunol.* **165**, 6833–6839 (2000).
63. McGill, J. & Legge, K. L. Cutting Edge: Contribution of Lung-Resident T Cell Proliferation to the Overall Magnitude of the Antigen-Specific CD8 T Cell Response in the Lungs following Murine Influenza Virus Infection¹. *J. Immunol.* **183**, 4177–

- 4181 (2009).
64. Pai, J. A. & Satpathy, A. T. High-throughput and single-cell T cell receptor sequencing technologies. *Nat. Methods* **18**, 881–892 (2021).
 65. Rotrosen, E. & Kupper, T. S. Assessing the generation of tissue resident memory T cells by vaccines. *Nat. Rev. Immunol.* 1–11 (2023).
 66. Chang, J. T., Wherry, E. J. & Goldrath, A. W. Molecular regulation of effector and memory T cell differentiation. *Nat. Immunol.* **15**, 1104–1115 (2014).
 67. Roth, G. A. *et al.* Designing spatial and temporal control of vaccine responses. *Nature Reviews Materials* **7**, 174–195 (2021).
 68. COVID-19 convalescent plasma composition and immunological effects in severe patients. *J. Autoimmun.* **118**, 102598 (2021).
 69. Bloch, E. M. *et al.* Deployment of convalescent plasma for the prevention and treatment of COVID-19. *J. Clin. Invest.* **130**, 2757–2765 (2020).
 70. Cheng, Y. *et al.* Use of convalescent plasma therapy in SARS patients in Hong Kong. *Eur. J. Clin. Microbiol. Infect. Dis.* **24**, 44–46 (2005).
 71. Libster, R. *et al.* Early High-Titer Plasma Therapy to Prevent Severe Covid-19 in Older Adults. *N. Engl. J. Med.* **384**, 610–618 (2021).
 72. Gharbharan, A. *et al.* Effects of potent neutralizing antibodies from convalescent plasma in patients hospitalized for severe SARS-CoV-2 infection. *Nat. Commun.* **12**, 3189 (2021).
 73. Cross, R. W. *et al.* Use of convalescent serum reduces severity of COVID-19 in nonhuman primates. *Cell Rep.* **34**, (2021).
 74. Shao, S., Wang, Y., Kang, H. & Tong, Z. Effect of convalescent blood products for

- patients with severe acute respiratory infections of viral etiology: A systematic review and meta-analysis. *Int. J. Infect. Dis.* **102**, 397–411 (2021).
75. Nguyen, T.-Q., Rollon, R. & Choi, Y.-K. Animal Models for Influenza Research: Strengths and Weaknesses. *Viruses* **13**, (2021).
76. Thangavel, R. R. & Bouvier, N. M. Animal models for influenza virus pathogenesis, transmission, and immunology. *J. Immunol. Methods* **410**, 60–79 (2014).
77. Pantaleo, G. *et al.* Evidence for rapid disappearance of initially expanded HIV-specific CD8⁺ T cell clones during primary HIV infection. *Proc. Natl. Acad. Sci. U. S. A.* **94**, 9848–9853 (1997).
78. Okas, M. *et al.* Clinical expansion of cord blood-derived T cells for use as donor lymphocyte infusion after cord blood transplantation. *J. Immunother.* **33**, 96–105 (2010).
79. Lavoie, P. M., Dumont, A. R., McGrath, H., Kernaleguen, A.-E. & Sékaly, R.-P. Delayed expansion of a restricted T cell repertoire by low-density TCR ligands. *Int. Immunol.* **17**, 931–941 (2005).
80. Sakaguchi, S., Yamaguchi, T., Nomura, T. & Ono, M. Regulatory T Cells and Immune Tolerance. *Cell* **133**, 775–787 (2008).
81. Liu, B. *et al.* Temporal single-cell tracing reveals clonal revival and expansion of precursor exhausted T cells during anti-PD-1 therapy in lung cancer. *Nature Cancer* **3**, 108–121 (2021).
82. Recent progress in the analysis of $\alpha\beta$ T cell and B cell receptor repertoires. *Curr. Opin. Immunol.* **59**, 109–114 (2019).
83. Sinnathamby, G. *et al.* Priming and activation of human ovarian and breast cancer-

- specific CD8⁺ T cells by polyvalent *Listeria monocytogenes*-based vaccines. *J. Immunother.* **32**, 856–869 (2009).
84. Zunder, E. R. *et al.* Palladium-based mass tag cell barcoding with a doublet-filtering scheme and single-cell deconvolution algorithm. *Nat. Protoc.* **10**, 316–333 (2015).
85. Finck, R. *et al.* Normalization of mass cytometry data with bead standards. *Cytometry A* **83**, 483–494 (2013).
86. Allen, B. M. *et al.* Systemic dysfunction and plasticity of the immune macroenvironment in cancer models. *Nat. Med.* **26**, 1125–1134 (2020).
87. Roberts, E. W. *et al.* Critical Role for CD103(+)/CD141(+) Dendritic Cells Bearing CCR7 for Tumor Antigen Trafficking and Priming of T Cell Immunity in Melanoma. *Cancer Cell* **30**, 324–336 (2016).
88. Salmon, H. *et al.* Expansion and Activation of CD103(+) Dendritic Cell Progenitors at the Tumor Site Enhances Tumor Responses to Therapeutic PD-L1 and BRAF Inhibition. *Immunity* **44**, 924–938 (2016).
89. Edelson, B. T. *et al.* CD8 α (+) dendritic cells are an obligate cellular entry point for productive infection by *Listeria monocytogenes*. *Immunity* **35**, 236–248 (2011).
90. Liu, D. *et al.* IL-10-Dependent Crosstalk between Murine Marginal Zone B Cells, Macrophages, and CD8 α Dendritic Cells Promotes *Listeria monocytogenes* Infection. *Immunity* **51**, 64–76.e7 (2019).
91. Khan, S. H. & Badovinac, V. P. *Listeria monocytogenes*: a model pathogen to study antigen-specific memory CD8 T cell responses. *Semin. Immunopathol.* **37**, 301–310 (2015).
92. Eitel, J., Suttrop, N. & Opitz, B. Innate immune recognition and inflammasome

- activation in listeria monocytogenes infection. *Front. Microbiol.* **1**, 149 (2010).
93. Neuenhahn, M. *et al.* CD8alpha+ dendritic cells are required for efficient entry of *Listeria monocytogenes* into the spleen. *Immunity* **25**, 619–630 (2006).
94. Neuenhahn, M. & Busch, D. H. Unique functions of splenic CD8alpha+ dendritic cells during infection with intracellular pathogens. *Immunol. Lett.* **114**, 66–72 (2007).
95. Hiam-Galvez, K. J. *et al.* Transient dendritic cell activation diversifies the T cell response to acute infection. *bioRxiv* 2021.09.26.461821 (2021)
doi:10.1101/2021.09.26.461821.
96. Dinarello, C. A. Overview of the IL-1 family in innate inflammation and acquired immunity. *Immunol. Rev.* **281**, 8–27 (2018).
97. Apte, R. N. *et al.* Effects of micro-environment- and malignant cell-derived interleukin-1 in carcinogenesis, tumour invasiveness and tumour–host interactions. *Eur. J. Cancer* **42**, 751–759 (2006).
98. Singer, C. F. *et al.* Interleukin-1alpha protein secretion in breast cancer is associated with poor differentiation and estrogen receptor alpha negativity. *Int. J. Gynecol. Cancer* **16 Suppl 2**, 556–559 (2006).
99. Coussens, L. M. & Werb, Z. Inflammation and cancer. *Nature* **420**, 860–867 (2002).
100. Maurer, D. M. *et al.* Dysregulated NF-κB-Dependent ICOSL Expression in Human Dendritic Cell Vaccines Impairs T-cell Responses in Patients with Melanoma. *Cancer Immunol Res* **8**, 1554–1567 (2020).
101. McIntyre, K. W. *et al.* Inhibition of interleukin 1 (IL-1) binding and bioactivity in vitro and modulation of acute inflammation in vivo by IL-1 receptor antagonist and anti-

- IL-1 receptor monoclonal antibody. *J. Exp. Med.* **173**, 931–939 (1991).
102. Wu, T.-C. *et al.* IL1 Receptor Antagonist Controls Transcriptional Signature of Inflammation in Patients with Metastatic Breast Cancer. *Cancer Res.* **78**, 5243–5258 (2018).
103. Roederer, M. Interpretation of cellular proliferation data: Avoid the panglossian. *Cytometry A* **79A**, 95–101 (2011).
104. Kirkling, M. E. *et al.* Notch Signaling Facilitates In Vitro Generation of Cross-Presenting Classical Dendritic Cells. *Cell Rep.* **23**, 3658–3672.e6 (2018).
105. Dobin, A. *et al.* STAR: ultrafast universal RNA-seq aligner. *Bioinformatics* **29**, 15–21 (2013).
106. Liao, Y., Smyth, G. K. & Shi, W. featureCounts: an efficient general purpose program for assigning sequence reads to genomic features. *Bioinformatics* **30**, 923–930 (2014).
107. Love, M. I., Huber, W. & Anders, S. Moderated estimation of fold change and dispersion for RNA-seq data with DESeq2. *Genome Biol.* **15**, 550 (2014).
108. Zhou, Y. *et al.* Metascape provides a biologist-oriented resource for the analysis of systems-level datasets. *Nat. Commun.* **10**, 1523 (2019).
109. Castanza, A. S. *et al.* Extending support for mouse data in the Molecular Signatures Database (MSigDB). *Nat. Methods* **20**, 1619–1620 (2023).
110. Subramanian, A. *et al.* Gene set enrichment analysis: a knowledge-based approach for interpreting genome-wide expression profiles. *Proc. Natl. Acad. Sci. U. S. A.* **102**, 15545–15550 (2005).
111. Liberzon, A. *et al.* The Molecular Signatures Database (MSigDB) hallmark gene set

collection. *Cell Syst* **1**, 417–425 (2015).

Publishing Agreement

It is the policy of the University to encourage open access and broad distribution of all theses, dissertations, and manuscripts. The Graduate Division will facilitate the distribution of UCSF theses, dissertations, and manuscripts to the UCSF Library for open access and distribution. UCSF will make such theses, dissertations, and manuscripts accessible to the public and will take reasonable steps to preserve these works in perpetuity.

I hereby grant the non-exclusive, perpetual right to The Regents of the University of California to reproduce, publicly display, distribute, preserve, and publish copies of my thesis, dissertation, or manuscript in any form or media, now existing or later derived, including access online for teaching, research, and public service purposes.

DocuSigned by:

Rachel DeBarge

35D8356C9F6741D...

Author Signature

12/11/2023

Date